



MERCURY'S SODIUM EXOSPHERE

CARL A. SCHMIDT

Dissertation submitted in partial fulfillment
of the requirements for the degree of
Doctor of Philosophy

**BOSTON
UNIVERSITY**

BOSTON UNIVERSITY
GRADUATE SCHOOL OF ARTS AND SCIENCES

Dissertation

MERCURY'S SODIUM EXOSPHERE

by

CARL A. SCHMIDT

M.A., Boston University, 2008
B.A., University of Colorado, 2005

Submitted in partial fulfillment of the
requirements for the degree of
Doctor of Philosophy

2013

© Copyright by
CARL A. SCHMIDT
2013

Approved by

First Reader

Michael Mendillo, PhD
Professor of Astronomy
Boston University

Second Reader

John T. Clarke, PhD
Professor of Astronomy
Boston University

Acknowledgments

This work has been achieved with the help and guidance of many. Firstly, it has been an great honor and a pleasure to work with Professor Micheal Mendillo. I am deeply grateful for his persistent support, which, in hindsight, was a masterfully choreographed balance of pushing me in a fruitful research direction while making space for me to steer my own course. I am truly inspired by Prof. Mendillo's wisdom in a wide breath of topics, and his resourceful ability to synthesize that knowledge in applications spanning throughout our solar system.

My other committee members deserve recognition for their meticulous reading of this thesis, their insightful comments and questions, and for helping me to place the microcosm of my research in a broader context: Professors John Clarke, Nick Schneider, Paul Withers, and Andrew West. I am very much indebted to Jeffrey Baumgardner, whom I believe has the greatest passion for observational astronomy of anyone I know. Jeff was actively invested many aspects of my graduate education, and consistently greeted my questions with interest and enthusiasm, even when their resolve necessitated long and detailed discussions. Many thanks are also owed to Dr. Jody Wilson, who played a central role in early foundation of my graduate research in aspects of both observations and modeling. I also wish to thank Dr. Luke Moore for many friendly discussions regarding the early career of a planetary scientist.

I especially thank Annika Bentley for championing the patience and encouragement that marriage to a graduate student in the sciences involves. Finally, I would like to thank my family for their continuous support of my education in science, regardless if it may have seemed a long or esoteric pursuit in the graduate years.

atoms s^{-1} , nearly twice the highest rate previously reported. By forward modeling Mercury's atmospheric escape, I place new constraints on the source properties and eliminate the prevailing theory that the escaping tail is sputtered from the surface by solar wind ions. The MESSENGER spacecraft has recently discovered that sodium is distributed unevenly over the planet's surface and that the magnetosphere is offset from the planet's center. Using the first model to include these effects, I demonstrate the magnetosphere's influence upon exospheric sources by simulating asymmetries observed in the escaping atmosphere. I conclude that the exosphere is sustained by a combination of micro-meteorite impact vaporization and photo-desorption that is locally enhanced by precipitating ions.

Contents

1	Introduction	1
1.1	Motivation and Overview of this Dissertation	2
1.2	Previous Work	3
1.2.1	The Sodium Exosphere: Observations	3
1.2.2	The Sodium Exosphere: Sources and Surface Interactions	5
1.2.3	The Sodium Exosphere: Modeling	10
2	Sodium Tail Observations	14
2.1	Introduction	14
2.2	Observational Methods for Ground-Based Measurements	14
2.3	Instrumentation	15
2.3.1	Wide-field Coronagraph	15
2.3.2	Image Slicing Spectrograph	16
2.4	Data Reduction	23
2.4.1	Instrumental Corrections	23
2.4.2	Filter Characterizations	27
2.4.3	Standard Star Calibrations and Atmospheric Extinction	31
2.4.4	Calibration and Reduction Procedures	33
2.5	Data Acquired	38
2.5.1	Wide-field Coronagraph: Distant Tail	40
2.5.2	Variation in escape rates	45
2.5.3	Image Slicing Spectrograph: Near Planet Tail	49

3	The Interpretation of the Data and Simulating Na Exospheres	52
3.1	Introduction	52
3.2	Sodium Spectroscopy	52
3.3	Radiative Transfer: Resonant Scattering	55
3.4	Radiative Transfer: Radiation Pressure	62
3.5	1-Dimensional Approximations in Wide Field Data Analysis	66
3.5.1	Down-tail Velocity Estimation	66
3.5.2	Transverse velocity	68
3.5.3	Down-tail Transit in a Steady Escape	70
3.5.4	1D Estimation of escape rates	71
4	Modeling The Sodium Tail	76
4.1	Introduction	76
4.2	Numerical Monte Carlo Model	76
4.2.1	Original Lunar Code	77
4.2.2	Adaptation for Mercury	78
4.3	Source Processes and Their Intrinsic and Potential Time Variabilities	88
4.3.1	Thermal Evaporation	89
4.3.2	Photon Stimulated Desorption	89
4.3.3	Ion Sputtering	94
4.3.4	Impact Vaporization	99
4.3.5	Conclusion	101
5	Model-Data Comparisons	102
5.1	Introduction	102
5.2	Modeling the Wide-field Coronagraph Data: New Constraints on Exospheric Processes	102
5.2.1	Constraints on Source Mechanisms	102

5.2.2	Constraints on Energetic Processes	107
5.2.3	Seasonal Effects	109
5.2.4	Constraints on Potential Short-Term Source Variability	114
5.3	Modeling of Simultaneous Ground-Based Data	120
5.3.1	Constraints on North-South Asymmetries	122
6	Summary	134
6.1	Conclusions	134
6.1.1	Summary of Observational Results: Schmidt et al. (2010)	135
6.1.2	Model Results based on the Wide-Field Data: Schmidt et al. (2012)	136
6.1.3	Summary of North-South Asymmetry Study: Schmidt (2013)	140
6.2	Discussion	141
6.3	Future Work	145
	References	151
	Curriculum Vitae	158

List of Tables

2.1	Sodium D Line Observations of Mercury at McDonald Observatory 2007-2012	39
3.1	FWHM of Gaussian fits to the tail width and transverse velocity com- ponents for each observation of the sodium tail.	69
5.1	Global Source Rates of Sodium Required to Simulate Observed Escape	107
5.2	Percentage of Na Ejected into the Atmosphere that Escaped by Source ¹ and Date ²	113

List of Figures

1.1	Diagram of Exospheric Processes	6
2.1	Coronagraph Diagram	15
2.2	Coronagraph Raw Data	17
2.3	Fiber Allocation	18
2.4	Spectrograph Diagram	19
2.5	Data Example: Image Slicing Spectrograph	21
2.6	Aperture Tracing	22
2.7	Row Stacked Spectra	25
2.8	Filter 1 Characteristics	28
2.9	Filter 2 Characteristics	29
2.10	Filter 3 Characteristics	30
2.11	Terrestrial Na Sampling	36
2.12	Initial Measurements - Day to Day Variability	40
2.13	Initial Measurements - Month to Month Variability	42
2.14	Initial Measurements - Non-Detections	43
2.15	Initial Measurements - Down-tail Profiles	44
2.16	Radiation Pressure vs. Orbital Phase	45
2.17	Daily Variability April 2009	47
2.18	Daily Variability June 2012	48
2.19	ISS: 21 December 2011	49
2.20	ISS: 4 July 2011	50

2.21	ISS: 26 December 2011	51
3.1	Grotrian Diagram	53
3.2	Zeeman Splitting: Allowed Transitions	55
3.3	Ratio of Excitation States	57
3.4	Absorption Line Broadening	59
3.5	Equivalent Width Curve of Growth	61
3.6	Fraunhofer Spectrum	63
3.7	Tail Velocity Profile - 1D Approximation	67
3.8	Transverse Velocity Profile	69
3.9	Acceleration vs. Orbital Phase	71
3.10	Initial estimation of escape rates	73
4.1	Validation	79
4.2	Surface Temperature Model	85
4.3	Diurnal Surface Temperature	86
4.4	Maximum Surface Temperature	87
4.5	Source Energy Distributions	90
4.6	PSD Energy Fitting	95
5.1	Model-Coronagraph Comparisons	104
5.2	Cross-Tail Profiles	108
5.3	Model-Coronagraph Comparisons: Non-Detection	110
5.4	Extreme Sputtering Event	116
5.5	Extreme Meteor Impact	118
5.6	Simulated Asymmetries in the Cross-tail Profile	124
5.7	Disk Resolved Imaging	126
5.8	Simulated Asymmetries and Their Sources	129

5.9 Diagram of Asymmetric Processes 131

List of Abbreviations

AEOS	Advanced Electro Optical System
FWHM	Full Width at Half Maximum
GRS	Gamma-Ray Spectrometer
IDL	Interactive Data Language
IS	Ion Sputtering
LCROSS	Lunar Crater Observation and Sensing Satellite
MASCS	Mercury Atmospheric and Surface Composition Spectrometer
MESSENGER	MERcury Surface, Space ENVironment, GEochemistry, and Ranging
MIV	Meteorite Impact Vaporization
NASA	National Aeronautics and Space Administration
PSD	Photon-Stimulated Desorption
PSF	Point Spread Function
RSS	Row Stacked Spectra
SORCE	Solar Radiation and Climate Experiment
SPICE	Spacecraft Planet Instrument C-matrix Events
TD	Thermal Desorption

Chapter 1

Introduction

This work addresses the escape of sodium from Mercury's atmosphere. The atmosphere consists of atoms liberated from the surface by various processes, following ballistic trajectories guided by gravity and solar radiation pressure, i.e., an exosphere with a surface boundary. The highest energy component of sodium in Mercury's exosphere forms a comet-like tail escaping the planet due to acceleration by radiation pressure (Potter et al., 2002). Sodium D-line measurements of Mercury's atmospheric escape provide constraints that aid in characterizing the sources and physical processes sustaining the exosphere.

Data from a series of observing campaigns using the wide-field coronagraphic technique described in Baumgardner & Mendillo (2009) and the image-slicing spectrograph approach described in Baumgardner et al. (2000) are presented here. The wide field of view of both instruments can image sodium emission at great distances from the planet's surface, making them ideally suited for studying atmospheric escape. This new set of remote sodium observations builds upon the latest domain for exospheric science at Mercury, as recently described in Baumgardner et al. (2008) and Potter & Killen (2008). Using these instruments, I will demonstrate that the $\sim 1000 R_M$ tail can be a persistent feature, that the escape of Mercury's Na exosphere is heavily modulated by radiation pressure, and that it can exceed previously published estimates. My goal is to document the orbital phase dependence of escape due to radiation pressure, as well as possible changes in source rates over time periods ranging

from a few hours to several years. Over the length of the tail, the coronagraph images can record a ~ 10 hour time history of Mercury’s escaping Na atmosphere in which the signal is bright enough to distinguish possible changes in escape rates. This dataset thus enables the first study of short time-scale variations in the loss of Mercury’s atmosphere.

To interpret the data physically, I simulate the escape of Mercury’s sodium exosphere with a numerical model using Monte Carlo techniques. I have developed this model to constrain, and in some cases eliminate, the many uncertainties regarding the nature of the sources of Mercury’s atmosphere. In my Schmidt et al. (2012) study, the escape rates of several sources are calculated at different orbital phases for direct comparison to the wide-field measurements in the studies of Baumgardner et al. (2008) and my Schmidt et al. (2010) work. Source fluxes required to generate the observed brightness are derived from the model and compared with other published estimates, forming constraints on the variability of the high-energy sources that supply the tail. I also simulate short-term variations in high-energy sources with the goal of determining the variability in ejection rates at the surface capable of detection in wide-field images. Finally, this model is further used to investigate anisotropies and asymmetries that have been observed in the escaping atmosphere, and their potential relation to localized physical processes on the surface.

1.1 Motivation and Overview of this Dissertation

The research in this dissertation was carried out with the purpose of investigating and answering the following important questions about the Mercury system: “What is/are the source/sources of Mercury’s atmosphere? How much of Mercury’s atmosphere is escaping? How does this escape vary with time? Do sources keep up with losses? Is the exosphere coupled to the magnetosphere?” The process of answering

these questions is involved and will be described in Chapters 2 - 5. The answers themselves, however, are succinct and conclusive, with each resolved specifically in Section 6.1.

1.2 Previous Work

1.2.1 The Sodium Exosphere: Observations

Observations of Mercury's exosphere are complicated by the planet's proximity to the Sun. To date, the bulk of ground-based data were taken using solar telescopes during Earth's daylight. Summaries of several extensive data sets for sodium D-line emission at Mercury can be found in Sprague et al. (1997), Potter et al. (2007) and Leblanc & Johnson (2010). These reports reveal a high degree of temporal variability in emission seasonally, diurnally, and regionally.

Several comets (Combi et al., 1997; Cremonese et al., 1997; Wilson et al., 1998), the Moon (Mendillo et al., 1991; Smith et al., 1999; Wilson et al., 1999; Mierkiewicz et al., 2006) and the planet Mercury (Potter et al., 2002; Potter & Killen, 2008; Kameda et al., 2008) have all been shown to have tails of neutral sodium atoms escaping their surfaces. Mercury's neutral Na tail was observed at a distance of ~ 16 Mercury radii (R_M) by Potter et al. (2002) and subsequently imaged at distances greater than 1000 planetary radii (Baumgardner et al., 2008). It is well known that sodium tails can extend for millions of kilometers from comets and the Moon (Cremonese et al., 1997; Smith et al., 1999), yet this is a recent discovery for Mercury (Baumgardner et al., 2008).

Observational estimates of the Na gas temperatures at Mercury span a wide range. High resolution spectrograph measurements at the McDonald Observatory have shown the Na emission lines to be well approximated by thermal distributions. However, using the same instrumentation, temperatures of 500K (Potter & Morgan,

1987) and 1500K (Killen et al., 1999) were independently reported. Killen et al. (1999) estimated gas temperatures by fitting the D2 line profile; temperatures were found to vary spatially and were everywhere 600-700 K hotter than the surface. More recently, the polar scans within 1500 km of Mercury's limb by MESSENGER are well fit by a Chamberlain exosphere at hotter temperatures of $\sim 1340\text{K}-1600\text{K}$ (Cassidy, personal communication 2013). These high temperatures characterize the energies that may originate from a combination of various source mechanisms, each of which do not intrinsically have a Maxwellian velocity distribution. Some observational evidence suggests multiple energy components with a very hot ($\sim 6500\text{ K}$) suprathermal population, which is attributed to ion sputtering (Potter & Morgan, 1997; Wurz & Lammer, 2003; Mura et al., 2009).

Initial observations found escape rates into the tail to be 1-10% of the estimated ejection rate at the surface (Potter et al., 2002). Recent ultrawide 7° field images of the planet contain a snapshot of sodium escape over as much as 15 hours (Baumgardner et al., 2008), roughly two e-folding photo-ionization lifetimes (Huebner et al., 1992). Naturally, such data suggest an investigation of potential short-term variability of high-energy sources at the surface. Sputtering of high-energy atoms by impacting solar wind and precipitating magnetospheric ions are expected to vary on timescales of hours. Several ground-based data sets have shown significant short-term variations in the exospheric sodium distribution, both spatially and temporally (e.g., Potter et al., 1999; Leblanc et al., 2009; Mouawad et al., 2011).

In the absence of a collisional atmosphere or ionosphere, plasma in Mercury's magnetic field has direct access to the planet's surface. Precipitating ions and electrons help to liberate gases from the regolith and sustain a thin exosphere. In this way, the exosphere is directly coupled to the magnetosphere. The extent of the magnetosphere's influence over the exosphere remains poorly constrained, however, as does the nature

of the surface interactions releasing both volatile and refractory species from Mercury’s regolith.

Observations of neutral sodium gas concentrated mid and high-latitude regions of the dayside showered by plasma suggest magnetosphere-exosphere coupling (e.g., Potter & Morgan, 1990; Baumgardner et al., 2008). Such features are frequently brighter in the south (e.g., Potter et al., 2006; Mangano et al., 2009). North-south asymmetries in the exosphere were initially attributed to the radial component of the interplanetary magnetic field (Sarantos et al., 2001). MESSENGER reveals, however, that precipitation in the southern cusp may be on average four times higher than in the north as a consequence of the planet’s offset magnetosphere (Winslow et al., 2012).

Sodium tail measurements by Baumgardner et al. (2008), Potter & Killen (2008) and during the MESSENGER flybys (Vervack et al., 2010; McClintock et al., 2008) show both localized density structures and seasonal variations associated with changing radiation pressure during Mercury’s orbit. With the exception of Vervack et al. (2010), brightest emission in the northern lobe is consistent throughout these observations, rather than in the south, where sources enhanced by greater plasma precipitation are expected. Such north-south asymmetries in the tail must arise from exospheric sources distributed unevenly between these hemispheres. When investigating asymmetric sources, variations in the Na surface concentration must also be included in addition to plasma precipitation and space weather drivers (Evans et al., 2013).

1.2.2 The Sodium Exosphere: Sources and Surface Interactions

With the exception of neutralized solar wind particles, Mercury’s exosphere is generated by processes that liberate atoms from the surface mineralogy. Sources of sodium are considered to include photon-stimulated desorption (PSD), sputtering by ions (IS), meteor impact vaporization (MIV), and thermal desorption (TD) (Killen et al., 2007). The relative contributions of these mechanisms to the exosphere have

been actively disputed for many years, and recent modeling suggests that no single source mechanism dominates during the entire Mercury year (Leblanc & Johnson, 2010). Much of the Na exosphere bound by gravity can be efficiently generated by desorption (Yakshinskiy & Madey, 2000; Yoshioka et al., 2008). However, the brightness of the recently observed escaping component suggests the contribution from higher energy sources, such as ion sputtering and impact vaporization, is much more substantial than previously thought (Baumgardner et al., 2008). Fig. 1.1 gives an overview of the relevant processes at Mercury.

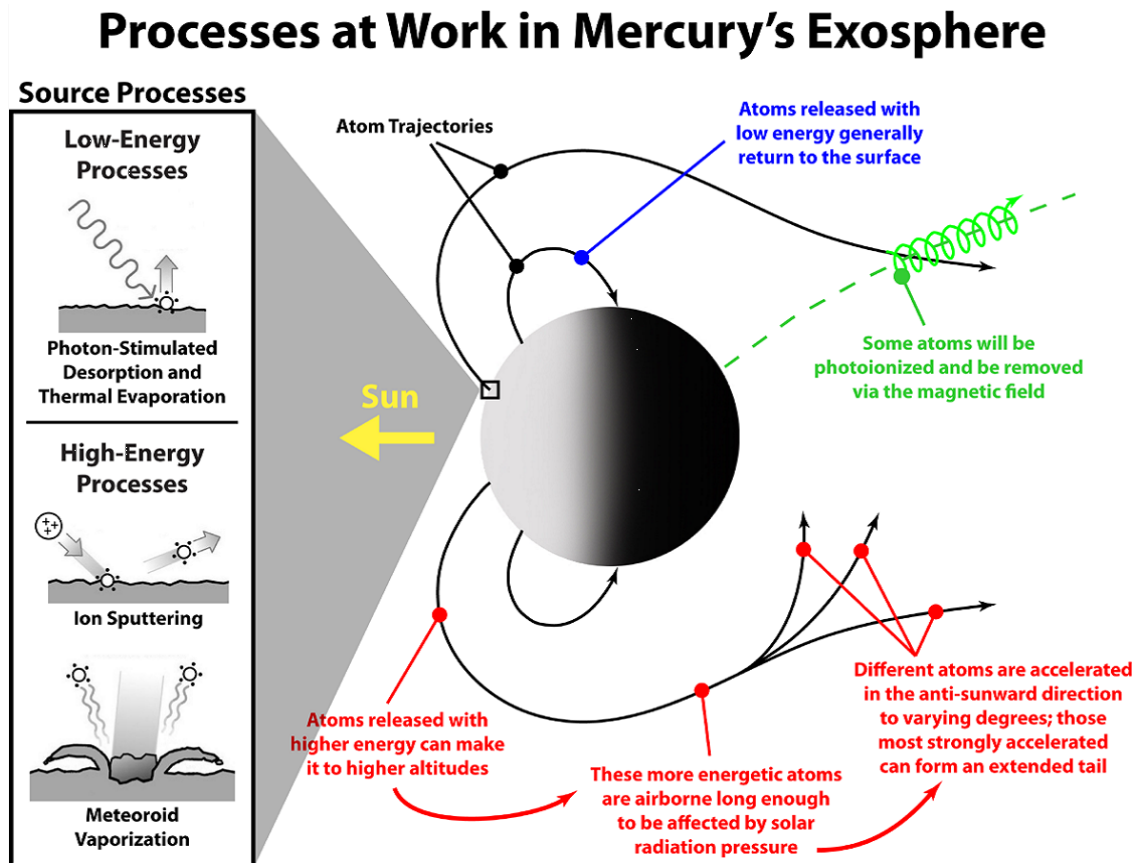
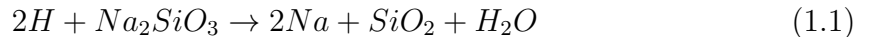


Figure 1.1 Diagram of the major source and loss processes that generate and sustain Mercury's exosphere. At left, panels depict the three primary sources of exospheric gas. Source: NASA

Observations have demonstrated that multiple source mechanisms exist in the lunar Na exosphere. On average the distribution of emission as a function of solar zenith angle is indicative of thermal desorption of photon-stimulated desorption as the predominate source (Mendillo & Baumgardner, 1995). Yet, observations in passing through the plasmashet of Earth’s magnetotail (Wilson et al., 2006), and during the intense 1998 Leonid meteor showers (Smith et al., 1999), show measurable deviations in column density, confirming the influence of IS and MIV drivers. Earth’s Moon is the best known analog to Mercury, and, while nature does not permit these experiments, there is expectation that several sources may shape Mercury’s exosphere as well.

Two additional sources of exospheric Na have been put forward. Sodium hydroxide may be produced in meteoroid collisions with the surface and has a photolysis lifetime shorter than the ballistic flight time (Self & Plane, 2002; Berezhnoy & Klumov, 2008). The Na produced has energies of the order of the 1-2 eV bond strength and will predominantly escape. Since this source would be distributed isotropically, it remains difficult to explain asymmetries in the escaping tail (Potter & Killen, 2008). Potter (1995) proposed a chemical reaction with hydrogen atoms derived from protons implanted into Na compounds in silicate rock, a mechanism termed chemical sputtering. An example reaction proceeds as:



Products on the right may desorb into the exosphere thermally. Although reaction 1.1 proceeds spontaneously, the activation energy and hence the reaction rate is unknown. As with Na, photo-destruction lifetimes for water are long compared with the ballistic flight times (Huebner et al., 1992). Much of the exospheric water molecules produced would therefore be returned to the surface, and some may collect in permanently shadowed regions. However, experiments onboard the MErcury Surface, Space EN-

vironment, GGeochemistry, and Ranging (MESSENGER) spacecraft have determined that water ice in polar craters is likely to be of cometary origin (Neumann et al., 2013), and the abundance of oxygen group ions is typically at least a factor of five less than Na^+ (Raines et al., 2013, *in press*).

In this work I will therefore limit consideration to four processes that liberate sodium atoms from the surface: meteoroid impacts (e.g., Cremonese et al., 2005), thermal desorption (McGrath et al., 1986; Hunten & Sprague, 2002; Leblanc & Johnson, 2003), photon-stimulated desorption (e.g., Potter & Morgan, 1985) and solar wind or exospheric pick-up ions channeled by magnetic field lines to the surface (e.g., Potter & Morgan, 1990; Ip, 1986; Delcourt et al., 2002; Lammer et al., 2003). Each of these four mechanisms has a relatively large uncertainty in its source rate. Yields of both desorption types vary with temperature, although in different ways (Yakshinskiy & Madey, 2004). Additionally, if the surfaces of grains become depleted of Na, the rates of desorption into the exosphere will be limited by diffusion (Killen et al., 2004). The diffusion rates vary exponentially with temperature according to the Arrhenius equation, $k = Ae^{-E_a/(k_B T)}$, where k_B is the Boltzmann constant and T is temperature. However, Arrhenius coefficients A and E_a heavily depend on how vitrified the surface is, and the corresponding diffusion rates (k) remain uncertain within a few orders of magnitude. Additionally, ions impacting the surface can break the lattice structure of the grain and enhance diffusion, thereby influencing other sources like desorption. Furthermore, the conductivity of the regolith is still not well constrained. Surface charging is hence poorly understood, but may have a large influence over surface interactions. Thus, many ambiguities perpetuate a lack of understanding of the surface physics governing the sources of the exosphere.

Sources of exospheric Na resulting from plasma precipitation differ in both their energies and the spatial distributions across the surface. In addition to cusp ion

impacts, precipitation to Mercury's nightside during the long night (88 Earth days) may chemically alter the surface, allowing subsequent desorption upon heating and exposure to sunlight (e.g., Sprague, 1992). Physical sputtering of Na atoms occurs predominantly by cusp ions, and generally results in gravitational escape. In contrast, secondary processes induced by ion impacts can release atoms into the exosphere at much lower energies. For instance, diffusion of Na to the topmost surface may be increased in regions of ion bombardment, thereby enhancing desorption (McGrath et al., 1986). Burger et al. (2010) required that diffusion enhancements increase photon stimulated desorption (PSD) by a factor of >5 in order to fit the MESSENGER flyby data. The effect of ion precipitation on PSD yields inferred from modeling of lunar sodium is smaller (x2) and energy-dependent (Sarantos et al., 2010). Wilson et al. (2006) observed that enhancements in the lunar Na exosphere were sustained for at least 15 hours after the Moon's passage through Earth's plasma sheet. The time lag in their measurements suggests that plasma interactions with the surface affect sources of exospheric Na indirectly, as the exosphere's response to the increased ion sputtering should fade on much shorter timescales.

While it is clear that the bulk of the exospheric sodium returns to the surface, the interactions between atoms and the surface also remains a subject of active research. Hunten et al. (1988) emphasized two distinct populations: those chemically bound to the regolith and those adsorbed from the exosphere. Madey et al. (1998) argued that re-impacting sodium will bond ionically to surface oxygen, and thus take on characteristics indistinguishable from sodium native to the regolith. Exospheric Na may also bounce off Mercury's surface. Laboratory measurements of Na interactions with lunar samples have shown that the probability that an atom will stick or bounce depends on the surface temperature (Yakshinskiy & Madey, 2005). Atoms that bounce may experience some level of accommodation with the local surface temperature and

the collision is probably not elastic (Hunten et al., 1988). Both the exit direction and energy relative to the incidence angle are changed in a surface bounce. Sticking and thermal accommodation are often parameterized as first order coefficients in models of surface bound exospheres (e.g., Smyth & Marconi, 1995; Burger et al., 2010; Mouawad et al., 2011; Killen et al., 2012).

Since collisions between exospheric atoms are rare, an atom’s velocity retains the characteristics of the associated source mechanism, unless modified by surface interactions. Although explanations of the observed spatial and temporal variations generally rely on other source mechanisms (e.g., Leblanc et al., 2007; Mura et al., 2009), photon-stimulated desorption is often hypothesized to be the dominant source of Mercury’s Na and K exosphere (Killen et al., 2001, 2004). Even if PSD is the true source for the bulk of the exosphere, very few desorbed atoms have energy sufficient to overcome gravity, and ion sputtered or micro-meteorite vaporized Na may still dominate escape. Determinations of the relative importance of these sources of energetic sodium are now possible by observations of tail behavior with orbital phase, such as those presented here, and observations during times of increased ion precipitation.

1.2.3 The Sodium Exosphere: Modeling

Estimates of Mercury’s total sodium production rate range from 1.35 to 10×10^{24} atoms/s (see Potter et al., 2002, for a review). Mura et al. (2009) suggest that (1-10%) of the atoms ejected by photon-stimulated desorption and 50% of ion sputtered atoms have enough energy to escape. The Na escape rate at Mercury is more than an order of magnitude larger than estimates of sodium loss at the Earth’s Moon (Wilson et al., 2003). Even larger sodium escape rates are not uncommon in our solar system. For comets, $\sim 10^{25}$ Na atoms/s were estimated to escape from comets Hale-Bopp (Cremonese et al., 1997), Halley and Kohoutek (Combi et al., 1997). Production at

Io varies substantially with volcanic activity, and at times may exceed the production rate at Mercury by more than two orders of magnitude (Wilson et al., 2002).

Soon after the discovery of atomic sodium in Mercury's exosphere by Potter & Morgan (1985), numerical models predicted that radiation pressure could force this gas into an anti-sunward tail (Ip, 1986; Smyth, 1986). A more in-depth analysis by Smyth & Marconi (1995) demonstrated dramatic changes in radiation pressure, and hence escape as a function of orbital longitude. These authors showed that atoms with a surface ejection velocity of at least 2 km s^{-1} can acquire the additional velocity needed to reach the 4.25 km/s escape speed. Additionally, modeled trajectories of escaping atoms were calculated to transit to the opposite hemisphere before traveling down-tail, an effect which has only recently become relevant, as I will discuss in detail in Section 5.3.1

More recent Monte Carlo models have focused on the relative contribution of the different source types in sustaining the Na exosphere. Yet, consensus between these studies remains elusive. Leblanc & Johnson (2003) modeled the Na surface density as having large differences on the day and night sides, at low and high latitudes, and in morning and afternoon regions due to the rapid depletion of sodium in the grain surfaces by thermal desorption. This work also determined that the rates of influx of meteoritic Na and of Na lost via photo-ionization are in equilibrium. An updated version of this model reported that the dominant source of the exosphere can shift between thermal desorption, photon stimulated desorption, and solar wind ion sputtering over one Hermean year (Leblanc & Johnson, 2010). Wurz et al. (2010) reported that meteor impact vaporization and sputtering were two orders of magnitude lower than the primary source, photon stimulated desorption. However, calculations by Borin et al. (2010) indicate the impact vaporization source is probably substantially

larger, and that the incident flux of micro-meteors is very much model dependent, spanning a few orders of magnitude depending on the assumed parameters.

Given the potential for coupling between the magnetosphere and the exosphere, some models have coupled exosphere simulations to codes that describe the precipitation of ions to the surface. Mura et al. (2009) synthesized the proton precipitation model of Delcourt et al. (2003) and attributed local enhancements in the cusp region to chemical sputtering rather than physical sputtering. Like Leblanc & Johnson (2003), this model also suggested strong heterogeneity in the Na surface distribution, particularly an enhancement of several orders of magnitude at dawn due to nighttime accumulation and in cusp regions due to chemical sputtering. Burger et al. (2010) built a model for the MESSENGER fly-by data which is qualitatively similar to the one which I will describe in Chapter 4, as both owe their heritage to codes first developed by Wilson & Schneider (1994). A separate model of proton precipitation during the flybys was generated by (Benna et al., 2010) and synthesis of the two demonstrated that models with PSD enhanced by factors of 4-9 in regions of ion bombardment best match the flyby data. In contrast to chemical sputtering posed by Mura et al. (2009), Burger et al. (2010) attributed local enhancements at the cusps to an increase in diffusion in regions of ion implantation.

The MESSENGER magnetometer has shown the magnetic dipole moment is offset from the planet's center by $.2 R_M$ to the north while approximately aligned with the spin axis (Anderson et al., 2011). Such a configuration produces an asymmetry in the magnetosphere cusp whereby more plasma has direct access to the planet's southern hemisphere than the northern one (Winslow et al., 2012). At the time of writing, no exosphere or magnetosphere models for ion precipitation use a magnetosphere with an offset center, though several are in development.

In summary, many questions survive concerning sodium in Mercury's atmosphere, even after nearly 25 years of research. In particular, the relative contributions of different source mechanisms, the nature of spatial and temporal variabilities, and the atmospheric loss rates all remain unknown. My contributions stem from new measurements of the escaping component, which I discuss in Chapter 2. Repeated observations at the same orbital phase signify an atmosphere that is predominantly seasonal. In Chapter 3, I use a simple 1-dimensional model to demonstrate that the overall atmospheric loss is greater than previously published estimates. Chapter 4 describes a more detailed 3-dimensional model, which is invoked in the following chapter to eliminate several proposed exospheric processes and find evidence for coupling between the exosphere and magnetosphere.

Chapter 2

Sodium Tail Observations

2.1 Introduction

This section describes two instruments that I have utilized to study sodium in Mercury's exosphere: a wide-field coronagraph and an image-slicing spectrograph, both located at the McDonald Observatory in Fort Davis, Texas. The calibration routine for each instrument is described, and calibrated images are given in units of Rayleighs. Data from each instrument represents a new achievement in ground-based imaging of the planet's escaping sodium atmosphere. The wide-field coronagraph data displays a sodium tail at distances of ~ 1500 planetary radii, the farthest reported measurement of the planet's exosphere. The image-slicing spectrograph data comprises the highest resolution images of Mercury's sodium tail taken from Earth.

2.2 Observational Methods for Ground-Based Measurements

Ground-based observations of Mercury are inherently difficult due to the planet's proximity to the Sun. The Mercury-Sun angle as seen from Earth never exceeds 28° , with elongations allowing imaging at twilight every few months. The Earth's atmosphere also emits strongly at the sodium D1 and D2 wavelengths, as micro-meteors deposit metals in the mesosphere. In spectroscopic observations, these terrestrial emissions conveniently provide a rest frame of reference from which Doppler shifted Na on Mercury can be easily distinguished. Conversely, narrow-band imaging of sodium

requires minimizing these terrestrial emissions, which can exceed Hermean signals in the tail by orders of magnitude. Such observations are possible only during short windows (<1 hour) occurring nightly over the several days surrounding maximum elongation. Even the most favorable conditions require observation at low elevation angles, through high air-mass, against a non-dark sky. Astronomers generally avoid these domains with good reason!

2.3 Instrumentation

2.3.1 Wide-field Coronagraph

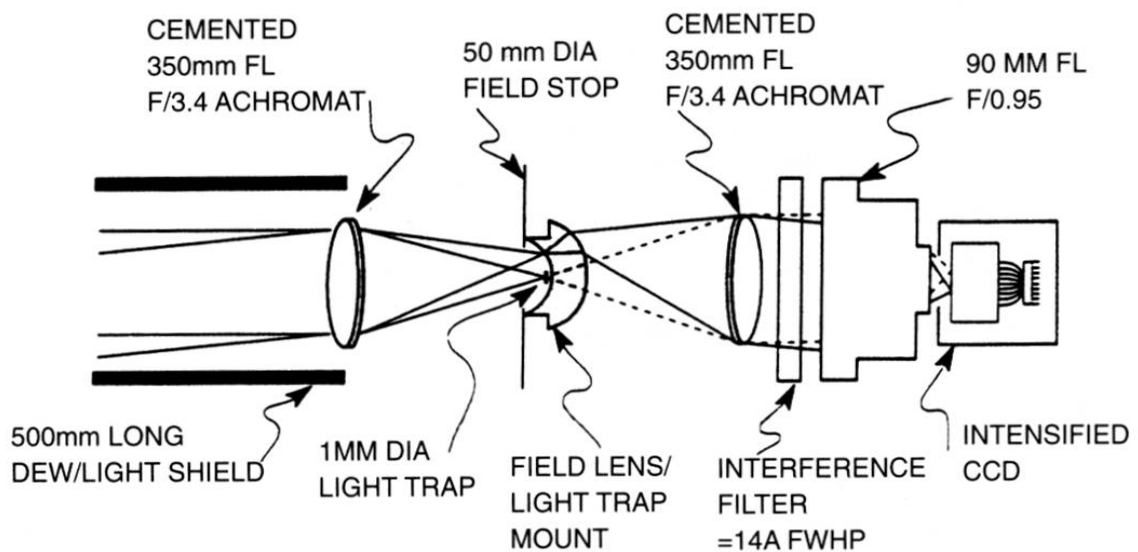


Figure 2.1 The optical layout of the coronagraph instrument used in wide-field direct imaging of Mercury's atmosphere.

The design of the coronagraph is elegantly simple, and it is certainly one of few telescopes capable of advancing a modern scientific field with a modest four inch aperture. The optics are refracting throughout and no mirrors are used. It consists of a unity power section (1x magnification) with an occulting mask attached to a

field lens at the focus of an f/3.4 objective. Placing the occulting mask early in the path minimizes scattered light that can reach the detector. The collimated beam then passes through a narrow-band interference filter and into a commercial camera lens with a fast beam of f/0.95 that images the sky onto a CCD detector. Fig. 2.1 shows the optical design of the instrument as recently described by Baumgardner & Mendillo (2009).

The short focal length (90 mm) commercial camera lens performs all magnification and images the beam onto a 1024×1024 CCD with $13 \mu\text{m}$ pixels allowing for a wide field of view, nearly 7° in diameter. The detector has a Peltier cooled housing, permitting dark currents of ~ 0.05 electrons/s at -25°C , and a read noise of ~ 9 electrons (RMS). With Mercury centered behind an occulting mask, exposures up to 5 min can be taken without saturating the CCD using a narrow-band ($\sim 14 \text{ \AA}$ FWHM) filter that passes sodium D1 and D2 emission lines. Observations in 2007 and 2008 utilized a 6 arcmin wide occulting mask with 2×2 pixel binning to increase sensitivity. Observations after May 2008 used 1×1 binning, trading sensitivity for resolution, and all observations 2009 onward use a 10^{-4} neutral density filter as an occulting mask. This neutral density filter passes a small amount of the solar continuum reflected from Mercury's surface, enabling Mercury's position to be determined directly in the image. Prior observations in 2007 and 2008 required triangulation from in-field stars to pinpoint the planet's location beneath the occulting mask. Figure 2.2 shows an example of a raw image from the coronagraph taken on UT 30 April 2009.

2.3.2 Image Slicing Spectrograph

In contrast to the coronagraph, the image slicing spectrograph is a relatively complex design. Although integral field spectrographs are becoming common in astrophysics, the Boston University image-slicing spectrograph at McDonald Observatory is currently the highest density fiber-fed spectrograph used in planetary science.

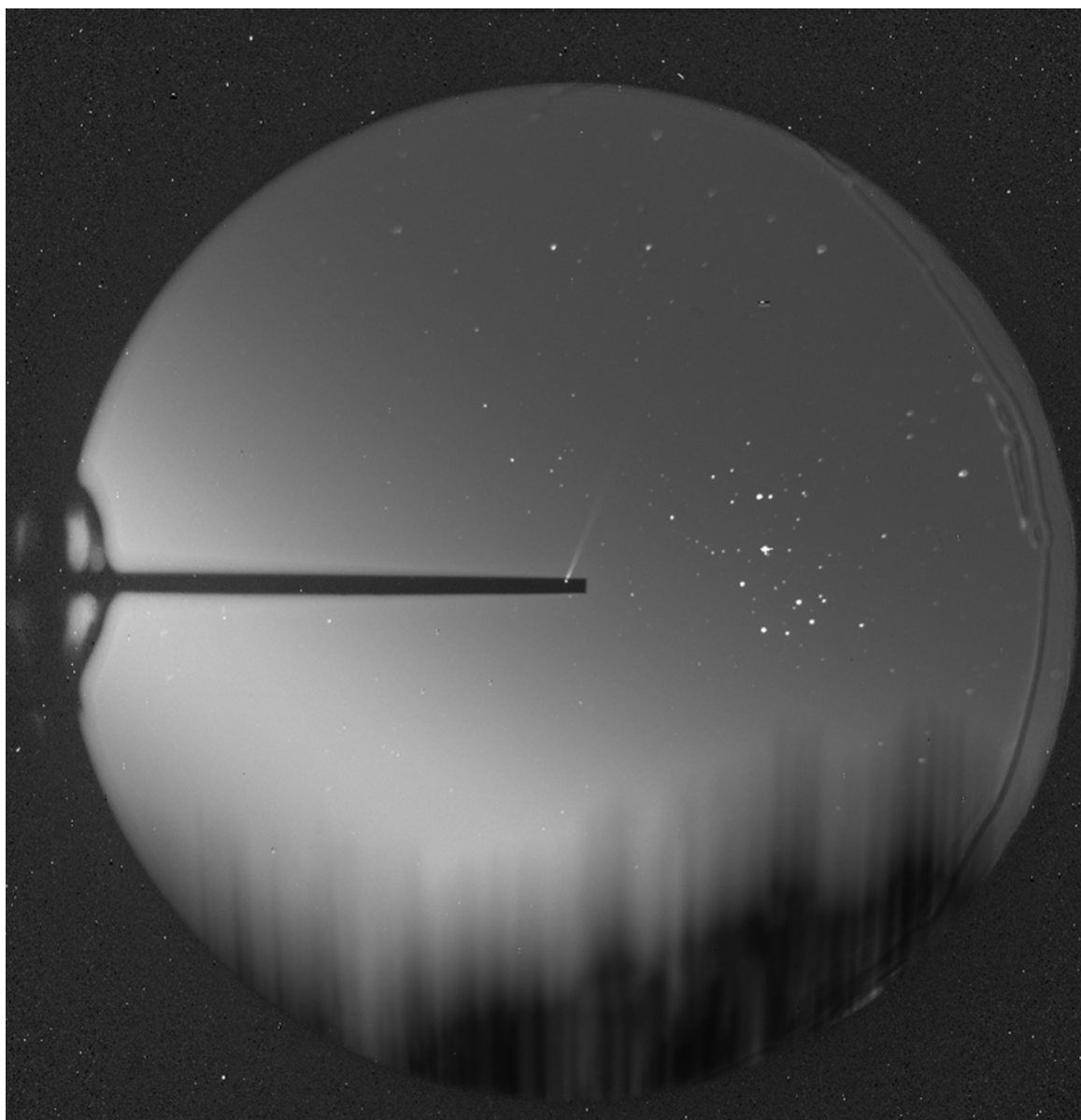


Figure 2.2 Example of a raw image from the wide-field coronagraph over a 350 second exposure taken UT April 30th 2009 02:45. Trees near the horizon in the lower portion of the image appear smeared, as they move through the field during the exposure. The neutral density filter protrudes horizontally, and obscures Mercury's bright disc at center. The long Na tail extends from Mercury, at the center of the frame, in the one o'clock direction. The Pleiades, just to the right of Mercury, contain standard stars used to calibrate the absolute flux and atmospheric extinction.

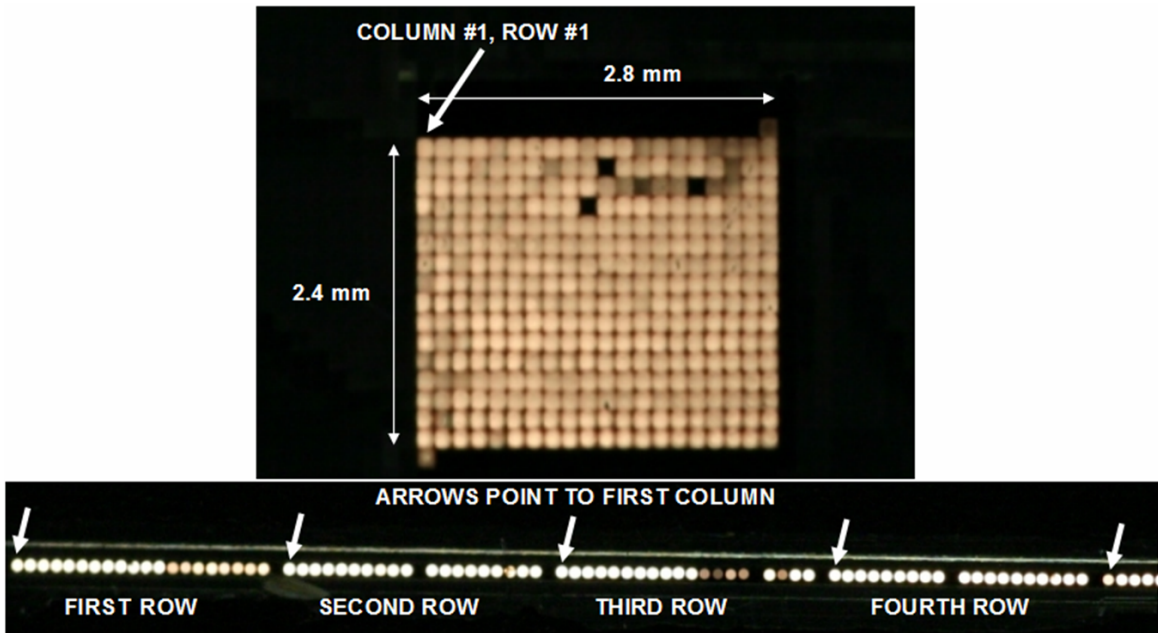


Figure 2.3 Images showing allocation of the fiber waveguides from two dimensions at the image plane (top) to a single line entering the spectrograph (bottom). The three dead fibers in the field are interpolated over, while fibers with diminished throughput are normalized to the same sensitivity in the flat fielding procedure.

This instrument has a $145\mu\text{m}$ spaced square lenslet matrix at the image plane of a 16 inch Schmidt-Cassegrain telescope. The lenslets have a focal length of 2 mm and are packed contiguously so that minimal light is lost between them. Each focuses incident light into a fiber-optic waveguide of $125\mu\text{m}$ diameter with a $100\mu\text{m}$ core. The bundle of 400 individual fibers is sent from the 20×20 matrix at the focus of the lenslet array to a single row at the spectrograph entrance. Mapping of this transfer from 2 dimensions to a single row is illustrated in Fig. 2.3. Upon passing through a slit entrance, the grating of the high resolution ($R \sim 60000$) spectrograph (Fig. 2.4) is pivoted so that wavelengths centered just between the D-line doublet will have first order diffractions that reach the detector at the center of the dispersion axis. A $\sim 40 \text{ \AA}$ FWHM filter is placed in the telescopes optical path so that higher order diffractions

at other wavelengths do not contaminate the spectra. In the current arrangement, each fiber/spectrum corresponds to a square region of sky with 7 arcseconds on a side. Not all the spectra physically fit on the 2.6 cm detector, however. Between 246 and 250 spectra are imaged simultaneously, so that the detector field of view is slightly cropped relative to the telescope image plane.

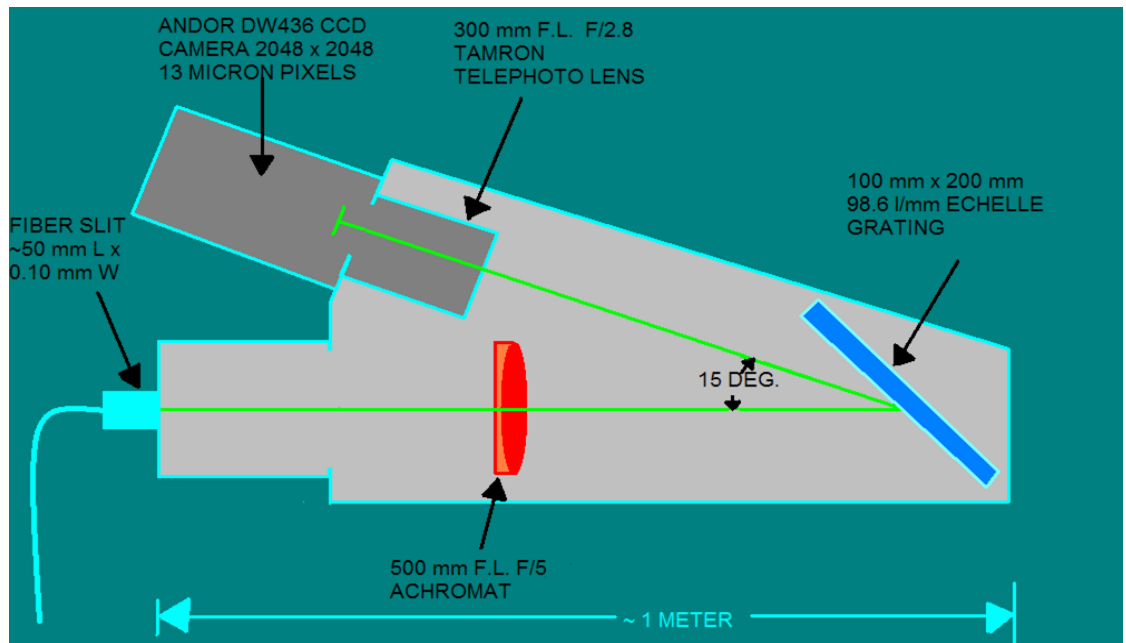


Figure 2.4 The optical layout of the high-resolution spectrograph.

“Unslicing” an Image

Like the coronagraph, the image-slicer records a range of wavelengths of light. However, rather than a fixed range of wavelengths over the filter pass-band, wavelength range can be specified directly over a chosen range of pixels in the dispersion direction since a spectrum at every spatial position is taken. Fig. 2.5 gives an example of a portion of the image slicer data for Mercury. Note that four distinctly different sodium D-line features exist in every spectrum: 1.) hermean exosphere emission, 2.) reflection

of sunlight off Mercury’s surface which features a Fraunhofer absorption line due to Na in the Sun’s atmosphere, 3.) terrestrial mesosphere Na emission and 4.) terrestrial atmospheric scattering of the solar Fraunhofer absorption. Feature 1 Doppler shifts are characterized by the line of sight velocity of the gas, while feature 2 is the sum of the Sun-Mercury and Mercury-Earth shifts, and features 3 and 4 are in the rest frame.

Notice that the spectral features are curved with respect to their horizontal position across the detector. Spectral lines passing through a straight slit are curved at the focal plane according to the grating equation (Schroeder, 1987). To correct for this, the curvature of Ne, He, Kr, and Na spectral lamps emission lines are measured, providing wavelength references commonly referred to as “arcs.” The curvature of the line centers in the arc frames are fit to a 2nd order polynomial. Resulting coefficients are applied in a 1-dimensional shift in the dispersion direction using bilinear interpolation. This un-warps the curvature in all science frames so that each wavelength corresponds to a uniform row of pixels across the CCD.

Using flat field continuum illumination, the location of all 246 spectra are automatically traced on the detector. Starting from the center of the dispersion axis, local maxima representing individual spectral positions are identified from a slice over the cross-dispersion axis. Assuming a Gaussian shape, these maxima are then fit and traced along both directions in the dispersion axis. As twenty individual parameters are passed to the tracing algorithm, for an in-depth discussion of this procedure the reader is referred to Section 3.1 of Sandin et al. (2010). Figure 2.6 shows the bottom left corner of a flat field continuum frame, after corrections for bias, dark and spectral curvature. Overlaid is the resultant aperture trace, where white lines indicate the aperture centers determined for each fiber at each wavelength bin. Note that the procedure of tracing the fiber apertures on the detector also identifies the eleven gaps between fibers and three broken fibers.

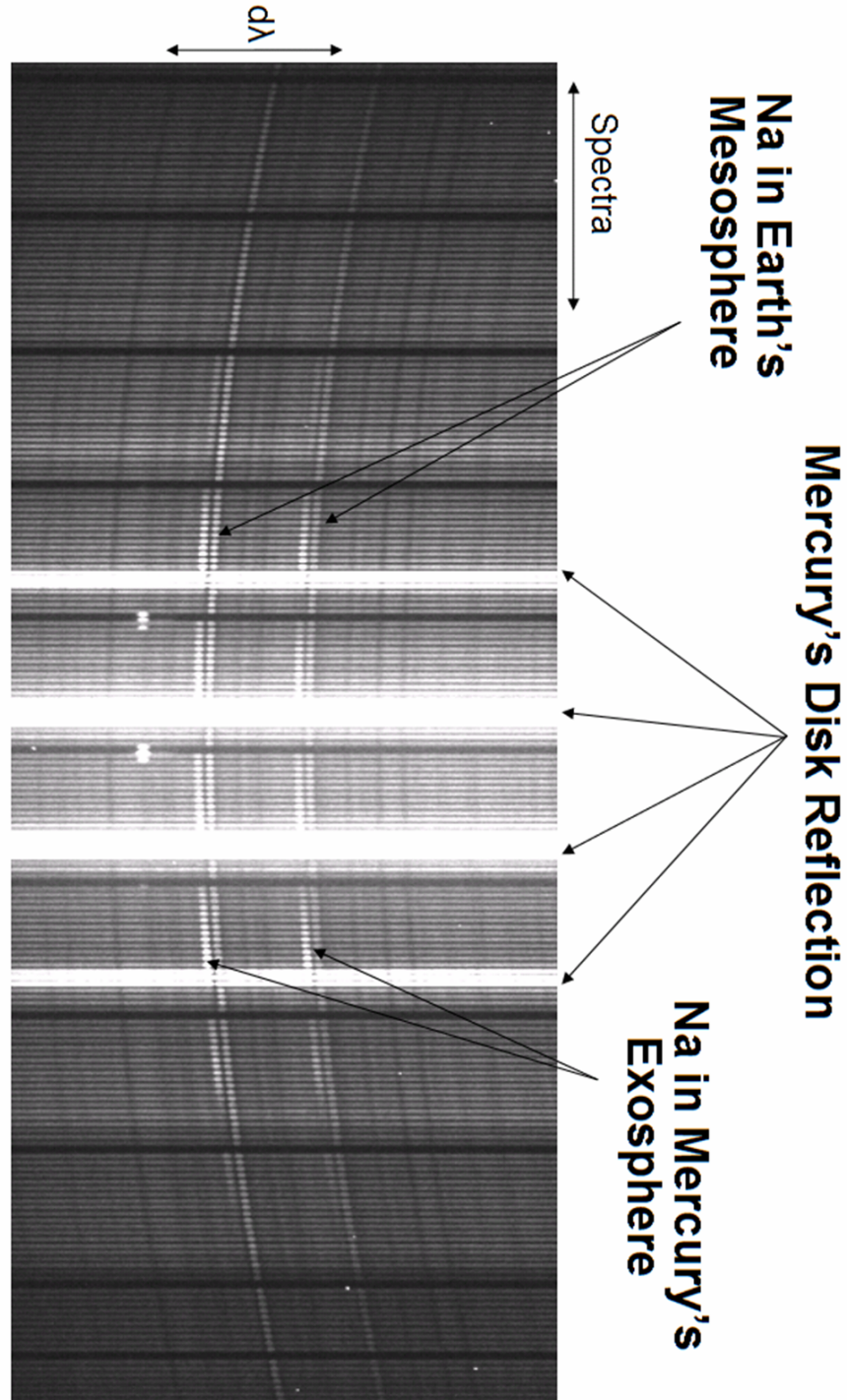


Figure 2.5 An example portion of a raw image of Mercury taken with the image slicing spectrograph at sodium D line wavelengths. The dispersion axis is vertical, and the two spatial dimensions are multiplexed. All fibers are illuminated by the twilight sky. Surface reflection of sunlight off Mercury's disk appears as bright continuum spectra at center. The hermean sodium doublet can be seen Doppler shifted just below the terrestrial mesospheric signature.

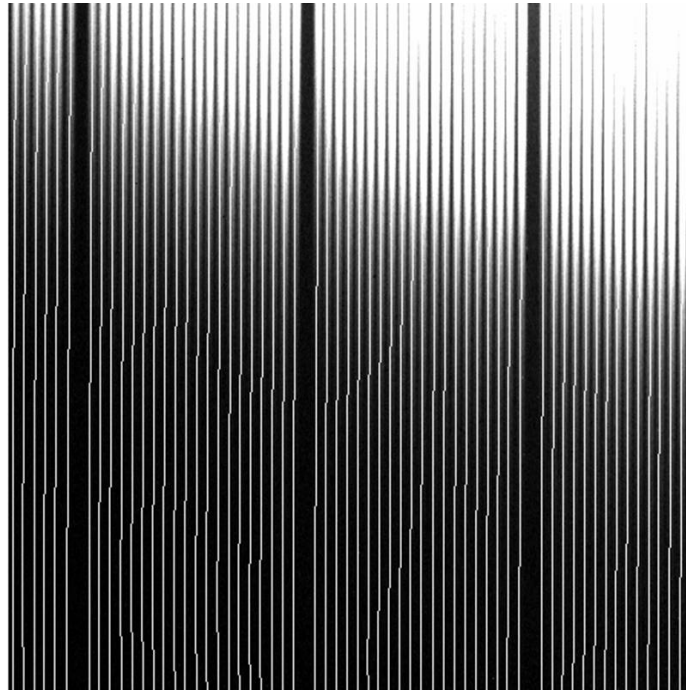


Figure 2.6 Calculated traces of the aperture centers for each spectrum from individual fibers. A small corner at bottom left of the 2048×2048 detector is shown for a continuum flat field frame. White lines indicate the the center of each fiber’s profile, determined in the tracing algorithm. Gaps can be seen each 20 fibers, marking the next row of fibers at the telescope image plane.

Traces shown in Fig. 2.6 are used as a template to identify the 246 individual aperture locations in all-sky, standard star, flat field and Mercury frames. At each wavelength bin, the cross-dispersion profiles are then integrated over a region spanning 3.3 pixels from the trace center. Partial pixels are counted via the fractional flux contained within them. Originally spreading over several pixels in the cross-dispersion axis, spectra after this extraction are only 1 pixel wide. Extracted spectra are held in a “row stacked spectra” (RSS) format, that is, a stacked output of dimensions the number of wavelength bins (2048) \times the number of spectra (246). Much of the subsequent data reduction is performed in the RSS domain, as this is the most intuitive way of visualizing the image-slicing spectrograph data.

The RSS format is easily converted to and from a 3-dimensional “data cube.” Spatial dimensions are re-allocated as seen in Fig. 2.3. Slices from the data cube can then be taken over a desired wavelength range. Each slice corresponds to a rectangular region of sky, i.e. an “un-sliced” image with dimensions 12 x 20 spatial pixels or “spaxels.”

2.4 Data Reduction

This section outlines the calibration procedure for both instruments in terms of the absolute surface brightness of emission from the sodium D-line doublet. The Rayleigh unit is adopted, being defined as 10^6 photons s^{-1} emitted from a 1 cm^2 column of atmosphere, where the emission is implicitly assumed to be isotropic (Hunten et al., 1956). Scattering of the D2 line is actually diminished by a few percent in viewing geometries where the Earth, Mercury and the Sun are near quadrature, as is ubiquitous here. Assuming the scattering phase function derived by Chamberlain (1961), a typical phase angle of 80° gives a 1% brightness correction for the doublet. Actual column abundances may therefore be $\sim 1\%$ greater than the isotropic determination used throughout this work, but this effect is considered small enough to be neglected.

2.4.1 Instrumental Corrections

Coronagraph Corrections

Standard bias, dark and flat corrections are made to each science and calibration frame taken by the coronagraph’s CCD. To eliminate cosmic ray counts and reduce statistical noise, the pixel by pixel median composite of a stack of at least five correction frames is used in each case. All dark corrections are normalized to the exposure time of the image being corrected. Flat field corrections are normalized by dividing

by the mode of the distribution of pixel counts. Due to instrument flexure, flat frames are imaged as close as possible to the telescope’s pointing direction during the science frames. Care is taken to ensure that the identical flat corrections are applied to science and calibration frames.

The passband of interference filters shifts toward shorter wavelengths with increasing angles of incidence. Although incidence angles are $<4^\circ$, this shift alters the transmission throughput for the D-line doublet by as much as 10%. A correction for this effect is discussed in the next section, 2.4.2.

Image-Slicing Spectrograph Corrections

The spectrograph housing unfortunately allows a small amount of ambient dome light to bleed through and reach the CCD detector. Contamination is not significant in science frames, even at twilight. However, flat field continuum frames taken with the dome halogen lamps on must be corrected for this light leak. A separate series of dark frames is therefore taken in conjunction with the flat fields under identical lighting conditions with the telescope aperture covered. Again using a median composite, these frames allow a separate “dark” correction which is specific to the flat field frames.

The location of the spectra on the detector is temperature sensitive, as the spectrograph itself is a large thermal mass with associated flexure. Given that the spacing between fibers is quite stable, the correction for variation in the location of the spectra can be automated in the reduction pipeline by taking a periodogram in the cross-dispersion axis. In this way, calibration and data frames need not be taken at precisely the same temperature. A shift in aperture positions along the cross-dispersion axis is applied when extracting the science spectra, with the shift amount determined by the difference in the indices of the periodogram maxima.

Science and calibration frames taken with the image-slicing spectrograph’s CCD are scrubbed for cosmic rays using the L.A. Cosmic algorithm (van Dokkum, 2001).

Standard bias and dark corrections are made for each science and calibration frame (e.g., Howell, 2006). Dark current corrections are normalized to the exposure time of each image being corrected, and the pixel by pixel median composite of a stack of at least three correction frames is used to eliminate cosmic ray counts and reduce statistical noise. Flat field corrections of this instrument are less intuitive, however. Dividing a raw image by a raw continuum flat field would amplify noise in the wings of each fiber’s spectral profile. For this reason, flat corrections are made post-extraction in the data reduction pipeline. After smoothing with a median filter in the dispersion axis, values are normalized by the mode of the count distribution in all fibers. The non-uniform throughput for each fiber channel is then corrected by dividing the resultant flat in the RSS domain. Figure 2.7 shows an example from 21 December 2011 at this point in the reduction pipeline.

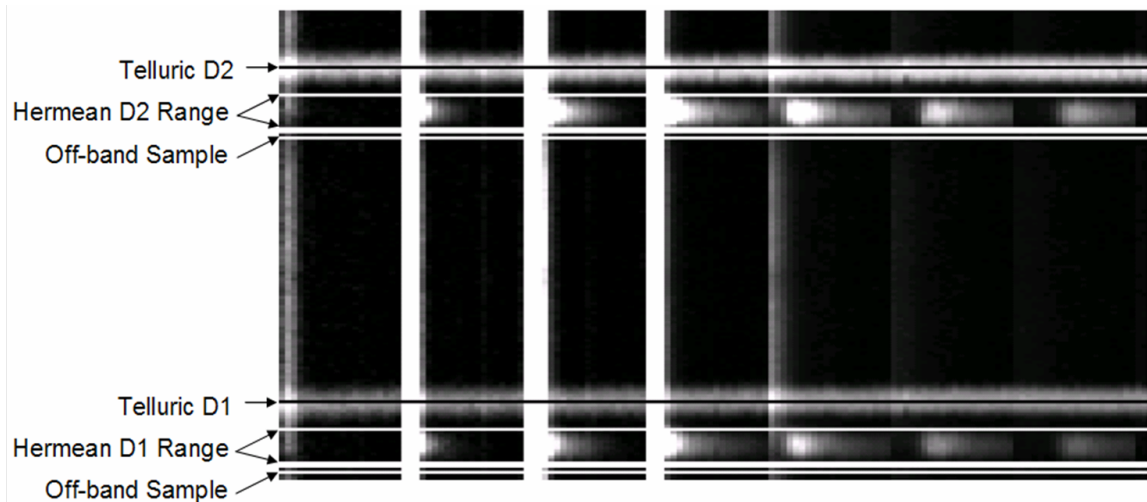


Figure 2.7 Data from the image-slicing spectrograph that has been extracted into the row stacked spectra (RSS) format. Telluric rest wavelengths for D1 and D2 are used as a reference when correcting for Doppler shifts in the hermean surface reflectance and exosphere emissions. Mercury’s exospheric emission is summed over the indicated range. Following sky, surface reflectance and scattered light subtraction, the off-band samples are used to correct for residual systematic errors.

Spectra must be corrected for the background emission of the twilight sky. A sky correction is built from a composite of the spectra in each science image which have the lowest counts at the sodium D lines and are far from the Mercury's disc. A median of this pool of fibers is taken over the cross-dispersion axis at each wavelength bin. The resulting background sky spectrum is subtracted from every spectrum in the science frames. This method benefits from the sky levels being measured directly, rather than scaled from an additional calibration frame. This sky subtraction corrects for terrestrial Na emission in Earth's mesosphere, although the Doppler shift is at times large enough that hermean and telluric D-line emissions are not degenerate, as is the case in Figure 2.7.

Scattered sunlight reflected from Mercury's surface is also subtracted. This is implemented using the surface reflected spectra of Ganymede, admittedly a relic of the instrument's original purpose. The Ganymede spectrum is shifted to the Earth-Mercury Doppler shift at the observing time and scaled by the ratio of integrated flux in broad-band continuum wavelengths. This subtraction is only applied to fibers within several arcseconds of Mercury's disk. Given that the surface reflectance exceeds exospheric emissions by several orders of magnitude, a relatively large uncertainty persists in the brightness near the planet's disk.

An additional source of error is scattered light within the image slicing spectrograph itself. A small fraction of sunlight reflected from the planet's surface arrives at the detector off-axis from the optical path, especially for fiber rows that contain bright light from the disk of the planet. This contamination is corrected for in two ways. First, using an aperture mask over a raw image, the flux contained in fiber gaps >5 pixels from any spectrum is smoothed with a median filter. Gaps close to Mercury's disk are omitted from the sample as they lead to over subtraction. Values in the cross-dispersion axis are fit with a least squares quadratic for one pixel on the

dispersion axis at a time. The result is smoothed using a convolution with a Gaussian kernel to reduce noise. An identical extraction is performed on this scattered light result so that it can be subtracted in the RSS domain. The second method of scattered light removal is then applied — simple off-band subtraction. As the Mercury and sky components have already been removed, wavelength bins adjacent to the D-lines should ideally have zero values. Constructing a data reduction pipeline that repeatably achieves this is exceedingly difficult, however. Off-band regions are carefully chosen immediately adjacent to the hermean D-line emission, in the direction opposing the Doppler shifted terrestrial emission (cf. Fig. 2.7). The median value of several pixels along the dispersion axis is subtracted from each spectra.

2.4.2 Filter Characterizations

Narrow-band interference filters used in the coronagraph instrument must be calibrated in two ways. First, the overall integrated passband must be determined. This passband is needed for characterization of the instrumental response to continuum emission from a known standard, in this case blue spectral type standard stars. Second, the transmission to sodium D1 and D2 line emissions must be determined. The transmission is needed to calculate the attenuation of sodium D line emission and recover the flux entering the telescope aperture. This section describes the procedure for each filter calibration.

The filter passband calibrations were performed in the NSF-sponsored Calibration Facility in the Imaging Science Laboratory at Boston University. First, a solar spectrum was fed from a heliostat and imaged through a high resolution spectrograph like that in Fig. 2.4. The location of Fraunhofer absorption lines along the dispersion axis of the CCD was fitted with a second order polynomial. This provides an accurate wavelength reference for each position across the detector. Second, a tungsten lamp spectrum was taken, allowing time for the filament to achieve thermal stability.

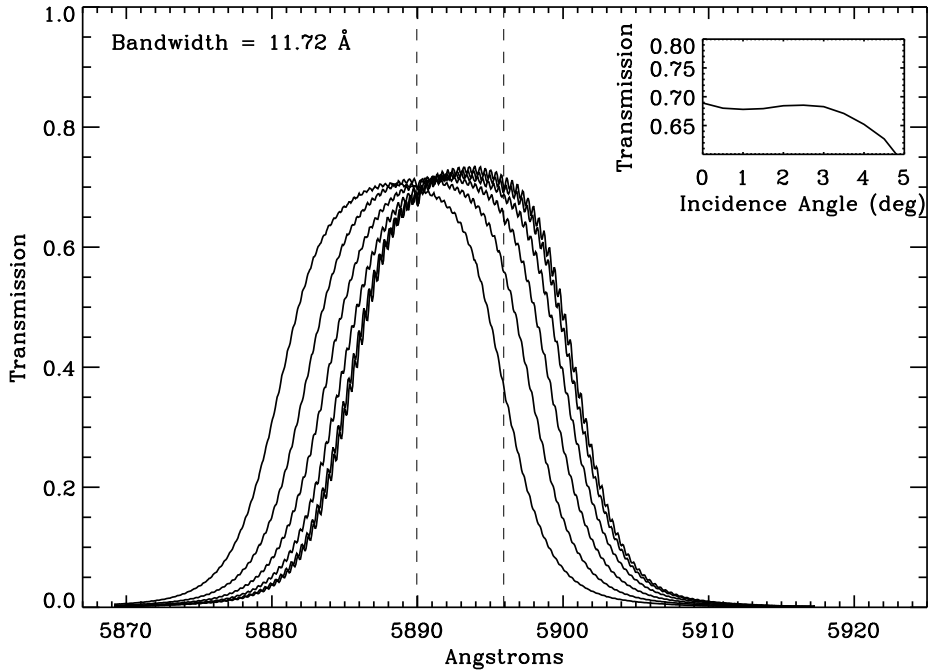


Figure 2.8 Properties of the interference filter used in initial studies of the distant sodium tail in 2007. The wave structure in the profile created an unwelcome ringed pattern in the images which was fit and divided out visually.

Third, this same tungsten spectrum was imaged, this time with the narrow-band filter in the optical path. Fourth, to estimate the effects of off-axis light, the filter was tilted relative to the optical path in degree steps, with additional spectra taken at each tilt angle.

After routine corrections for the bias level and dark current of the CCD, dividing the filtered tungsten spectra by the unfiltered tungsten spectra yields the filter's transfer function, that is, the transmission versus pixel position. The polynomial fit from the first step then gives the transfer function in terms of wavelength. Figures 2.8 - 2.10 show the transfer functions for the three narrow-band filters used in this study. The quality of each successive filter is an improvement from the previous one. The

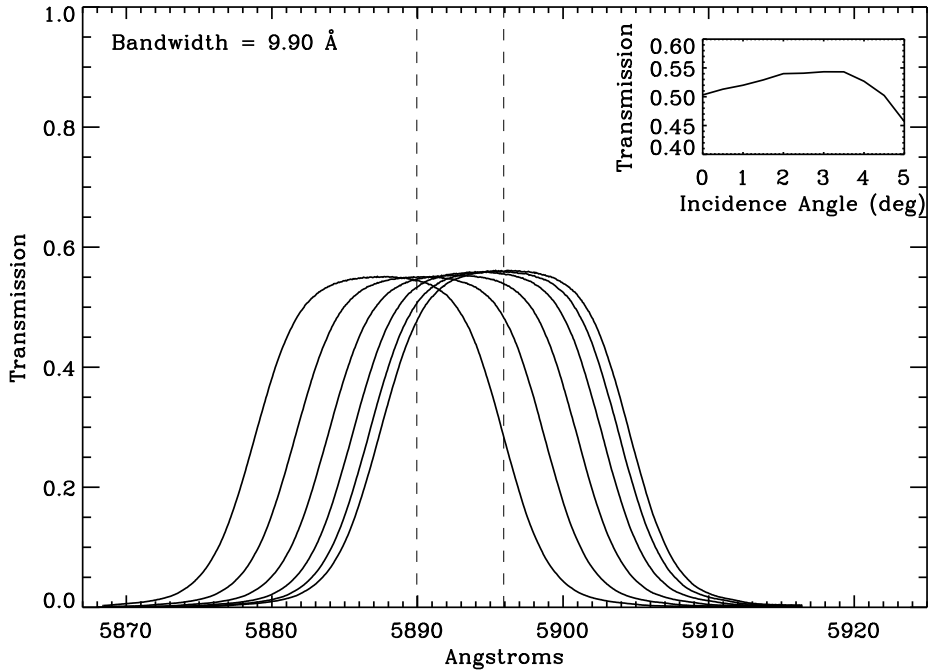


Figure 2.9 Properties of the interference filter used in 2008 measurements. This filter was selected because of the smoothness of the transmission profile, however throughput for D-line emission was diminished by $\sim 30\%$ compared to the previous filter in Fig. 2.8

passband of the filter shifts blue-ward when the filter is tilted. The rightmost profile shows perpendicular light. At degree increments, up to 5° tilt are seen in each profile shifted successively blueward. The overall bandwidth of the filter is shown at the top left in each figure, calculated from the area under the profiles.

In optically thin sodium emission, the D2 transition is twice as bright as D1, scaling with the number of sub-levels in the excited state. The inset plots of Figures 2.8 - 2.10 show the weighted average of each filter's transmission at D-line doublet wavelengths versus the incidence angle of the tungsten filament rays. Since the coronagraph accepts light at angles up to 4° , these inset plots reveal that the transmission varies across the detector by up to 10%. Measured D-line transmission is interpolated

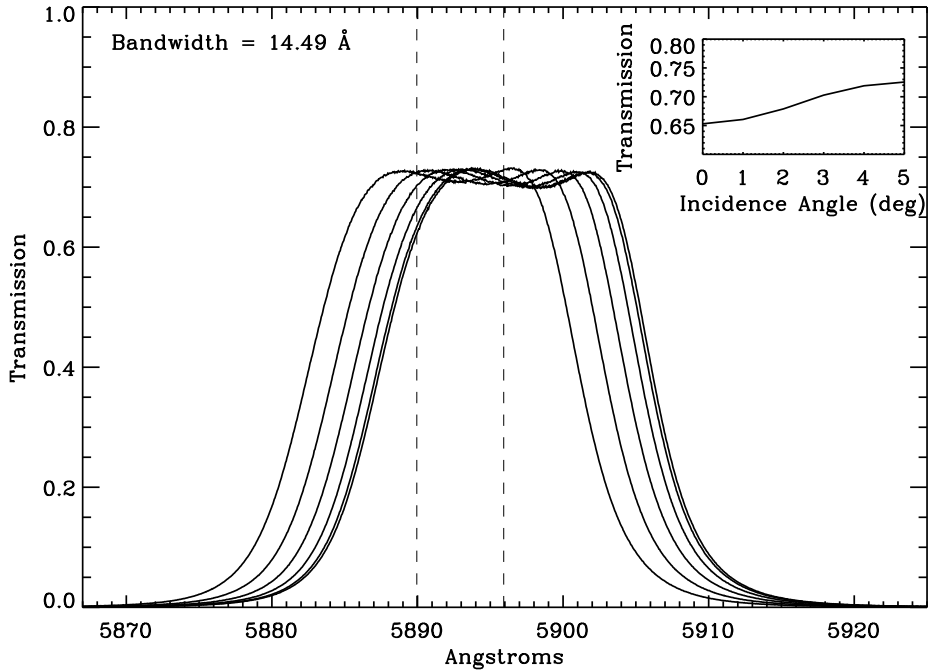


Figure 2.10 Properties of the interference filter used from 2009 onward. This filter was selected to optimize transmission while preserving a smooth transmission profile.

over these angles to calculate the transmission at each pixel using the coronagraph's plate scale. The resulting map of the D line transmission at the detector is then divided out, in order to recover the flux of the sodium doublet emission entering the telescope.

Initial attempts at calibrating the D-line transmission relied on imaging a low pressure sodium lamp, both with the filter in and out of the optical path. Dividing these two images to yield the D line transmission, however, did not produce the desired result. A wood-grain structure in the resulting image was an artifact of phase interference at far red wavelengths, where silicon is transparent enough that incident photons can reflect off detector layer interfaces. This provided evidence that the detector had recorded substantial at the far red end of the visible spectrum. The

spectrum of a low pressure sodium lamp contains both Na emission at 8195 Å, and trace emission features from the Penning mixture of neon and argon, that is, more than the intended D-line emission alone. As such, this method cannot isolate the instrumental throughput to D-line emission without additional filtering of the lamp, and hence was abandoned in favor of the laboratory measurement.

The interference filter in the image-slicer's optical path is used only to eliminate other wavelengths, with higher orders diffracted by the grating, from hitting the detector. Unlike the coronagraph, the filter on the image-slicing spectrograph does not need calibration for spectro-photometry.

2.4.3 Standard Star Calibrations and Atmospheric Extinction

All data were recorded when Mercury was at an elevation less than 15° from the horizon. Measured fluxes by both instruments are therefore heavily dependent on the atmospheric conditions. For this reason, standard stars measurements are used for calibration, as this method allows nightly estimates of the atmospheric extinction. Calibration is performed using standard stars that have a known and stable spectro-photometric brightness (Burnashev, 1985). O and B type standard stars are preferentially selected in order to minimize stellar features at the Na D-line doublet. White dwarf stellar types would also make suitable standards, however their faint apparent magnitudes are generally less favorable.

The altitude of the standard star is determined from its right ascension and declination, and the time at the middle of the exposure. Given these three parameters, a rotation matrix converts between the equatorial and horizontal coordinate frames. The conversion between these coordinate frames is described in numerous observational astronomy texts and hence not discussed here. Extinction of the standard star's flux is then fit to the form:

$$I(z) = I_0 e^{-kM(z)} \quad (2.1)$$

were I_0 represents the airless flux of the star in units of data number (DN) per second and k is the atmospheric extinction coefficient per unit vertical atmosphere. Eq. 2.1 implicitly assumes the extinction is uniform in composition, as corrections for non-hydrostatic extinction in layers requires a much more rigorous solution. At the low elevation angles of interest, refraction becomes significant to the extent that the airmass, M , no longer scales simply as the cosine of the true zenith angle, z . Rather, the airmass is estimated in the calibration of both instruments using a formula reached empirically by Young (1994) as:

$$M(z) = \frac{1.002432(\cos z)^2 + 0.148386 \cos z + 0.0096467}{(\cos z)^3 + 0.149864(\cos z)^2 + 0.0102963 \cos z + 0.000303948} \quad (2.2)$$

A least squares fit is used to solve for I_0 and k in equations 2.1 and 2.2 given a set of I versus z data points as a standard star rises or sets near the horizon. Thus, the sensitivity and extinction parameters are determined simultaneously each night by measuring the decrease in flux as a function of elevation angle. As Earth's atmospheric conditions vary on timescales of minutes, the flux of spectrophotometric standard stars in the (Burnashev, 1985) catalog is measured by both instruments as closely as possible to the science data. For the coronagraph, a standard star is occasionally in the same field of view as Mercury.

Photometry

In reducing the image-slicing spectrograph data, background sky spectra are subtracted from the entire field so that photometry can be performed subsequently by simply totaling the counts. After normalizing the exposure times, all standard star

spectra in the RSS format are summed, producing an array of the star's DN s^{-1} for each wavelength bin integrated over both spatial dimensions.

Standard star fluxes recorded by the coronagraph are determined via circular aperture photometry, utilizing the NASA Astrolib IDL routine “aper.pro” for sky subtraction. A two-dimensional Gaussian is fit to the point spread function of each standard. The peak of the fit is used as the centroid of a circular aperture around each star, where three times the fitted FWHM is the aperture radius (Howell, 2006). The background sky is sampled over an annulus 3.5 - 5 times the FWHM. Partial pixels from the projection of a circle on the square grid are weighted by the ratio of area enclosed. The photometry program automatically rejects measurements of stars that either 1.) approach non-linear saturation above 2^{16} counts or 2.) have a signal to noise ratio of less than three, calculated by summing in quadrature the scatter in sky values, the random photon noise and the uncertainty in sky brightness.

2.4.4 Calibration and Reduction Procedures

Coronagraph Procedure

Once bias, dark and flat corrections have been made, all science and calibration frames were divided by the two dimensional transmission of the filter, as determined in the laboratory and described in section 2.4.2. This accounts for D-line flux which entered the telescope but did not pass through the filter in order to reach the detector. Next, the standard's spectrophotometric flux in $\text{photons s}^{-1} \text{cm}^{-2} \text{\AA}^{-1}$, as cataloged by Burnashev (1985), were multiplied by the filters passband determined in section 2.4.2. This gives the standard's flux in $\text{photons s}^{-1} \text{cm}^{-2}$ that are capable of being registered by the instrument in the absence of attenuation by the Earth's atmosphere. Since the star's radiation is isotropic, the flux received in a given pixel will be that pixel's projected area on the sky at some arbitrary distance $R\theta^2$, divided by the surface area of the great sphere at this distance, $4\pi R^2$. This yields the relation:

$$F = I \frac{\theta^2}{4\pi} \quad (2.3)$$

Solving for I and converting to units of Rayleighs gives the star's surface brightness:

$$I_{Rayleighs} = 10^{-6} F \frac{4\pi}{\theta^2} \quad (2.4)$$

The sensitivity, $S(z)$, of the instrument as a function of altitude was found by dividing Eq. 2.1 by Eq. 2.4, that is, the recorded data number (DN) per second divided by the star's surface brightness. The units of sensitivity are $DN s^{-1} R^{-1}$, and this yields the relation:

$$S(z) = S_0 e^{-kM(z)} \quad (2.5)$$

Iterating this procedure over many nights gives independent estimates of the instrument sensitivity in the absence of atmospheric attenuation, S_0 , which should remain constant provided the detector and instrument transmission are stable. In all calibrated data using the filter in Fig. 2.10, the \bar{S}_0 was determined to be $0.038 \pm .005$ $DN s^{-1} R^{-1}$. Once this airless sensitivity is established, calibration becomes one step recursive, as I_0 can be solved directly as $\bar{S}_0 \times I_{Rayleighs}$, rather than with a least squares fit. The only fit variable in the calibration thus becomes the atmospheric extinction coefficient per unit vertical airmass, k .

The apparent zenith angle for a given pixel location in an image, $z_{App}(x, y)$, can be determined as:

$$z_{App}(x, y) = P \frac{\Delta x}{\cos \phi} + z_M = P \frac{\Delta y}{\sin \phi} + z_M \quad (2.6)$$

where $\Delta x, \Delta y$ are pixel distances from Mercury's detector location, z_M is Mercury's zenith angle at the time of mid-exposure, P is the telescope plate scale in radians per

pixel, and ϕ is the angle between the meridian and the x-axis of the detector chip. Since the telescope is mounted equatorially, the x-axis is parallel with right ascension so that ϕ is easily computed (actually, a 3° visually determined offset is accounted for). After bias, dark, flat, and transmission corrections are applied, dividing an image by the extinction corrected sensitivity, Eq. 2.5, at each pixel using Eq. 2.6, gives a calibrated image in Rayleighs. At this step, a conversion between true and apparent zenith angles is made (Meeus, 1998), as atmospheric refraction significantly curves light rays near the horizon.

Exposures ranging from 30 seconds to 5 minutes were possible in the fading twilight without saturating the detector. Since the sodium in Earth's mesosphere (~ 90 km in altitude) was also imaged, terrestrial emissions in columns on both sides of the tail were fit and subtracted from each image in order to isolate the Hermean emission. This background from resonant scattering in the Earth's mesospheric sodium layer is the principal factor that affects the signal to noise ratio. Fig. 2.11 shows the regions sampled for the terrestrial Na emission as a function of altitude. The median value of a pixel row of constant altitude is taken on each side of the tail and averaged. A third order polynomial is fit to these values as a function of elevation angle and subtracted from the image to remove the terrestrial component and isolate Hermean emission. Notice that Fig. 2.11 is aligned in ϕ . A rotation matrix over ϕ was applied pivoting about Mercury's location. Terrestrial subtraction is performed in the unrotated frame, so that no interpolation of pixel values is required.

After subtracting terrestrial emission from each image, visually selected best frames are combined into a single image for each night of data. Telescope flexure slightly varies between the guide camera and the coronagraph. To correct for this, exposures are shifted to co-align Mercury's pixel centroid to a reference image. Bilinear interpolation is implemented allowing sub-pixel shifts. The best images of the tail are

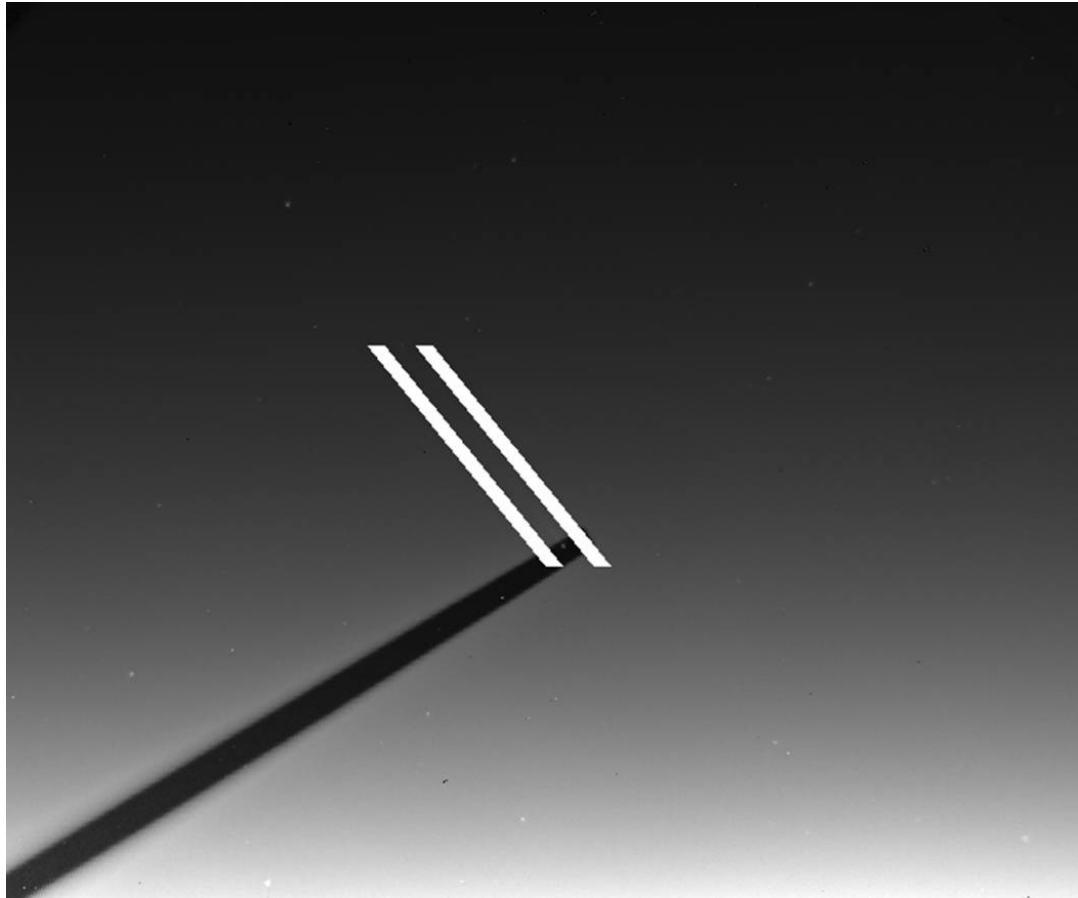


Figure 2.11 Sampled regions used for fitting and subtracting terrestrial Na emissions in Earth's mesosphere, shown in white. Hermean emission in the tail is centered between the these white columns. This image has been rotated so that the horizon is parallel with the horizontal axis. The neutral density filter occulting mask extends from bottom left. The vertical gradient throughout the field is due to combined emission from resonantly scattered Na in Earth's mesosphere, and twilight scattered solar continuum.

then stacked into a three-dimensional array and a composite (median) image is created from the median of the stack at each pixel. The result is then rotated to align the tail in the y axis and cropped to the region of interest. The rotation angle is between the x-axis (constant declination) and the Sun-Mercury vector, allowing the rotation to be automated in the reduction pipeline via SPICE ephemerides (Acton, 1996). Final images are displayed in Sec. 2.5.1. Note that the final two steps, shifting and rotating, required bi-linear interpolation of pixel values. These are the only interpolations of pixel values used throughout the reduction procedure.

Image Slicing Spectrograph Procedure

Calibration of the image slicer data is carried out much in the same way as the coronagraph, but with the absolute flux determined per unit wavelength bin, rather than over a filter passband. Wavelengths registered by a coronagraph pixel span the entire filter passband, and a standard star's spectrophotometric flux is thus multiplied by $\sim 14 \text{ \AA}$ to give I in Eq. 2.3. Wavelengths registered by a pixel on the image slicer detector span a small fraction of an \AA . In this case, a standard star's flux in $\text{photons s}^{-1} \text{ cm}^{-2} \text{ \AA}^{-1}$ is multiplied by the spectrograph's dispersion to give the flux per wavelength bin of the instrument, i.e., the flux per pixel along the dispersion axis of the detector. Using Eq. 2.3, where θ is the angular width of a spatial element, the incident surface brightness of the star is calculated over the spectral range of a single pixel along the instrument's dispersion axis.

After corrections and extraction, the average recorded flux in the star's continuum region between the D lines is tallied in DN s^{-1} as a function of the true elevation angle and fit to Eq. 2.1. Dividing an image by the sensitivity after the atmospheric extinction correction, Eq. 2.5, interpolated at Mercury's elevation angle mid-exposure, gives a result in Rayleighs at each wavelength bin. Whereas the coronagraph requires isolating hermean emission from the background, the emission in the spectrograph

is summed over the line width along the dispersion axis. After correcting for the planet’s Doppler shift using SPICE epherides, the sum over several pixel rows gives the brightness in Rayleighs that is intrinsic to Mercury.

Simultaneous measurements with the image slicing spectrograph can be cross-calibrated with the coronagraph, after normalizing for both exposure time and elevation angle. The total surface brightness of a standard star in Rayleighs, integrated over the bandwidth of the coronagraph’s filter, can be cross-calibrated to that measured by the coronagraph’s CCD. In principle, this technique would also work for Mercury frames with the planet out from behind the occulting mask and short integration times.

With the aid of flexure between the 16 inch and guide telescopes at low elevation angles, images of the planet are intentionally dithered within the field of view. This permits a higher resolution image to be made from the composite of several individual frames, and aids in lowering the residual noise floor from flat fielding errors. The centroid is determined by weighting the off-band brightness over five spatial elements and is again used to shift and co-align the images from a given night. Each slice is re-sized to 24×40 spatial elements, without interpolation, and placed in a stack. The pixel by pixel median value of the stack is then used as a final composite image for each night, the result having twice the resolution of the individual frames.

2.5 Data Acquired

Table 2.1 summarizes the conditions for the observing runs used in this study. The true elevation angle of Mercury at sunrise / sunset is given in the last column and is a proxy for the background emission levels that govern signal to noise. Observations frequently overlap the same orbital longitudes. The true anomaly angle, TAA, is the angle between perihelion, the Sun, and Mercury. Heliocentric velocity, V_R , and

Table 2.1. Sodium D Line Observations of Mercury at McDonald Observatory
2007-2012

Campaign	UT Date	TAA (deg)	V_R (km s^{-1})	P_{Rad} (cm s^{-2})	Range (AU)	Elevation (deg)
(1)	(2)	(3)	(4)	(5)	(6)	(7)
1	31 May 2007	114	9.19	129.9	0.404	20.5
1	2 June 2007	121	8.62	116.8	0.415	20.6
1	3 June 2007	124	8.39	111.4	0.420	20.6
2	12 Nov. 2007	69	9.37	180.9	0.345	16.4
3 ^M	15 Jan. 2008	287	-9.65	182.1	0.350	13.1
4	18 May 2008	118	8.88	122.7	0.410	18.8
5	6 July 2008	275	-10.03	171.4	0.365	15.6
6 ^T	19 April 2009	46	7.27	159.0	0.325	16.5
6 ^T	20 April 2009	52	7.92	171.0	0.329	17.2
6 ^T	21 April 2009	57	8.47	177.6	0.334	17.8
6 ^T	22 April 2009	63	8.94	180.5	0.339	18.4
6 ^T	24 April 2009	73	9.61	179.3	0.350	19.2
6 ^T	27 April 2009	87	10.04	168.2	0.367	18.7
6 ^T	30 April 2009	100	9.92	152.3	0.384	18.5
6 ^T	1 May 2009	104	9.77	146.11	0.390	18.3
7	12 Dec. 2009	256	-9.78	148.7	0.389	11.8
7	17 Dec. 2009	278	-9.96	175.5	0.360	13.8
8	4 April 2010	35	5.73	115.1	0.317	16.6
8	5 April 2010	41	6.55	140.9	0.321	17.1
8	6 April 2010	46	7.05	156.3	0.324	17.6
8	7 April 2010	52	7.92	171.0	0.329	18.0
8	8 April 2010	57	8.48	177.8	0.334	18.2
8	11 April 2010	73	9.61	179.3	0.350	17.4
8	12 April 2010	78	9.83	177.1	0.355	17.3
8	14 April 2010	87	10.04	168.2	0.367	16.7
9	3 Jan. 2011	90	10.06	165.7	0.370	17.1
9	5 Jan. 2011	98	9.96	155.2	0.381	17.3
9	8 Jan. 2011	110	9.47	136.4	0.399	17.1
9	9 Jan. 2011	114	9.21	130.2	0.404	16.9
9	10 Jan. 2011	117	8.94	124.0	0.409	16.7
9	12 Jan. 2011	128	8.31	111.0	0.419	16.2
9	13 Jan. 2011	131	7.96	103.6	0.424	15.9
9	14 Jan. 2011	134	7.59	95.2	0.429	15.6
10 ^{M,H}	3 July 2011	110	9.55	139.4	0.396	15.7
10 ^{M,H}	4 July 2011	114	9.31	132.6	0.402	16.1
10 ^{M,H}	5 July 2011	117	9.06	126.6	0.407	16.4
10 ^{M,H}	6 July 2011	121	8.76	120.1	0.412	16.7
10 ^{M,H}	7 July 2011	124	8.45	113.7	0.417	16.9
10 ^{M,H}	8 July 2011	128	8.11	106.7	0.422	17.1
10 ^{M,H}	9 July 2011	131	7.75	99.3	0.426	17.3
10 ^{M,H}	10 July 2011	134	7.37	90.9	0.431	17.4
10 ^{M,H}	16 July 2011	152	4.83	39.6	0.452	17.1
11 ^M	21 Dec. 2011	90	10.06	164.8	0.371	17.7
11 ^M	22 Dec. 2011	94	10.03	159.3	0.377	17.6
11 ^M	26 Dec. 2011	110	9.43	135.95	0.399	17.3
11 ^M	28 Dec. 2011	118	8.90	122.9	0.410	16.5
11 ^M	29 Dec. 2011	121	8.60	116.5	0.415	16.1
11 ^M	30 Dec. 2011	125	8.27	109.9	0.420	15.7
12 ^{M,H}	15 June 2012	93	10.05	162.0	0.374	15.9
12 ^M	17 June 2012	101	9.88	150.3	0.386	17.0
12 ^{M,S}	18 June 2012	105	9.72	144.8	0.391	17.4
12 ^{M,T,S}	19 June 2012	109	9.52	138.3	0.397	17.9
12 ^{M,T,S}	20 June 2012	113	9.29	132.4	0.402	18.2
12 ^{M,H,T}	21 June 2012	116	9.03	125.6	0.408	18.5
12 ^{M,H,T}	22 June 2012	120	8.73	119.8	0.412	18.8
12 ^{M,H}	23 June 2012	123	8.41	112.7	0.418	19.0
12 ^{M,H}	24 June 2012	127	8.07	105.6	0.423	19.2
13 ^M	28 Nov. 2012	45	7.17	159.0	0.324	16.3
13 ^M	29 Nov. 2012	51	7.83	169.9	0.328	16.7
13 ^M	30 Nov. 2012	57	8.40	177.4	0.333	17.9

^MSimultaneous with MESSENGER^TSimultaneous with THEMIS Observations^HSimultaneous with Haleakala Observations.^SSimultaneous with McMath-Pierce Observations.

radiation pressure, P_{Rad} , are periodic functions of TAA, and the combined framework provides a convenient metric for seasonal studies. Three observing campaigns were coordinated in conjunction with groups at other observatories as part of the International Mercury Watch initiative. At the beginning of each run, the telescopes were co-aligned so that data can be recorded simultaneously in both instruments.

2.5.1 Wide-field Coronagraph: Distant Tail

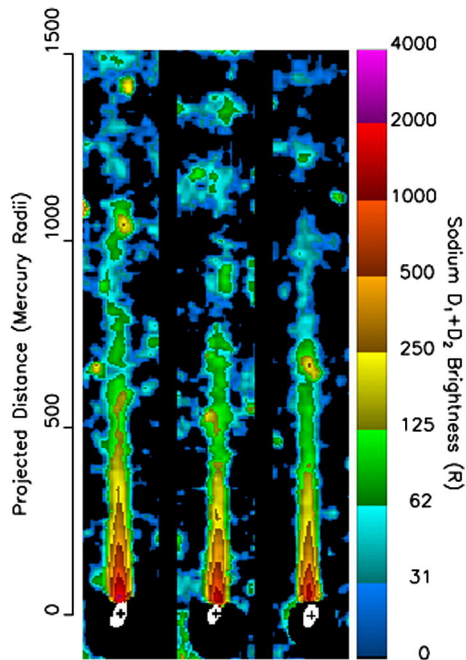


Figure 2.12 Coronagraph observations from the May to June 2007 elongation, calibrated in Rayleighs. The Sun is in the downward direction and the plus symbol at bottom center represents Mercury's position behind the occulting mask. The surrounding region in white is the 1σ uncertainty level in Mercury's position. (Left to right) UT 31 May 2007, 2 June 2007, and 3 June 2007.

Since May 2007 13 observing campaigns, each taken with Mercury near maximum elongation, have been collected using Boston University's 10 cm coronagraph telescope at the McDonald Observatory. The first coronagraph image was presented

by Baumgardner et al. (2008), and weather conditions in the days following permitted accurate imaging on 2 June 2007 and 3 June 2007. This data set was the only elongation out of the first 5 observing runs in which the tail was observed, and weather conditions allowed photometric imaging for more than one night. The 12 November 2007 observation yielded the brightest tail recorded thus far in any study of the Mercury exosphere. 15 January 2008 data was taken in conjunction with the first MESSENGER fly-by. Ground-based observations were not possible during the second fly-by on 6 October 2008, as Mercury was only 2° in angular separation from the Sun. Observations on 18 May 2008 were taken during nearly the same orbital phase as those of the previous summer, and the signal of sodium emission in the tail was strong enough that higher resolution was achieved by 1×1 binning the CCD. Prior to this date, 2×2 pixel bins were summed to give higher signal at the cost of lower resolution. Observations on 7 July 2008 closely matched the orbital phase of those taken during the first MESSENGER fly-by, but with much better observing conditions.

Calibrated images from the first seven observing dates are shown in Fig. 2.12, Fig. 2.13 and Fig. 2.14. Five of these seven observation dates show a tail that visibly extends several hundred Mercury radii. Fig. 2.12 reveals changes in the tail over just a few days: 31 May 2007, 2 June 2007, and 3 June 2007. Fig. 2.13 shows changes on a much longer timescale of observations over nearly 1 year: 3 June 2007, 12 November 2007, and 18 May 2008. Before the neutral density filter was implemented in 2009, Mercury’s position under the occulting mask was found by interpolation from the azimuth and altitude of neighboring stars. The region in white gives the 1σ uncertainty ellipse in Mercury’s position. The down-tail distance scale, given at the left side of these plots, accounts for the projection of the tail’s anti-sunward direction in the plane of the sky. This scale was calculated using the SPICE (Spacecraft Planet Instrument C-matrix Events) ephemerides as:

$$\frac{Distance(R_M)}{Pixel} = \frac{\alpha}{2P \sin(\pi - \angle SME)} \quad (2.7)$$

where P is again the coronagraph's plate scale in radians per pixel, $\angle SME$ is the Sun-Mercury-Earth angle, and α is the planet's angular diameter in radians. As this geometry and the distance to the planet changed nightly, figures that compare the tail are normalized for the same physical scaling via bilinear interpolation over both axes.

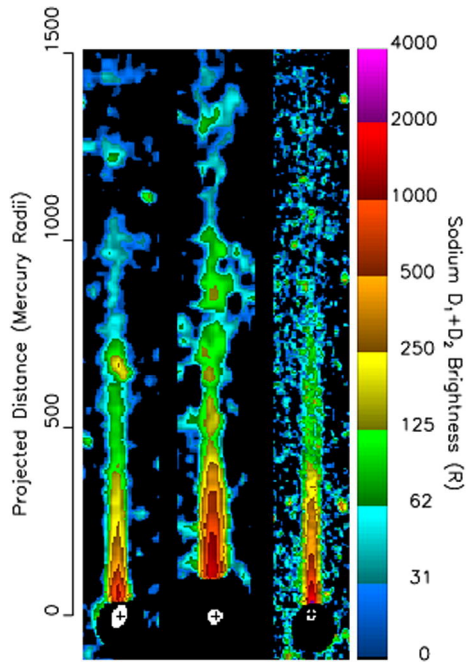


Figure 2.13 Observations spanning three elongations. (Left to right) UT 3 June 2007, 12 November 2007, and 18 May 2008.

Observing runs during 14-17 January 2008 and 3-6 July 2008 (Fig. 2.14) did not yield a detection of a tail beyond the occulting mask. In observations made just 7 hours after the MESSENGER first fly-by closest approach, no tail was found above the noise level at a distance of $\sim 120 R_M$, corresponding to the edge of the coronagraph mask. This finding is consistent with observations of the MASCS UVVS instrument onboard MESSENGER, which showed the tail disappearing from the detection limit

near $10 R_M$ (McClintock et al., 2008). Images from 15 January 2008 and 6 July 2008 represent non-detections and are shown in Fig. 2.14, in which background emissions largely correspond to high noise levels in the subtraction of terrestrial sodium due to low observing elevations.

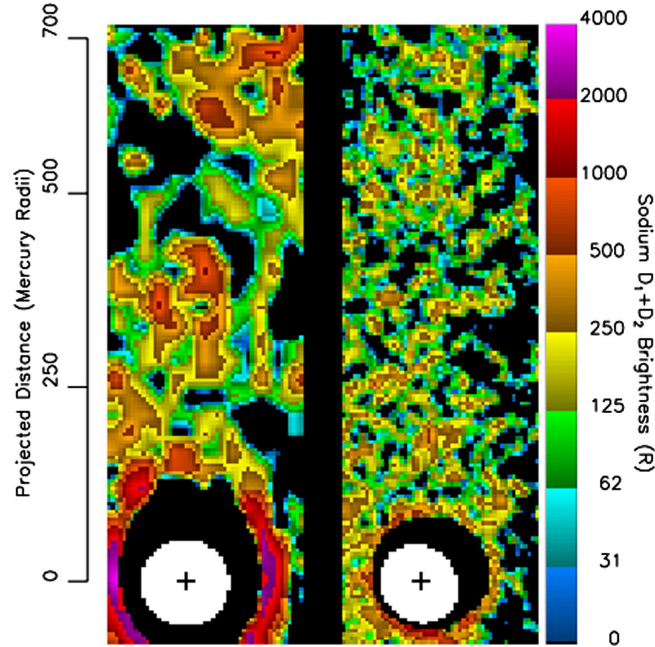


Figure 2.14 Example images from non-detections at (left to right) UT 15 January 2008 and 6 July 2008.

The effects of shadowing by the planet’s disk observed by UVVS in the two MESSENGER fly-bys (Vervack et al., 2009) are not seen in the coronagraph data set. Asymmetries and enhanced emissions in the northern portion of the tail measured by Potter & Killen (2008) at lesser distances are also not observed, a consequence of the instrument’s plate scale being far too large (~ 0.5 arcmin/pixel) to resolve the northern tail lobe from the southern one.

Fig. 2.15 shows the tail brightness versus distance profiles obtained from the data in Fig. 2.12 and Fig. 2.13. Each profile represents the emission in a single

row of pixels anti-sunward from Mercury after the images are rotated. The region out to a distance of $500 R_M$ is chosen to best highlight major differences. Poisson uncertainties in subtraction of terrestrial mesospheric sodium dominate the error in brightness. These are added in quadrature to a 10% uncertainty from standard star calibrations, producing the sample error bars shown every fifth data point.

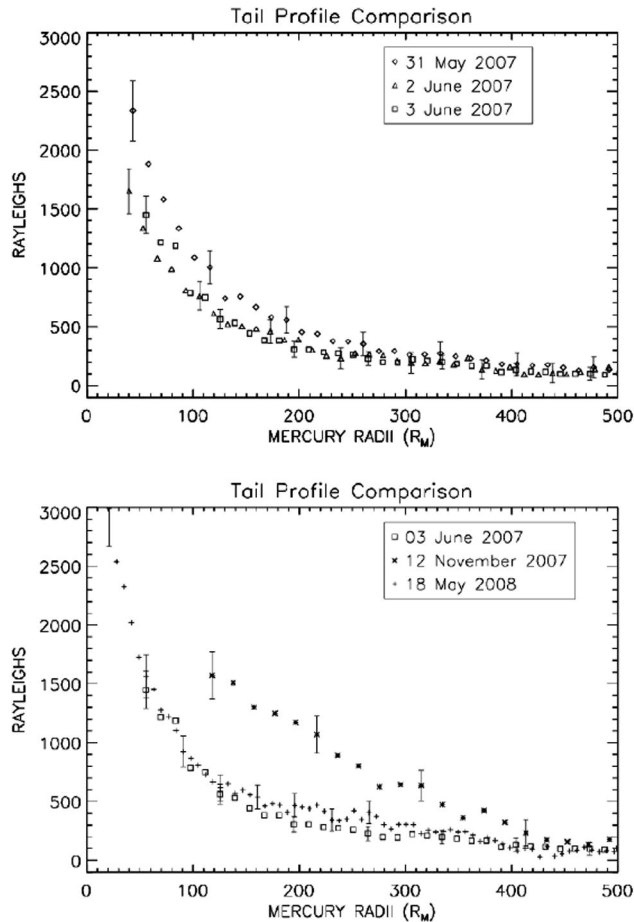


Figure 2.15 Comparison of peak brightness versus distance for each observation shown in Fig. 2.12 and Fig. 2.13.

Heliocentric velocity and radiation acceleration at Mercury are shown in Fig. 2.16 to demonstrate that the tail's long term variability was correlated with orbital motion. Colored regions indicate orbital data coverage over the the first five observing

runs. The black arrows represent the velocity feedback effect, by which radiation acceleration changes during an atom's transit down-tail, for a Doppler shift into or out of the Fraunhofer absorption well. The next chapter quantifies this effect in detail, and discusses the implications for atmospheric escape.

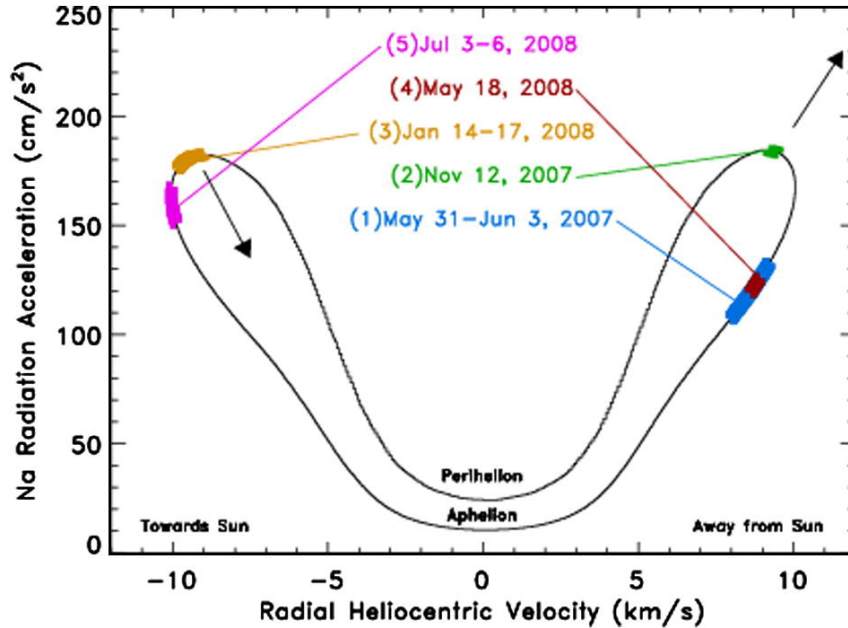


Figure 2.16 A diagram of radiation acceleration at Mercury's surface versus the heliocentric velocity intrinsic to Mercury orbit. The acceleration imparted to sodium atoms by solar photons will change by nearly a factor of 15 over Mercury's orbit, as shown by the vertical axis. As Mercury orbits, motion around this loop is clockwise. Atoms traveling down the tail experience an additional change in acceleration due to their Doppler shift with respect to the Sun; black arrows show the effect on atoms in the tail when Mercury is traveling toward and away from the Sun.

2.5.2 Variation in escape rates

The results in Fig. 2.15 suggest that the escape flux changes substantially with orbital position. In the lower panel that relates the long term results of Fig. 2.13, emission roughly doubled out to $500 R_M$ when the radiation acceleration increased from ~ 115 to $\sim 184 \text{ cm/s}^2$. The recorded emission does not scale directly with the

scattering rate (g-value) for these measurements, meaning amplified scattering alone cannot account for this emission enhancement. A doubling of emission shown in Fig. 2.15 must therefore represent higher column abundance in the tail. A change in the rate of escape in the surface-bound exospheric population is thus evident in these observations. Higher radiation pressure on 12 November 2007 stripped away more of the bound exosphere, so the increase in emission naturally results from Mercury's orbital phase, rather than transient variations in sources, e.g., ion sputtering or meteor impacts.

Some externally induced variability cannot be ruled out, however. Ion precipitation to Mercury's surface is dependent on the interplanetary magnetic field configuration (e.g., Massetti et al., 2003; Kallio & Janhunen, 2003) and effects of coronal mass ejections passing Mercury have been attributed to a factor of 3 increase in total exospheric sodium content (Potter et al., 1999). Since this observing campaign began in May 2007, the SOHO CELIAS instrument, positioned at Earth's L1 Lagrange point 1.5×10^6 km sunward of Earth, has recorded a range of daily proton energy densities changing by a factor of ~ 40 and momentum densities which change by a factor of ~ 30 . Unfortunately, extrapolations of this solar wind data from 1 AU back to Mercury are strongly model dependent, and constraints on the time variation of micro-meteors do not exist. However, SOHO MDI solar magnetograms and C3 coronagraph images show quiet Sun conditions for the 2007 - 2008 dates considered here. Although I find no evidence for the effects of solar activity in analyzing the first seven coronagraph observations, better constraints on solar wind and interplanetary magnetic field conditions at Mercury are needed in order to dismiss the possibility.

Data analysis of observations after my (Schmidt et al., 2010) study suggests that some day to day variability may be present, independent of that intrinsic to orbital effects. Fig. 2.17 shows observations that straddle the orbital phase of maximum

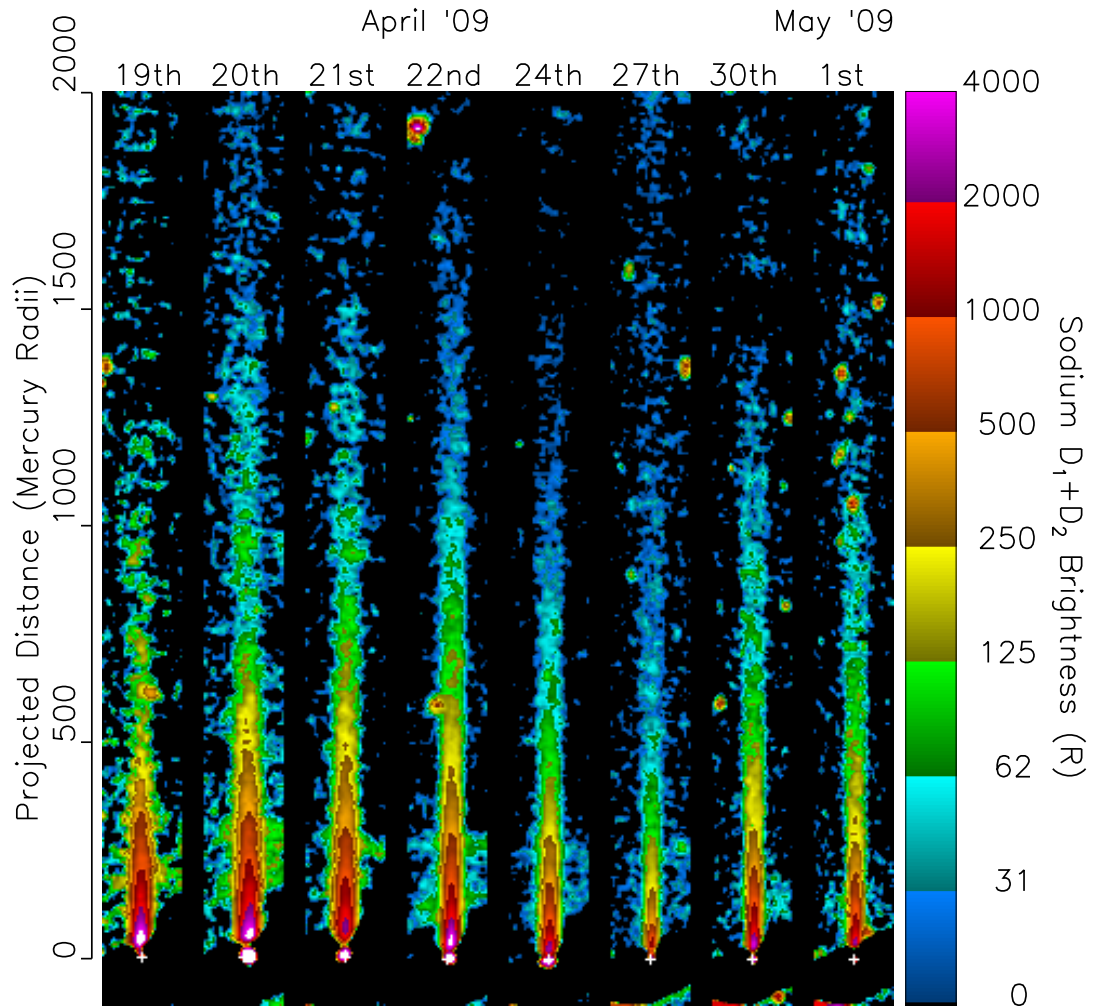


Figure 2.17 Observations of the sodium tail during campaign 6 in April of 2009. Radiation pressure is at a maximum on 22 April 2009.

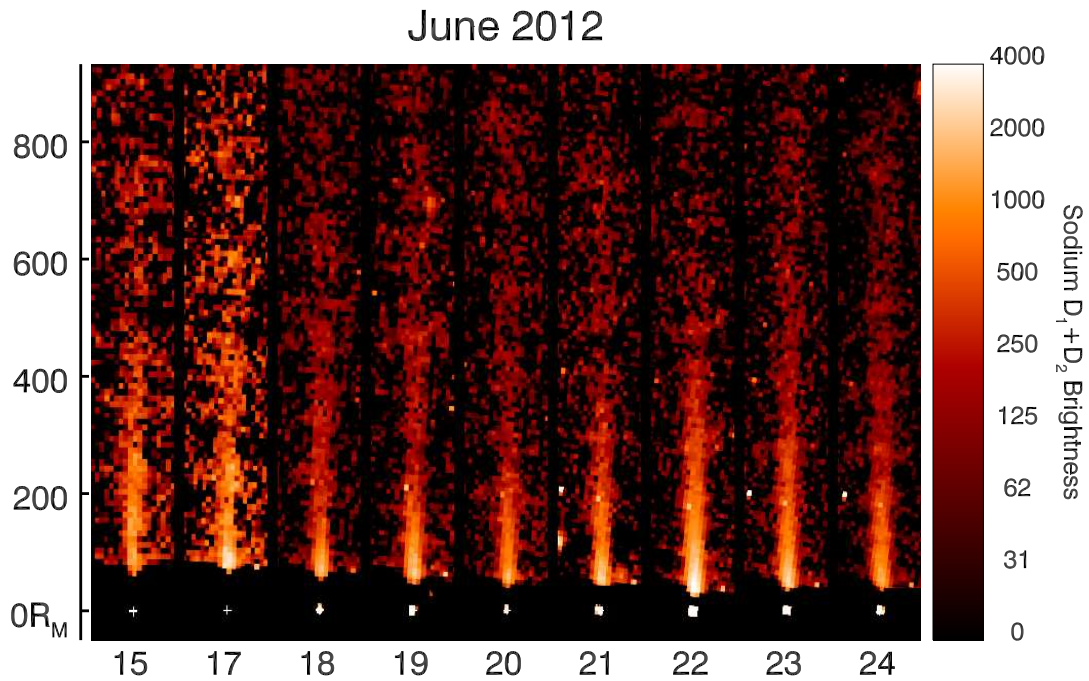


Figure 2.18 A survey of the sodium tail during observing campaign 12, in June 2012. Radiation pressure is decreasing from left to right. The signal to noise level improves on consecutive nights, with Mercury’s elevation at dusk.

radiation pressure on 22 April 2009. Brightness of the tail appears to either surge during the final two nights of the campaign or show a depletion on April 24th and 27th. Fig. 2.18 shows an output of the coronagraph’s data reduction pipeline for the June 2012 observing campaign. As given in Table 2.1, the radiation pressure was steadily decreasing over these dates. Yet, the brightness in the tail was not observed to steadily decrease over consecutive nights. Significant escape occurs even for a radiation acceleration of only 106 cm s^{-2} on 24 June 2012. Prior studies have predicted that the tail should not be observable at this time (Potter & Killen, 2008). The preliminary results in figures 2.17 and 2.18 suggest short-term changes in drivers in Mercury’s

escape. However, further analysis of these data and a more careful review of the calibration is needed to confirm or refute the presence of day to day variability.

2.5.3 Image Slicing Spectrograph: Near Planet Tail

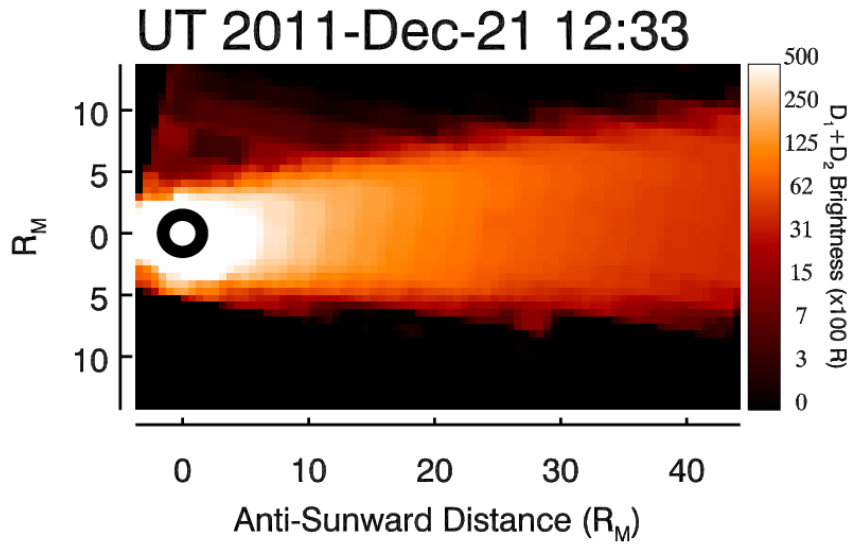


Figure 2.19 The composite of several images taken on 26 Dec 2011 when Mercury reaches its maximum velocity from the sun at a true anomaly angle of 90°

Figure 2.19 shows an image of the tail at a true anomaly angle of 90° when Mercury was at the maximum heliocentric velocity. This figure currently represents the highest resolution ground-based image of Mercury's escaping sodium exosphere. Values within $1 R_M$ of the disk are masked as surface reflection and seeing artifacts in this region yield poor confidence. A slight enhancement in emission in the northern lobe of the tail is seen relative to the south. Although contamination of scattered light from Mercury's disk has been removed from adjacent rows of pixels (cf. Sec. 2.4.1), further analysis of scattered light artifacts is warranted before the North-South asymmetry can be quantified precisely. Still, an overall north-south ratio greater than

unity can be claimed with confidence. A physical mechanism responsible for this asymmetry is proposed in Sec. 5.3 and modeled in detail in Sec. 5.3.1

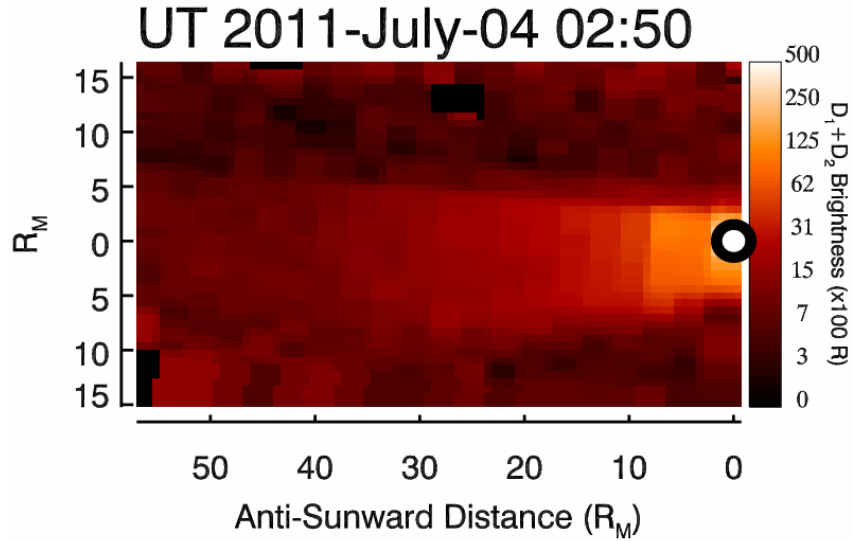


Figure 2.20 The composite of several dithered and individually calibrated images taken the on night of 4 July 2011

Figures 2.20 and 2.21 show final nightly composite images taken two Mercury years apart, but at the same orbital longitude. As each was taken during an opposite elongation (morning / evening), the tail’s direction is flipped between images. In contrast to the coronagraph, noise levels in the image-slicer data are primarily governed by scattered light from Mercury’s disk and by the Doppler separation from terrestrial emissions. The relative velocity of -26.4 km s^{-1} in Fig. 2.20 produces noticeably more noise than in Fig. 2.21, where a 35.5 km s^{-1} shift fully separates the terrestrial and hermean lines. Considering seeing effects and subtraction of bright surface reflection, comparisons in brightness very close to the planet’s disk are dubious (values within $1 R_M$ of the disk are masked completely for this reason). However, the sodium tail beyond $\sim 10 R_M$ agrees very closely, both in brightness and width between these im-

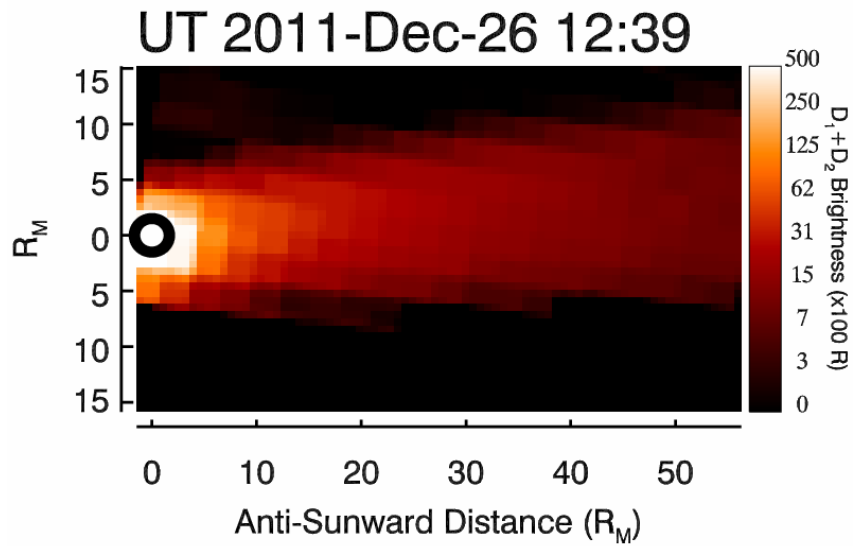


Figure 2.21 The composite of several images taken 26 Dec 2011 at the same orbital phase as 2.20

ages. Like the coronagraph results in Fig. 2.13, which are separated by four Mercury years, the characteristics of sodium escape are seen to persist over repeated measurements taken at similar orbital longitudes. Although only the high energy component of the exosphere is seen in these data, this finding indicates an atmosphere governed by seasonal effects, rather than driven by variability from Mercury's dynamic space environment.

Chapter 3

The Interpretation of the Data and Simulating Na Exospheres

3.1 Introduction

This chapter describes the physical processes associated with sodium D-line emission at Mercury. The unique effects imparted by solar radiation pressure and Mercury's eccentric orbit are derived. A simple 1-dimensional model is presented of the Na D-line emission as a function distance down the escaping tail. Fits of this model to the first two years of coronagraph data yield the highest Na escape rates reported at Mercury (Schmidt et al., 2010).

3.2 Sodium Spectroscopy

Extracting density information from the data sets in this study requires an understanding of the physical process that scattered the photons. Therefore, a review and physical description of the sodium atom is outlined here with a focus on its energy states and the D-line transitions.

Sodium has but 1 stable isotope, ^{23}Na , comprised of 11 proton electron pairs, and 12 neutrons. The ground state term symbol is $^2S_{1/2}$ and the electron configuration is $1s^22s^22p^63s$. A term symbol uniquely identifies quantized levels according to the format $^{2S+1}L_J$, where S is the total spin angular momentum quantum number, given sum of the $\pm 1/2$ spins of the valence electrons, and $J = L \pm S$, for an orbital angular

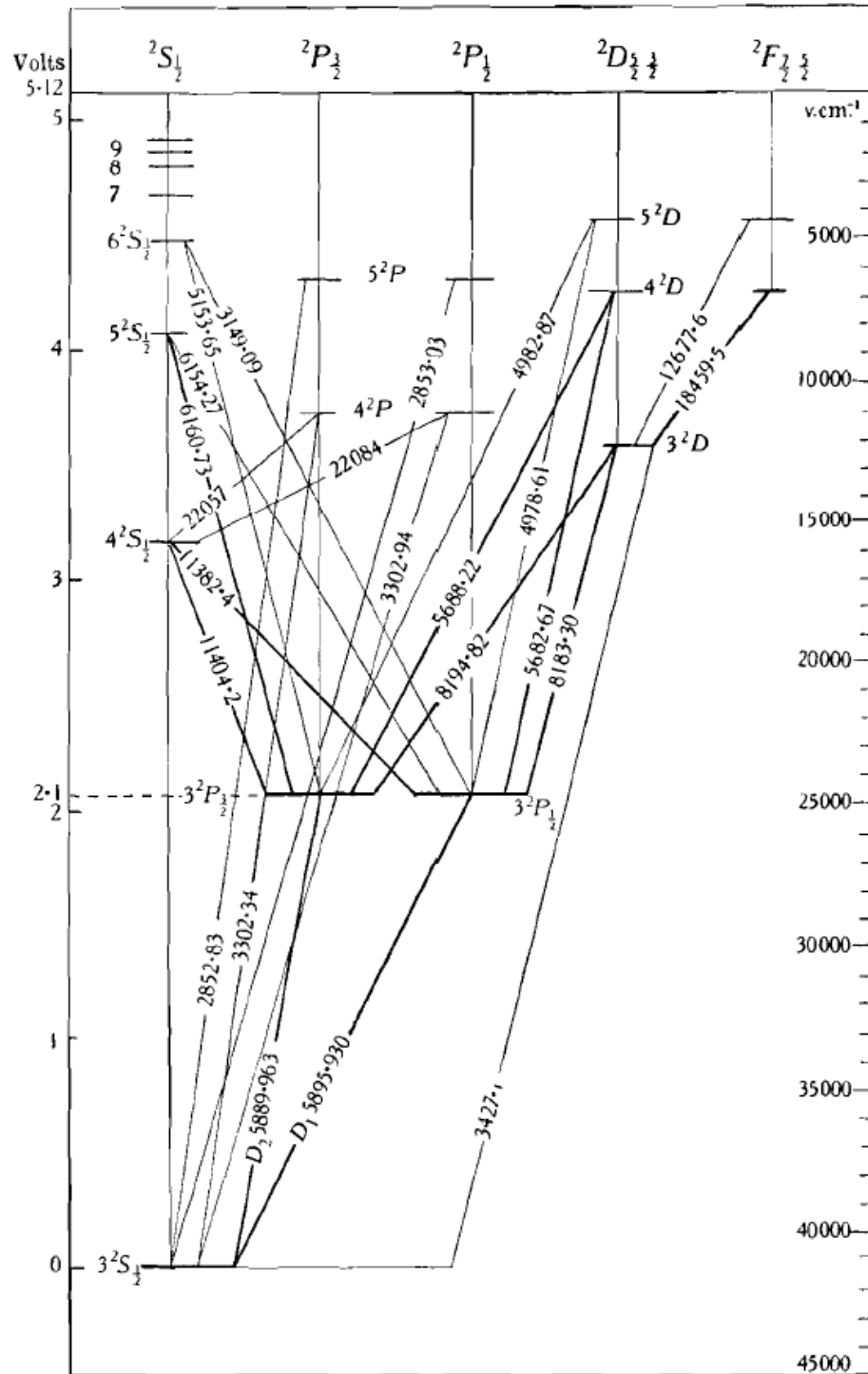


Figure 3.1 Grotrian diagram of transitions within a sodium atom. Transitions from first excited states, $2P_{1/2}$ and $2P_{3/2}$, to the $2S_{1/2}$ ground state result in the D-line emission doublet. Adapted from Mitchell & Zemansky (1934)

momentum quantum number L . Although there are many electric quadrupole and magnetic dipole transitions in sodium, electric dipole transitions are the most efficient in naturally occurring Na gas and result in the D-line doublet at 5890 Å and 5896 Å. The electric dipole transition selection rules for the change in quantum numbers are: $\Delta S = 0$, $\Delta m_s = 0$, $\Delta L = \pm 1$ and $\Delta m_l = 0, \pm 1$. Figure 3.1 shows an energy level diagram indicating transitions within a sodium atom.

The anomalous Zeeman effect, that is, splitting of an energy state in the absence of an external magnetic field, was first observed in sodium D-lines, earning Pieter Zeeman the 1902 Nobel Prize in Physics. It is termed anomalous as this was well before quantum theory determined that the electron had its own spin generating a B field native to the atom. The magnetic field strength in Mercury's exosphere is $\sim 10^{-7}$ of that intrinsic to the atom, so that further splitting need not be considered here. The quantum number which determines Zeeman splitting is $m_j = m_l + m_s$ which has allowed values of $\pm J$. Considering this effect semi-classically, both the electron spin and the current from its orbital motion induce a magnetic moment. Because the electron spin (quantum number s) and the electron's angular momentum (quantum number l) are both quantized, the interaction of their induced magnetic moments in the spin-orbit coupled state is also quantized, hence m_j . Electric dipole transitions require that $\Delta S = 0$, so spin drops out of the transition selection rules and $m_j = m_l + m_s = m_l = 0, \pm 1$. Thus, sodium has four degenerate states at the ${}^2P_{3/2}$ level and only two degenerate states at the ${}^2P_{1/2}$ level ($l = 1, s = 1/2, J = l - s = 1/2$). Fig 3.2 gives oscillator strengths for these transitions as well as the Zeeman line shifts from the centroid (Morton, 2003). Note, that these quantities differ slightly from those quoted in Brown & Yung (1976).

		${}^2P_{1/2}$	
		$m_j = -1/2$	$m_j = +1/2$
${}^2S_{1/2}$	$m_j = -1/2$	$f = .026$ $\Delta\lambda_z = -11.4m\text{\AA}$	$f = .133$ $\Delta\lambda_z = -13.6m\text{\AA}$
	$m_j = +1/2$	$f = .080$ $\Delta\lambda_z = 9.1m\text{\AA}$	$f = .080$ $\Delta\lambda_z = 6.9m\text{\AA}$

		${}^2P_{3/2}$			
		$m_j = -3/2$	$m_j = -1/2$	$m_j = +1/2$	$m_j = +3/2$
${}^2S_{1/2}$	$m_j = -1/2$	$f = .053$ $\Delta\lambda_z = -12.1m\text{\AA}$	$f = .133$ $\Delta\lambda_z = -12.3m\text{\AA}$	$f = .133$ $\Delta\lambda_z = -12.7m\text{\AA}$	Forbidden ($\Delta m_j = 2$)
	$m_j = +1/2$	Forbidden ($\Delta m_j = 2$)	$f = .016$ $\Delta\lambda_z = 8.2m\text{\AA}$	$f = .080$ $\Delta\lambda_z = 7.8m\text{\AA}$	$f = .225$ $\Delta\lambda_z = 7.2m\text{\AA}$

Figure 3.2 Oscillator strengths and line shifts ($\Delta\lambda_z$) for anomalous Zeeman splitting in sodium. The vacuum line centroids are taken as 5891.5833\AA for D2 and as 5897.5581\AA for D1. The total oscillator strength of allowed D2 transitions are twice those of D1.

3.3 Radiative Transfer: Resonant Scattering

The lifetime for spontaneous emission of Na in both the ${}^2P_{3/2}$ and the ${}^2P_{1/2}$ states is $\sim 1.6 \times 10^{-8}$ s (Sansonetti, 2008). When this nearly instantaneous de-excitation follows the absorption of a photon, the process is termed resonant scattering. Where illuminated, collisional de-excitation of atomic Na in the 2P state is effectively negligible given the relative timescales. Even in Earth's mesosphere, where sodium is deposited in molecular form, collisional effects on the D-line features are minimal compared with resonant scattering. Free sodium produced by collisions with oxygen yield < 100 R nightglow brightness, whereas resonant scattering at twilight is several kilo-Rayleighs at zenith (Chamberlain, 1961). When compared with Earth's mesosphere, collisional effects and atmospheric chemistry in Mercury's exosphere are negligible. Excitation by UV photo-dissociation of Na in molecules may still be present, but the emission is negligible given the remarkable efficiency at which sodium continuously scatters visible solar photons and the high atomic to molecular Na abundance. Thus,

all D-line emission in Mercury's exosphere can be considered as resonant scattering of solar photons to an excellent approximation.

In applications at Mercury, a derivation of the resonant scattering rate is straightforward. Consider a beam of light of intensity $I_\nu(0)$, passing through a layer of sodium gas of thickness s which absorbs, but has negligible emission. In the absence of a source function, the solution of the transfer equation for pure absorption of the emergent beam, $I_\nu(s)$, is:

$$I_\nu = I_\nu(0) \exp\left(-\int_0^s k_\nu(s) ds\right) \quad (3.1)$$

The absorption rate can be expressed in terms of the Einstein B coefficients by treating stimulated emission as negative absorption. Using u and l to designate the upper and lower energy states, the absorption coefficient per unit of volume, k is formulated as:

$$\begin{aligned} k_\nu &= \frac{\text{energy}}{\text{solid angle}} \times \frac{\text{atoms}}{\text{volume}} \times \frac{\text{absorptions}}{\text{atom s}} \times \text{absorption line profile} \\ &= \frac{h\nu_0}{4\pi} (n_l B_{lu} - n_u B_{ul}) \phi(\nu) \\ &= \frac{h\nu_0 n_l B_{lu}}{4\pi} \left(1 - \frac{g_l n_u}{g_u n_l}\right) \phi(\nu) \\ &\approx n \frac{h\nu_0 B_{lu} \phi(\nu)}{4\pi} = n \frac{\pi e^2 f_{lu} \phi(\nu)}{m_e c} \end{aligned} \quad (3.2)$$

where n is the number density of sodium, g is the state degeneracy, $h\nu_0$ is the energy at line center, B_{lu} is the Einstein coefficient for photo-absorption and $\phi(\nu)$ is the line profile. The last result is also expressed in terms of the transition's unitless oscillator strength, f , where e and m_e are the charge and mass of the electron, respectively, and c is the speed of light. The final step in Eq. 3.2 is well approximated in the limit that all the gas is in the ground state. This section will demonstrate that the timescale between scatterings is several orders of magnitude longer than the spontaneous emission

lifetime, so that a negligible fraction of the atoms are radiatively excited at any given instant. For collisional excitations, the ratio of atomic energy states in thermodynamic equilibrium (Boltzmann factor) is plotted with temperature in Fig 3.3, demonstrating that this limit applies for collisional gases $<4000\text{K}$. The assumption that all sodium in the hermean exosphere is in the ground state is hence justified.

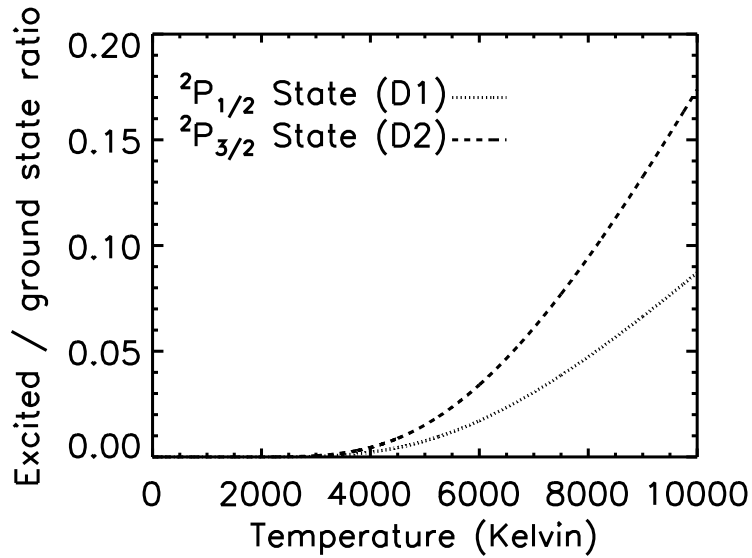


Figure 3.3 Ratio of sodium occupying the 2P states to ground states. Statistical weights of the degenerate energy states cause the $^2P_{3/2}$ level to populate at twice the $^2P_{1/2}$ abundance.

Each ground state atom is able to absorb photons over a range of frequencies such that $\phi(\nu)$ is a Lorentzian line profile. The absorption line profile from a collection of atoms must take into account the Doppler velocity distribution. If in thermal equilibrium, the atomic velocity distribution along the any axis (in this case the Mercury-Sun axis) is given by:

$$f(v_r) dv_r = \sqrt{\frac{m}{2\pi kT}} \exp\left(\frac{-mv_r^2}{2kT}\right) \quad (3.3)$$

where k is Boltzmann's constant, m is the atomic mass, and T has units of Kelvin. Setting Eq. 3.3 equal to one half the maximum, and substituting $\Delta\nu = \frac{\nu_0 v_r}{c}$, it's immediately clear that the FWHM of the Doppler broadened profile, $\Delta\nu_D$, is

$$\Delta\nu_D = 2\sqrt{Ln2}\sqrt{\frac{2kT}{m}}\frac{\nu_0}{c} \quad (3.4)$$

The corresponding distribution of Eq. 3.3 over frequencies is determined by substituting $\nu = \nu_0 \left(1 + \frac{v}{c}\right)$:

$$\begin{aligned} \phi(\nu)d\nu &= f(v_r)\frac{dv_r}{d\nu}d\nu \\ &= \frac{c}{\nu_0}f_v\left(c\left(\frac{\nu}{\nu_0} - 1\right)\right)d\nu \\ &= \sqrt{\frac{mc^2}{2\pi kT\nu_0^2}}\exp\left(-\frac{mc^2(\nu - \nu_0)^2}{2kT\nu_0^2}\right)d\nu \end{aligned} \quad (3.5)$$

Near line center, the Doppler profile dominates over the natural Lorentzian absorption profile. Inserting Eq. 3.5 and 3.4 into Eq. 3.2, the absorption coefficient becomes:

$$k_\nu = n\frac{\pi e^2 f_{lu}\phi(\nu)}{m_e c} = n\left(\frac{\pi e^2 f_{lu}}{m_e c}\right)\frac{2\sqrt{Ln2}}{\sqrt{\pi}\Delta\nu_D}\exp\left(-Ln2\left(\frac{2(\nu - \nu_0)}{\Delta\nu_D}\right)^2\right) \quad (3.6)$$

By setting $\int_0^s k_\nu(s) ds = 1$, the optical depth at line center reaches unity at a column density of:

$$\begin{aligned} N &= \frac{m_e c \Delta\nu_D}{2\sqrt{\pi Ln2} e^2 f_{lu}} \\ &= 6.6 \times 10^{11} \text{ atoms cm}^{-2} \text{ for D1 at 5000 K} \\ &= 3.3 \times 10^{11} \text{ atoms cm}^{-2} \text{ for D2 at 5000 K} \end{aligned} \quad (3.7)$$

Na column density estimates on Mercury have been quoted as high as $\sim 8 \times 10^{11}$ atoms/cm² locally (Sprague et al., 1997). The D2 disk-averaged intensity at Mercury

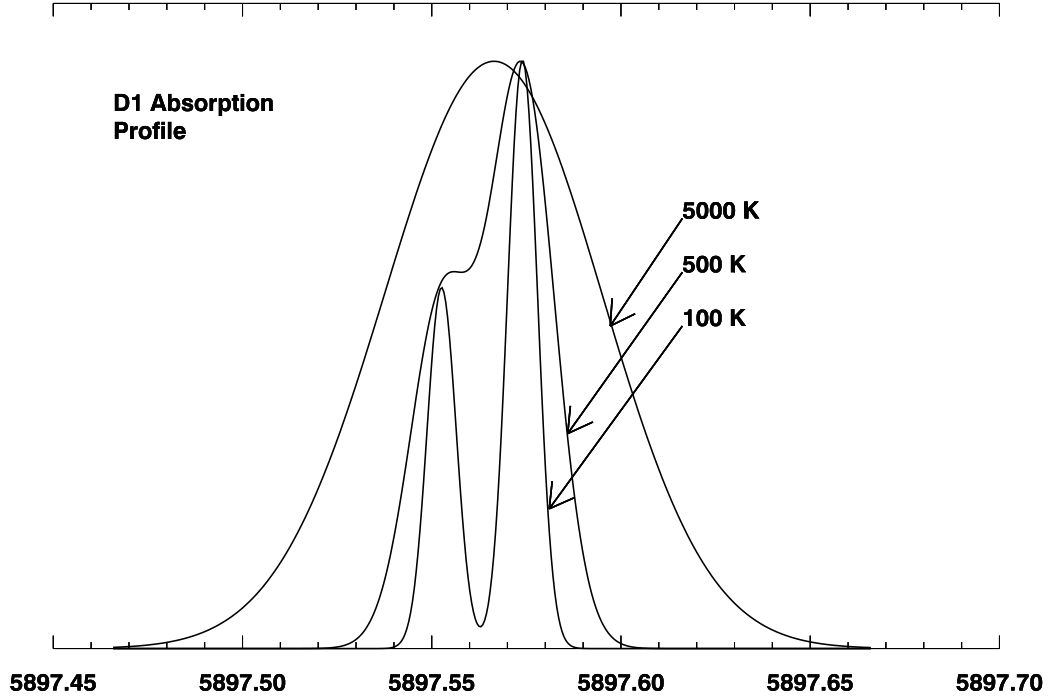


Figure 3.4 The volumetric absorption coefficient for the D1 line as a function of the incident photon wavelength, shown for thermalized gas at several temperatures. Note that observed wavelengths are shifted by -1.65 \AA from the vacuum wavelength given here due to refraction in air.

typically varies between 1 and 6 MR (Leblanc & Johnson, 2010). For the scattering rate characteristic to orbital phases with an escaping sodium tail, the D2 emission from a $3.3 \times 10^{11} \text{ atom cm}^{-2}$ column would be ~ 10 MR. Thus, if the brightness exceeds ~ 10 MR locally in regions over the planet's surface, a full treatment necessitates radiative transfer calculations involving multiple scattering, surface reflection, and phase angle corrections (e.g., Killen, 2006). Such opacity effects are not presently included as the coronagraph and image slicer are not sensitive to exospheric emissions

directly over the disc. Where necessary, near-disc model results in my work are given in column density rather than brightness.

Sodium in Mercury's exosphere does not inherently possess a Maxwell-Boltzmann velocity distribution. If thermodynamic equilibrium does not hold, the distribution of atomic velocities is no longer governed by Eq. 3.3 and the absorption characteristics follow accordingly. In any case, the thermal limit is amenable to modification and useful for comparison with non-Maxwellian populations. Fig. 3.4 shows k_ν (Eq. 3.6) as a function of temperature for the D1 line, taking into consideration the hyperfine structure in Fig. 3.2.

The brightness observed in this work is directly proportional to the equivalent width of the absorption line, which is a function of both the column density and the velocity distribution of the gas. Using Eq. 3.1, the equivalent width of the absorption lines, W , is determined as:

$$W = \int_{-\infty}^{\infty} \left(1 - \frac{I_\lambda}{I_\lambda(0)} \right) d\lambda = \int_{-\infty}^{\infty} (1 - e^{-\tau_\lambda}) d\lambda \quad (3.8)$$

In the optically thin limit, the broadened profile in Eq. 3.6 is normalized so that the integral over frequency is unity. In this case, corresponding to the constant sloped portion of Fig. 3.5, the total absorption for a given line is simply a linear function of the column density. The resonance scattering rate of the i th emission line, g_i , has units of photons $\text{atom}^{-1} \text{s}^{-1}$, and is simply the product of the absorption cross-section and the solar flux (Chamberlain, 1961).

$$g_i = \frac{F_\odot \lambda \pi e^2 f_i}{R^2 \nu m_e c} \quad (3.9)$$

where F_\odot is the differential solar flux in photons $\text{cm}^{-2} \text{s}^{-1} \text{\AA}^{-1}$, R is the atomic heliocentric distance in AU, and λ/ν converts between frequency and wavelength units. The time between any photon scatterings is the sum, $\sum_i g_i^{-1}$, and can be as short

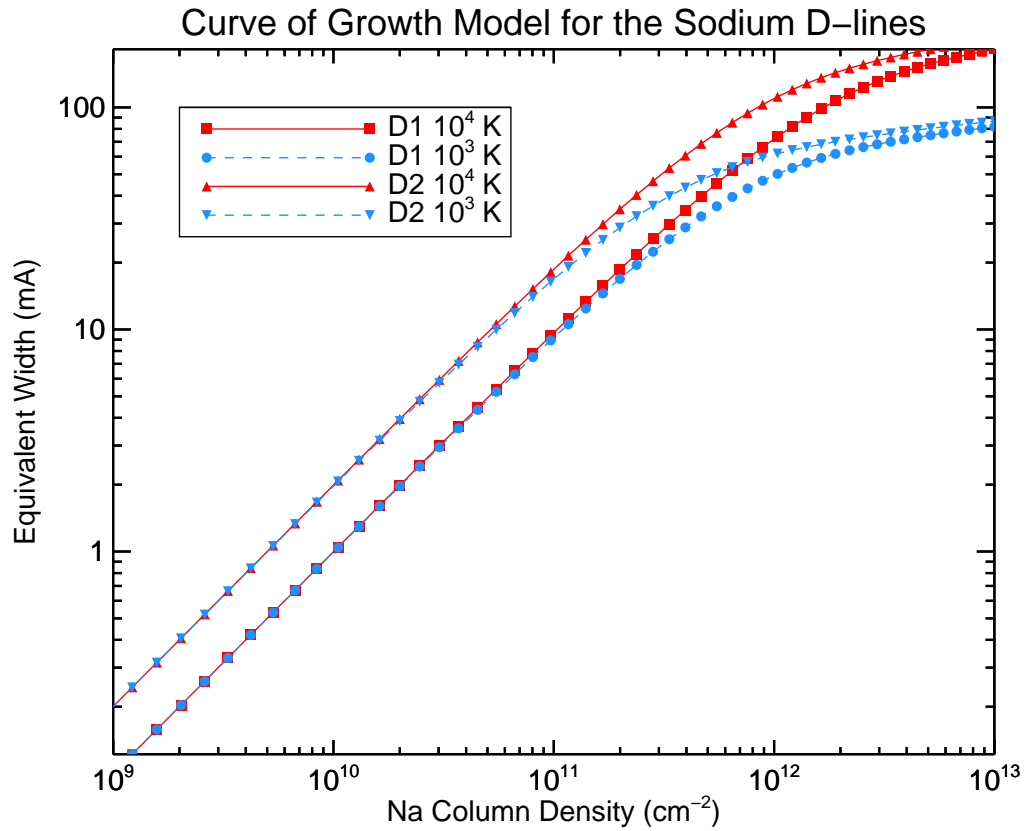


Figure 3.5 Theoretical curve of growth for absorption of the sodium D-line doublet.

as 10^{-2} s, depending on Mercury's orbital phase. In the absence of non-radiative de-excitation or multiple scatterings, a column density, N , in atoms cm^{-2} , is calculated from the from observed surface brightness, I , in Rayleighs, as simply $N = 10^6 I/g$. As seen in figures 3.3 and 3.5, this simple relation between brightness and column density applies in the limit that the abundance is $\lesssim 10^{11}$ atoms cm^{-2} , and either cold ($\lesssim 4000\text{K}$) or collisionless.

3.4 Radiative Transfer: Radiation Pressure

Radiation pressure results from a net momentum transfer at each photon scattering. Each photon absorbed by a sodium atom carries momentum h/λ or E/c . If z is the anti-sunward vector, and θ_i and θ_r are the angles between z and the incident and reflected directions, respectively, the change in the z component of momentum from photons of wavelength λ is:

$$dp_\lambda = \frac{h}{\lambda} \cos(\theta_r) - \left(-\frac{h}{\lambda} \cos(\theta_i) \right) \quad (3.10)$$

Since the sodium doublet scatters symmetrically about z , the cosine θ_r term vanishes when the average of many scatters is considered, that is, over several seconds. The average θ_i angle is zero by definition, and thus the momentum of each photon is transferred completely to the atom. With the scattering rate per atom given by Eq. 3.9, the g -value, the force applied to a sodium atom by radiation is simply the photon's momentum times the frequency of scatters:

$$F_{Rad} = \frac{dp_\lambda}{dt} = \sum_i \frac{h}{\lambda_i} g_i = m a_{Rad} \quad (3.11)$$

where the sum is over all resonantly scattered lines. In practice, only the D-line doublet need be considered in this sum, as its transition strength is ~ 3 orders of magnitude higher than all other ground state transitions in the visible band combined (cf. NIST Atomic Spectra Database).

Considerable Doppler shifting relative to the solar Fraunhofer spectrum is inherent to Mercury's high orbital velocity and eccentricity, so that resonant scattering rates for sodium D line emission vary by more than an order of magnitude during the hermean year. Since Mercury has a large eccentricity of 0.21, its heliocentric velocity varies substantially with orbital position: ± 10.06 km/s radial velocities occur at true

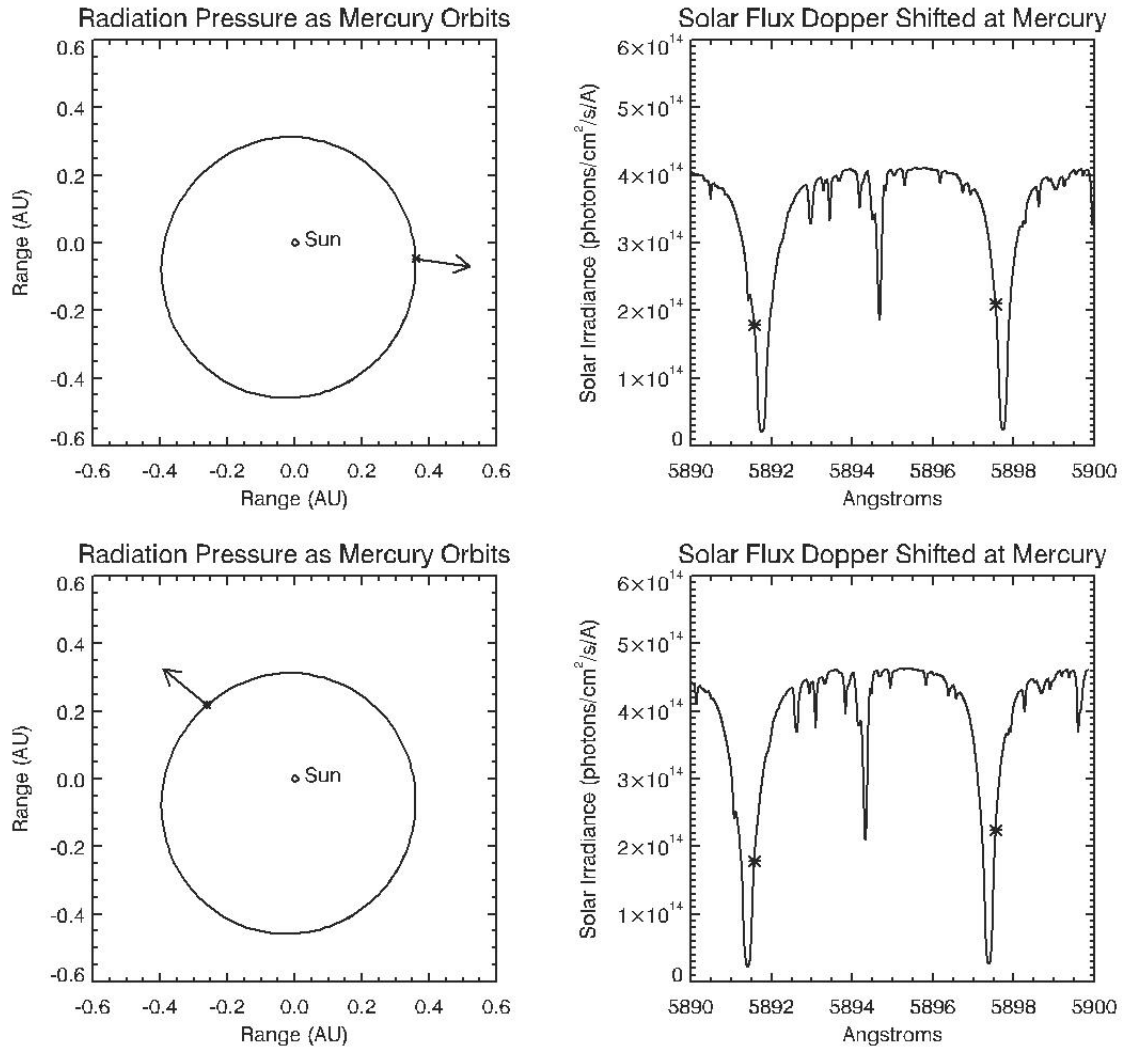


Figure 3.6 Doppler shifts in solar spectrum cause large variations in the incident flux that an Na atom can scatter. The top panel is an example during Mercury's inbound orbital leg while the bottom panel is during outbound orbital motion. Frames at left show Mercury's orbit to scale, indicating the direction of the resulting radiation pressure. The frames at right give the solar spectral irradiance, and the asterisks indicate the amount incident on a Na atom in Mercury's rest frame. The acceleration by solar radiation varies by more than an order of magnitude at Mercury because of its eccentric orbit and Doppler shifting about the narrow solar Fraunhofer absorption wells.

anomaly angles of $\pm 90^\circ$. The panels in Fig 3.6 show examples of the incident solar flux when Mercury is traveling toward the sun in the inbound portion of its orbit (top panel), and away from the sun on its outbound orbital leg (bottom panel). The asterisks denote the resonantly scattered flux at Mercury's surface. Further Doppler shifting occurs as escaping atoms are accelerated down the tail, and the scattered flux in the atom's frame move to the right of the asterisks in Fig 3.6. When Mercury's velocity is Sun-ward, sodium atoms accelerating down the tail will Doppler shift into the solar Fraunhofer absorption wells, where they encounter less sunlight and experience less acceleration. The opposite effect occurs when Mercury is moving away from the Sun: atoms accelerating down the tail interact with greater amounts of sunlight as they go, and experience increasing acceleration. In addition to the Doppler shift effect from Mercury's orbital motion denoted by the asterisks, Na atoms moving down the tail experience strong forces imparted by radiation pressure with this velocity feedback effect. As the velocity increases, the solar flux at the absorption wavelengths increases, resulting in further acceleration—a positive feedback loop. After just a few hours, such atoms Doppler shift out of the D-line absorption wells entirely and experience a more constant acceleration from the solar continuum. This dramatic effect at Mercury is unique among planets in our solar system; only comets are known to experience such a strong positive feedback in radiation pressure. In the case of Hale-Bopp, for instance, the neutral Na exosphere is pushed out to at least 8 million km (Wilson et al., 1998).

Changes in incident flux at the D1 and D2 rest wavelengths due to Doppler shifting affect the Na distribution via three physical processes. First, radiation acceleration determines the number of atoms which are capable of being pushed beyond the escape velocity to overcome surface gravity, thereby controlling the fraction of the source population lost to the tail. Second, radiation acceleration governs how far the atoms travel down the tail before being photo-ionized, setting the neutral tail's

length ($\tau_i = 4.4\text{-}10.2$ h, depending on the orbital distance from the Sun). Third, since scattered sunlight is being observed, the solar flux available for scattering affects the tail brightness. Determining the column density at any point down the tail requires knowledge of the mean heliocentric velocity at that point. Radiation acceleration at Mercury's surface changes by nearly a factor of twenty over an orbit, so the escape rate may vary considerably irrespective of the ejection rate from the regolith.

Radiation pressure plays a key role in overcoming gravity and shaping the exospheric coma into a tail. Atoms escaping the planet's gravity down the tail represent the highest-energy component of the sodium exosphere. Although few atoms are more energetic than the 4.25 km/s escape velocity, bound orbits can be achieved at speeds of 3 km/s. These atoms can be easily destabilized into escape trajectories by solar radiation pressure. Modeling of radiation pressure by Ip (1986), Smyth (1986) and Smyth & Marconi (1995) has shown that atoms with a surface ejection velocity of at least 2 km s⁻¹ can acquire the additional velocity needed to reach the 4.25 km/s escape speed, and thus begin their journey down the tail. In particular, during a portion of the orbit marked by strong radiation pressure spanning 50° to 120° in true anomaly, the escape of sodium in Mercury's atmosphere grows to a significant fraction of its total surface production rate. An extensive ground-based study, summarized in Leblanc & Johnson (2010) and Potter et al. (2007), has measured a depletion by as much as 50% from the expected D2 brightness for a steady source at these phases. This reduction in disc-averaged brightness could be attributed, at least in part, to radiation pressure forcing the escape of the sodium atmosphere from the planet.

3.5 1-Dimensional Approximations in Wide Field Data Analysis

In modeling the coronagraph data, the down-tail brightness with distance and the cross-tail expansion of the coma can be well approximated with an analytical solution. In this approach, the cross-tail brightness in the coronagraph data is integrated leaving a one dimensional down-tail profile allowing an escape flux to be fit uniquely. The falloff in emission down the tail is due to photo-ionization, but also due to the spreading between atoms that results from acceleration, making the gas more diffuse with distance. The essential elements to this approach include a high resolution solar spectrum, the viewing geometry, the absorption coefficient, the heliocentric range and velocity and the photo-ionization lifetime.

3.5.1 Down-tail Velocity Estimation

To interpret the results shown in Fig. 2.12 - 2.15, within the context of Fig. 2.16, a first order estimate must be made of the velocities of sodium gas at various distances in the observed tails. This simple approximation starts with Na atoms which have escaped Mercury's gravity, rather than modeling a velocity distribution in the gravitational field. Naturally, a distribution of energies and initial ejection trajectories are present in the exosphere, however, the essential features of tail formation physics appear with a low (even zero) initial speed away from Mercury, i.e., atoms that have just enough energy to escape the planet. Using 1-min time steps, radiation acceleration is calculated via scattering rates in the same method described in Sections 3.3 and 3.4. The corresponding displacement and velocity over a time step are found and applied. A new solar flux is then assigned based on the calculated Doppler heliocentric velocity with a high resolution solar spectrum (Bass2000 solar survey available at <http://bass2000.obspm.fr>) and forwarded to the next time step. In this way, a

heliocentric velocity is calculated and then interpolated to each pixel down the tail. An example of these calculations is shown in Fig. 3.7 for the case of 18 May 2008.

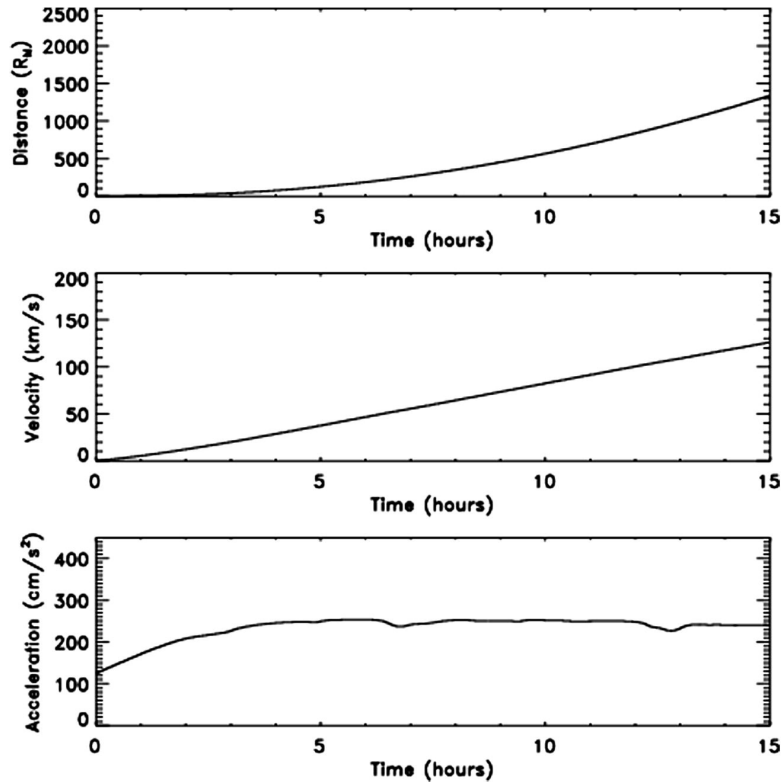


Figure 3.7 For the 18 May 2008 observing date, a calculation of distance from surface, velocity and acceleration with time, that a sodium atom may experience after escaping Mercury's gravity. Small changes seen in the acceleration curve correspond to Fraunhofer absorption features in the solar spectrum.

Whereas gravity is clearly the dominant force near the surface, within only ~ 0.3 to $\sim 4.5 R_M$, depending on orbital position, radiation acceleration overtakes gravitational acceleration, so that it can be considered negligible at the large distances considered here. Down-tail velocities due to radiation pressure can exceed 100 km s^{-1} at distances of several hundred R_M . Omitting the effects of shadowing and Mercury's gravity in this calculation of heliocentric velocity arguably ignores processes that effect particle trajectories near Mercury. However, the vast number of Na atoms captured

in the coronagraph data are beyond the domain of such effects. Since both shadowing and gravity effectively slow the transport of atoms down-tail at early times, these velocity calculations place an upper limit on the Doppler shift.

3.5.2 Transverse velocity

The sodium population in the tail expands as it moves downstream in the direction perpendicular to the Sun. This motion is essentially the random speed of typical ejection processes after the atoms have slowed in the gravitational escape. To calculate the velocity of this expansion, I have fit a Gaussian to the cross-section down the tail (while the shape of the cross-tail profile is not implicitly Gaussian, this assumption provides a convenient first order solution as desired). The point spread function taken from neighboring stars in the field is subtracted in quadrature from the FWHM of these fits, in order to estimate the true tail width. The mean transverse velocity is computed from half the change in FWHM with time. Time elapsed for sodium to reach each position down-tail is derived considering radiative forces as discussed in the preceding section 3.5.1. The expanding FWHM with down-tail distance is shown in Fig. 3.8 for the data taken 18 May 2008. I estimate an average transverse velocity of 1.2 ± 0.1 km/s was present at this time, shown as the solid line in Fig. 3.8.

Table 3.1 gives the tail's FWHM at several points downstream, and the associated transverse component of the velocity, V_{\perp} . The average and standard deviations of all measurements at each distance are given in the last row. Velocity is estimated by fitting the FWHM out to a distance of $400 R_M$ where Gaussian fits are most dependable. Uncertainties represent the standard deviations in the coronagraph point spread function and the FWHM of neighboring points. Variability in the expansion rate with orbital phase is within one standard deviation of the average and shows no correlation with radiation pressure. The average expansion rate of the tail (twice the transverse velocity) determined from the fit widths in Table 3.1 is 2.0 ± 0.4 km/s in

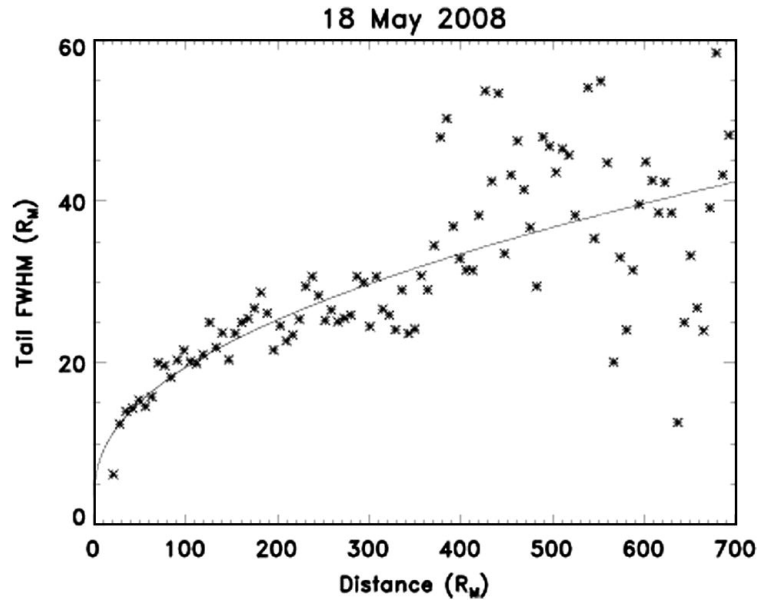


Figure 3.8 Projected distance down-tail versus the FWHM of a Gaussian fit to the tail width. Over plotted is the predicted expansion of an atom with a 1.2 km/s transverse velocity component. The Gaussian fit to the tail width becomes less reliable with distance as the signal to noise level drops with distance from the planet.

Table 3.1. FWHM of Gaussian fits to the tail width and transverse velocity components for each observation of the sodium tail.

UT date	40 R_M (R_M)	110 R_M (R_M)	300 R_M (R_M)	500 R_M (R_M)	V_{\perp} (km/s)
(1)	(2)	(3)	(4)	(5)	(6)
31 May 2007	13.6 ± 3.8	26.5 ± 2.0	28.0 ± 5.0	27.4 ± 5.4	1.1 ± 0.2
2 June 2007	19.7 ± 2.6	24.7 ± 2.2	28.7 ± 2.9	57.6 ± 16.5	0.7 ± 0.2
3 June 2007	NA	22.2 ± 2.1	26.5 ± 2.1	32.8 ± 4.8	1.0 ± 0.1
12 Nov 2007	NA	23.0 ± 3.5	30.2 ± 3.3	37.8 ± 18.0	0.8 ± 0.6
18 May 2008	14.4 ± 2.4	20.5 ± 2.4	28.4 ± 4.0	46.1 ± 2.8	1.2 ± 0.1
Average	15.9 ± 3.3	23.4 ± 2.3	28.4 ± 1.3	40.3 ± 11.9	1.0 ± 0.2

good agreement with the 1.9 ± 0.3 km/s obtained in observations presented in Potter & Killen (2008).

3.5.3 Down-tail Transit in a Steady Escape

The variation in emission observed in the extended tail profiles results naturally from the strong dependence on radiation acceleration. As mentioned earlier, this dependence is comprised of three separate effects: radiation acceleration (1) enhances the rate of escape, and (2) determines how far atoms travel down-tail before ionization, while (3) the down-tail velocity determines how much solar flux will be made available for resonant scattering. Considering orbital positions alone, the observations made in November 2007 (strong tail) and January 2008 (non-detection) effectively isolate the latter two of these three effects. With comparable radiation acceleration upon ejection from the surface, the escape rates should be quite similar at these times assuming steady state sources. Under steady state conditions, a similar radiation pressure liberated roughly the same amount of sodium, but heliocentric velocity changed sign when Mercury was on the outward and inward leg of its orbit, respectively. As shown in Fig. 2.16 and 3.6, resonant scattering occurred at opposite sides of the Fraunhofer well, so that identical fluxes of sodium into the tail would result in very different observed brightness for these two cases. For the January 2008 non-detection, Doppler shifting into the Fraunhofer absorption feature stagnated the neutral flow downstream, so that the atoms presumably were mostly ionized by the time they had emerged from behind the coronagraph mask. Neutrals that survived long enough to come into view radiated very little on 15 January 2008, because the incident flux available for scattering was only 5% of the solar continuum. The results of a 1-D calculation for the radiation acceleration (described in Section 3.5.1) for the 12 November 2007 and 15 January 2008 observations are plotted in Fig. 3.9, quantitatively revealing the effects of a large difference in scattering and radiation acceleration as the cause of the measured

brightness variation. Since sodium scatters more sunlight at D-line wavelengths than at any other wavelength, scattering rates in 3.9 are approximately proportional to the acceleration as shown on the y-axis of Fig. 3.9.

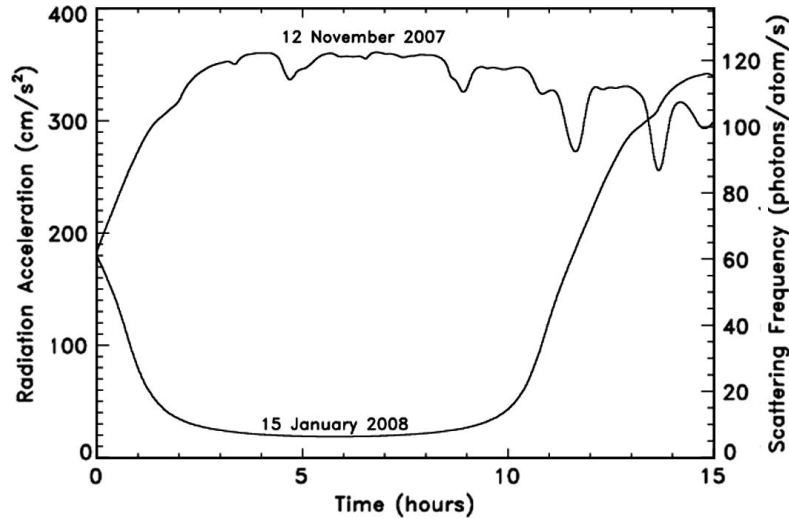


Figure 3.9 Comparison of predicted accelerations and scattering rates or g -values for 12 November 2007 and 15 January 2008 observation dates. Atoms will have traveled 1940 and 340 R_M from the planet respectively during this 15 hour period. The large well shown in the 15 January 2008 and wiggles shown in the 12 November 2007 acceleration profiles correspond to Fraunhofer absorption features in the solar spectrum.

3.5.4 1D Estimation of escape rates

It is possible to compute brightness profiles produced from different escape rates for the purpose of comparison with our two sets of observations which were taken over daily (top) and monthly (bottom) timescales. To do so, a constant flux of atoms under the force of radiation pressure alone is accelerated away from Mercury and ionized using 1 min time steps. A rate coefficient derived from the theoretical ionization cross-section for the quiet Sun was determined by Huebner et al. (1992) and was scaled with heliocentric distance to be applied to these conditions. Scattering rates were calculated for every pixel using the estimated Doppler shifts. Escape rates were found by a least

squares fit using a test range of $(3.0-14.0) \times 10^{23} \text{ atoms s}^{-1}$. Gravity and shadowing effects from the disk were omitted. This method assumes single scattering, and that optical depth is small for both D1 and D2 over the entire down-tail path length. For coronagraph observations made in 2007 and 2008 the results appear in Fig. 3.10, organized into measurements made over a 4 day times span and a several month time span.

The escape rates quoted in Fig. 3.10 are approximate lower limits on the amount of Mercury's Na that leaves the surface-bound exosphere. This is because Na which is ejected close to the minimum escape energy can spend significant time climbing out of Mercury's gravity, during which time a substantial fraction is ionized. Also, since an upper limit on the down-tail velocity is used in the calculation, this corresponds to an upper limit in the scattering rate, meaning more atoms may be necessary to produce the observed brightness. Given these considerations, the escape rate at maximum radiation pressure on 12 November 2007 was significantly larger than any previously published estimates (Schmidt et al., 2010).

The best candidate in Fig. 3.10 for short term, hourly changes in escape occurs on 12 November 2007 at nearly the maximum radiation acceleration experienced at Mercury. Unfortunately, this profile also exhibits the highest noise due to sky subtraction in our data sets. Leblanc et al. (2009) attributed hourly changes in localized emission to changes in the radial component of the IMF; however, total emission showed little variation in their study. Sprague et al. (1997) found diurnal variations with emission highest in morning, and enhanced emissions localized about radar-bright regions on the planet's surface. Such studies suggest that variation in flow rates into the tail on hourly timescales may be common. Analysis of short term variability merits further investigation in conjunction with modeling and additional data near this orbital phase in order to better characterize the baseline rate of atmospheric escape.

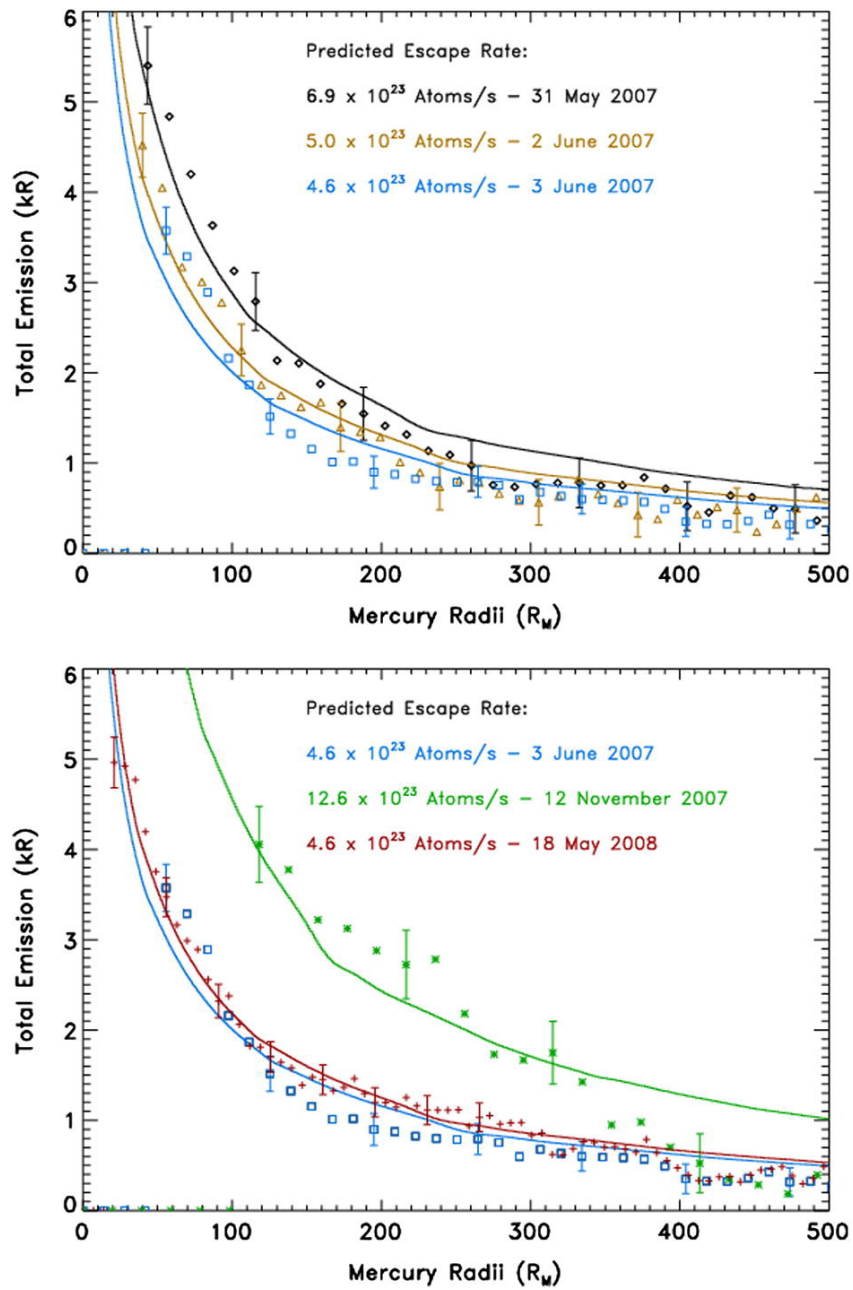


Figure 3.10 Total emission in kiloRayleighs for three observed sodium tails over short timescales spanning 4 days (top) and long timescales spanning nearly 1 year (bottom). The recorded total emission shown is the summed emission at pixel spaced radial distances from Mercury. Predicted emission from a fixed escape rate found from a least squares fit is the over plotted curve.

In all but one of the tails imaged during the first two years of this study, increased escape rates were found at times of higher radiation acceleration. Furthermore, the 18 May 2008 outlier of this trend is within the uncertainty limit. Near the surface, the exospheric depletion corresponding to these increased escape rates has been observed by other groups. Observations when Mercury is on the out-bound leg of its orbit by Potter & Morgan (1997) and Potter et al. (2007) demonstrate a trend in which exospheric column density decreases as radiation acceleration increases. A 4 year investigation of emissions at Mercury's disk by Sprague et al. (1997) could not confirm this result, however. As radiation pressure increases, the global emission reduction totaling 20% found by Potter et al. (2007) is approximately anti-correlated with the tail emission increase in the coronagraph data. Although both data sets show considerable scatter, this suggests the general expectation that losses in the surface-bound exosphere result in gains to the tail's population. Assuming these losses in the Na exosphere with increasing radiation pressure populate the tail, and that escape rates are negligible at minimum radiation pressure, then our 12.6×10^{23} atoms s^{-1} into the tail would be 20% of a surface source rate, i.e., 6.3×10^{24} atoms s^{-1} . This source rate is in agreement with the $(5-9) \times 10^{24}$ atoms s^{-1} total source estimated by Ip (1990), and slightly above the 5×10^{24} atoms s^{-1} assumed by McClintock et al. (2008) based on MESSENGER measurements.

However, previous escape rate estimates based on ground-based spectroscopic and in situ measurements are less than those presented here. For example, the 31 May 2007 observation yields an escape of 6.9×10^{23} atoms s^{-1} . This image was taken with identical orbital phase to a spectrograph tail measurement made by Potter & Killen (2008) on 12 June 2006, in which approximately half this escape rate was estimated. The greatest escape rate in the Potter & Killen (2008) study is $4.9 \pm 1.1 \times 10^{23}$ atoms s^{-1} , and occurred during the largest radiation pressure of 155.5 cm s^{-2} .

If a linear interpolation of escape with radiation acceleration is assumed this is again nearly half the escape rate estimated in our findings. This may suggest that a weakened source of high energy Na atoms was present during their 2006 observations; however the authors note uncertainties due to shadowing, and some atoms lying outside the projected slit length of $\sim 6 R_M$.

Using an initial anti-sunward velocity of 2 km/s, McClintock et al. (2008) find a lower limit of 6×10^{23} atoms s^{-1} escaping during the first MESSENGER fly-by. Similar radiation acceleration occurred in the opposite orbital leg during our 12 November 2007 measurement, suggesting a very large escape rate of 12.6×10^{23} atoms s^{-1} , though admittedly this was also the date with the highest noise levels. I propose that this difference in rate of escape is due to a change in radiation pressure with time as shown in Fig. 3.9. This would suggest that the escape rates are governed not only by radiative forces upon the initial ejection of surface sodium, but on how these forces are sustained in the atom's subsequent motion.

Chapter 4

Modeling The Sodium Tail

4.1 Introduction

This chapter details a 3-dimensional numerical model of Mercury's sodium exosphere. This tool enables characteristic properties of the different sources sustaining the exosphere to be simulated for direct comparison with observations of the Na exosphere. It is the only model which has been developed for simulating emission in the distant sodium tail. It is also the first model of Mercury's exosphere to include a full treatment of temperature dependence in atom-surface interactions (Yakshinskiy & Madey, 2005), as well as spatial anisotropies both in the Na surface concentration (Evans et al., 2013) and ion precipitation (Winslow et al., 2012), based on the MESSENGER spacecraft data.

4.2 Numerical Monte Carlo Model

While a 1-dimensional method is sufficient for estimating the escape flux, investigating the source mechanisms at the surface which sustain this escape requires three dimensions. A kinetic Monte Carlo approach is described in this section with results in chapter 5. The essential elements in the model include the gravity of Mercury and the Sun, radiation pressure, photoionization, the speed and direction of ejection from the surface, parameters governing atom-surface interactions, and a thermal model of the surface.

4.2.1 Original Lunar Code

The present model for Mercury has its origins in a numerical Monte Carlo model of the lunar exosphere presented in Wilson et al. (2003), and much of the fundamental architecture remains the same. In the original lunar model, $\sim 10^4$ test particles, each representing many sodium atoms, were launched from random locations on the lunar surface in random directions. The particle launch times were randomly distributed over the duration of a simulation, chosen to be several photoionization lifetimes for sodium to achieve steady state between ejection and ionization rates. The particle's velocity was initially chosen at random within a 0.1 km s^{-1} range about a center velocity. The equation of motion was integrated using a 4th order Runge-Kutta algorithm with an adaptive time step, considering the instantaneous acceleration by radiation pressure and the gravity of the Moon and Earth. Radiation pressure was switched off in the umbra where atoms are not illuminated. Scattering, and hence radiation pressure, are calculated using the heliocentric velocity and a solar spectrum normalized for intensity at 1 AU. After running the model many times at different increments in ejection velocity, the results can be back-filtered and weighted to give an energy distribution. A total release rate in atoms per second is chosen, so that each test particle in the model represents a collection of atoms that decreases in number with photo-ionization over time. The line of sight column density is computed by collapsing the three dimensional result along an axis. Brightness is calculated based on each particle's incident Doppler-shifted solar flux, the photo-ionization loss, the solar disk visibility, and the line of sight column density of test particles. The Wilson et al. (2003) model provides an outstanding foundation for a simulation of Mercury's exosphere. This section describes the Mercury simulation in detail and documents my adaptation. Elements in this section are hard coded directly into the model, whereas parameters

in the following Section 4.3 are inputs specified by the user that are specialized to each model run.

4.2.2 Adaptation for Mercury

The model of Mercury’s sodium exosphere releases particles from the surface at a defined rate. Monte Carlo methods are used to select the location and velocity of the particle’s ejection from within specified distributions. Each particle represents a large number of Na atoms. The 3-dimensional spatial distribution of $\sim 10^6$ particles is calculated from their trajectories governed by radiation pressure and gravity. After time-integrating the effects of photoionization, the brightness is determined from the line-of-sight column density in Earth’s direction and the incident solar flux in each particle’s Doppler frame.

Integration Technique

The motion of particles in the simulation is governed by the equations:

$$\begin{aligned}\frac{d^2x}{dt^2} &= -\frac{GM_{\odot}x_{\odot}}{r_{\odot}^3} - \frac{GM_Mx_M}{r_M^3} + \frac{\gamma hx_{\odot}}{mr_{\odot}} \left(\frac{g_{D1}}{\lambda_{D1}} + \frac{g_{D2}}{\lambda_{D2}} \right) \\ \frac{d^2y}{dt^2} &= -\frac{GM_{\odot}y_{\odot}}{r_{\odot}^3} - \frac{GM_My_M}{r_M^3} + \frac{\gamma hy_{\odot}}{mr_{\odot}} \left(\frac{g_{D1}}{\lambda_{D1}} + \frac{g_{D2}}{\lambda_{D2}} \right) \\ \frac{d^2z}{dt^2} &= -\frac{GM_{\odot}z_{\odot}}{r_{\odot}^3} - \frac{GM_Mz_M}{r_M^3} + \frac{\gamma hz_{\odot}}{mr_{\odot}} \left(\frac{g_{D1}}{\lambda_{D1}} + \frac{g_{D2}}{\lambda_{D2}} \right)\end{aligned}\tag{4.1}$$

where r_{\odot} and r_M are the instantaneous distances to the body centers of the Sun and Mercury, respectively, G is the gravitational constant, M is the body mass and h is Plank’s constant. The values x_M , x_{\odot} , etc., represent the scalar projection of each particle’s distance to the Mercury and Sun centers, respectively, along a Cartesian axis. The instantaneous scattering, $g(r_{\odot}, r'_{\odot})$, is evaluated using Eq 3.9 and multiplied by the fraction of the limb-darked solar disc, γ , that is visible from each particle’s location (Cox, 2000). The set of second-order differential equations in 4.1 is solved using a 4th

order adaptive step-size Runge-Kutta method. For the details of this integration method and the adaptive time step algorithm, the reader is referred to Section 16.2 of Press et al. (2007). The Runge-Kutta integrator computes the equation of motion for each test particle along each Cartesian axis over one time step given its instantaneous initial values, e.g., x_0, \dot{x} .

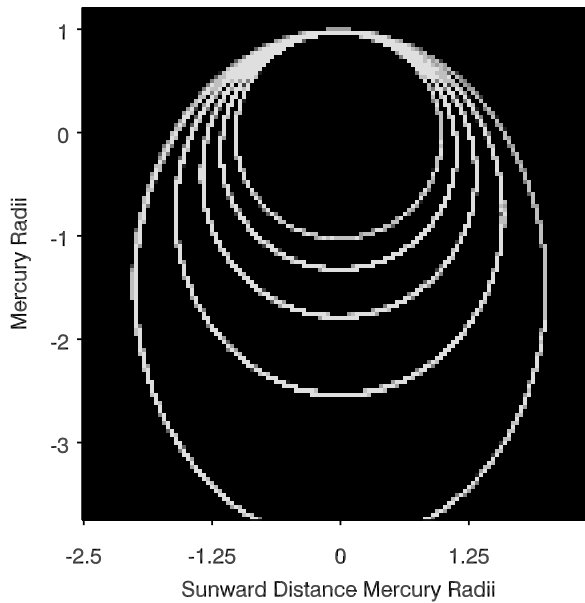


Figure 4.1 Particles released tangentially from Mercury’s north pole. Increasingly larger orbits correspond to ejection velocities of 3.006, 3.2, 3.4, 3.6 and 3.8 km s^{-1} . The apex of the inner-most orbit is about 120 m from Mercury’s surface.

The result of the integration is validated by testing the orbits of particles in the absence of radiation pressure, performed in a stationary frame with the origin at solar system barycenter. For each point on the surface at the time of ejection, Mercury’s instantaneous velocity is added as a vector to the initial velocity of the particle. Vertically ejected particles are confirmed to escape with a threshold of $v_e =$

$\sqrt{\frac{2GM}{r}} = 4.25 \text{ km s}^{-1}$. Tangentially ejected particles are verified to attain circular orbits at $v_O = \frac{v_e}{\sqrt{2}} = 3.0 \text{ km s}^{-1}$. Fig. 4.1 shows the result of particles tangentially ejected from Mercury's north pole at this minimum orbital velocity, v_O , as well as at several higher speeds. Stable bound orbits about both the planet and the sun are found in a fixed coordinate frame. The equivalent calculation of orbital motion using a single body and an inertial frame is trivial. The Hill radius, where solar gravitation becomes greater than the gravitational force from Mercury's, varies from 70 to 105 R_M over Mercury's orbit so that the gravity of both bodies is relevant to atoms in these data sets.

Coordinates Frames

The original lunar model was implemented in an inertial frame in which one Cartesian axis was centered at the Moon and fixed to the sun-ward direction. In the case of Mercury, a Cartesian coordinate frame with the origin at the solar system barycenter at the J2000 epoch seemed more fitting. This frame was chosen for simplicity, as it is fixed with respect to time, and is a default reference frame for the Jet Propulsion Laboratory's Horizons ephemeris system (<http://ssd.jpl.nasa.gov/horizons.cgi>) so that orbital elements computed in the model can be quickly cross-checked. The architecture of the Mercury model was constructed with the objective of being directly comparable to observations from the MESSENGER spacecraft. The information needed to compute the flight path of the spacecraft is available from NASA's Jet Propulsion Laboratory in the form of a SPICE (Spacecraft Planet Instrument C-matrix Events) kernel (Acton, 1996). Therefore, the coordinate system follows the SPICE standard in which the X-Y plane is taken to be the Earth's orbit at the J2000 epoch.

The SPICE ephemeris data allows a calculation of the position of any major solar system body with respect to another at a given time. Hard coding this capability into

the Mercury simulation allowed many advances from its lunar code predecessor. For example, at any given time, the coordinates of the Earth with respect to Mercury permit the computation of a rotation matrix such that a particular Cartesian axis aligns with the line of sight. The matrix product with the particle coordinates can then be collapsed along one axis to give the line of sight column density from Earth. Column densities in the lunar code were limited in that the model's output could only be viewed from directions along a body-fixed Cartesian axis.

Discrete Velocity and Spatial Distributions

Initially, the Wilson et al. (2003) model accounted for a source's energy distribution by running the simulation many times at different velocity bins and back-filtering the results to a desired weighting scheme. I instead chose to program a Monte Carlo method in which the ejection energy is selected at random from within a distribution. To reduce statistical noise, the simulation is iterated many times, each with the random number seed passed; the subsequent results are stacked and averaged along the line of sight. Some mechanisms, like ion sputtering, may eject atoms preferentially in the direction of zenith (Johnson et al., 2002). The Monte Carlo surface ejection was modified to allow anisotropic weighting of the ejection angles relative to the surface normal. The weighting schemes for both ejection velocity and ejection angle are specified inputs for simulating different processes. As the planet's rotation states are also encoded in the SPICE ephemeris data, it is possible to convert between planetographic longitude and latitude coordinates, local time coordinates, and non-inertial J2000 coordinates. This enables the simulation of localized sources of the exosphere, whereas spatially homogeneous sources were previously assumed.

Surface Interactions

Particles impacting the surface during the simulation either adsorb to the surface or bounce in a random direction. In my Schmidt et al. (2012) model, atoms that impact the cold ~ 100 K nightside were assumed to adsorb to the surface as several authors have proposed (e.g., Leblanc & Johnson, 2003; Burger et al., 2010). I fit a dayside sticking probability of $S = 1.55 - (6.53 \times 10^{-3})T + (1.1 \times 10^{-5})T^2 - (6.7 \times 10^{-9})T^3$ to the laboratory measurements of Na adsorption to thin SiO₂ films of various temperatures by Yakshinskiy & Madey (2005). With each bounce, a particle's energy settles toward an energy characteristic of the local surface temperature, $E_{Thermal}$, according to a thermal accommodation coefficient α , where $\alpha = (E_{Final} - E_{Initial}) / (E_{Thermal} - E_{Initial})$. For an α quartz (SiO₂) surface at 600 K, the thermal accommodation was determined to be 0.62 (Hunten et al., 1988). However, subsequent models have shown α more likely to be in the range of .1 to .3 (e.g., Mouawad et al., 2011). Under these conditions, test particles in Mercury's hottest regions generally experience several bounces across the dayside, with high adsorption to the nightside. As exospheric Na reabsorbed to the surface is likely to bond ionically with oxygen (Madey et al., 1998). Therefore, the same ejection characteristics are applied to both original regolith sodium as well as exospheric Na absorbed by the surface.

Surface Temperatures

The localized temperature of Mercury's surface is used in modeling the behavior of particles impacting the planet. Initially, I neglected the thermal inertia of Mercury's lithosphere. Following Leblanc & Johnson (2003), the dayside surface temperature in Schmidt et al. (2012) was assumed to vary as:

$$T(\lambda, \mu) = T_{Night} + (T_{Sub-solar} - T_{Night})[\cos(\lambda)\cos(\mu)]^{1/4} \quad (4.2)$$

where T_{Night} is the average nightside surface temperature of 100 K and λ and μ are the latitude and longitude relative to the sub-solar point. To first order, the sub-solar point temperature is well represented as a blackbody in thermal equilibrium:

$$T_{Sub-solar} = T_{\odot} \left[\left(\frac{R_{\odot}}{r_{\odot}} \right)^2 \frac{1-a}{e} \right]^{1/4} \quad (4.3)$$

where R_{\odot} is the solar radius; a is the 0.106 albedo (Cox, 2000); e is the planet's emissivity, fixed at 0.95 (Hale & Hapke, 2002); and T_{\odot} is the effective solar temperature (5777 K), giving 700 and 570 K at aphelion and perihelion, respectively.

Recent estimates based on MESSENGER Gamma Ray Spectrometer data indicate that the concentration of sodium in the top few cm regolith depends on the maximum annual surface temperature (Evans et al., 2013). Prompted by this development, I have since improved the simple model of Eq. 4.2 to include thermal conduction. The impetus for this correction stems not only from the capability to map the Na surface concentration, but also to better simulate the temperature dependence of sources and surface interactions. In future work, the thermal gradient in the soil may also prove useful in incorporating diffusion effects from depth into the model, an effect which is quite poorly constrained. It's worth noting that this is the first time a model of an exosphere has incorporated a dawn-dusk asymmetry induced by thermal inertia in a body's lithosphere. Considering conduction, energy balance at the surface requires:

$$\frac{S_{\odot}(1-a)}{r_{\odot}^2 e} \cos(\lambda) \cos(\mu) = \sigma T^4 - \kappa \frac{dT}{dz} \quad (4.4)$$

where S_{\odot} is the total solar irradiance in W m^2 at 1 AU (Cox, 2000), σ is the Stefan-Boltzmann constant and the thermal conductivity, κ , is $1.8 \times 10^8 \text{ erg cm}^{-1} \text{ deg}^{-1} \text{ sec}^{-1}$ (Wang & Ip, 2008). The temperature gradient at the surface in the last term is given

by the one dimensional equation for the heat conduction along a direction z that is normal to the surface:

$$\rho c \frac{\partial T}{\partial t} = \frac{\partial}{\partial z} \left(\kappa \frac{\partial T}{\partial z} \right) \quad (4.5)$$

where ρ is the mass density, taken as 2.8 g cm^3 and the specific heat, c , is $4.6 \times 10^7 \text{ erg g}^{-1} \text{ K}^{-1}$ (Wang & Ip, 2008). Eq. 4.5 is solved with the aid of an IDL code provided by John Spencer (available at <http://www.boulder.swri.edu/spencer/thermprojrs>), with the slab boundary method described in Spencer et al. (1989). An endogenic heat flow of $.02 \text{ W m}^{-2}$ is assumed to cross the model's lower slab boundary (Vasavada et al., 1999).

Due to thermal inertia, the dusk hemisphere is slightly hotter than the dawn hemisphere. As an example, the equatorial surface temperature is shown in Fig. 4.2 as a function of time. As Mercury's orbit becomes approximately tidally synchronous near perihelion, the incident solar flux at a given surface location is not sinusoidal over a diurnal period. In fact, Mercury's orbital motion is so fast at perihelion that the westward motion of the Sun completely stops and briefly becomes retrograde. The time variation of solar insolation across the surface is computed using SPICE. To demonstrate the thermal effects of Mercury's spin-orbit resonance, Fig. 4.3 shows the result of this thermal model for a point on the equator over one diurnal period. This profile can be compared directly with Fig 1. of Wang & Ip (2008), in which equations equivalent to 4.4 and 4.5 are solved using a Crank-Nicholson finite difference routine for the same surface point. Although I have included endogenic heat flux and emissivity, the results of this thermal model bare no significant deviations from that of Wang & Ip (2008). In this sense, the solution is validated against their thermal modeling.

The geographic location of the sub-solar point alternates with each successive orbit, a consequence of the planet's 3:2 spin orbit resonance. The variation of the

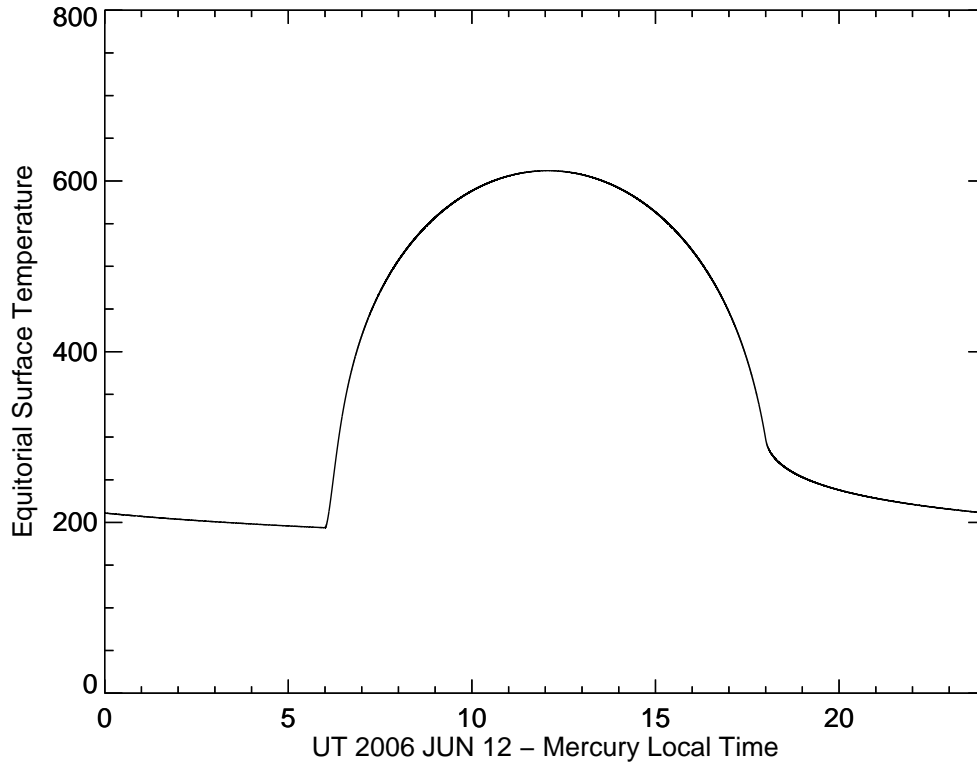


Figure 4.2 Modeled equatorial surface temperature as a function of local time. The asymmetry of the profile results from the thermal inertia of Mercury’s lithosphere and induces spatial asymmetries in exospheric sources and surface interactions.

maximum surface temperature over one diurnal period is shown in a Mercator projection in Figure 4.4. The planet’s 3:2 spin-orbit resonance and eccentric orbit produce two distinct hot poles. The slightly non-circular shape of these hot poles is again a consequence of thermal inertia in Mercury’s lithosphere. Very recent studies with the MESSENGER Gamma Ray Spectrometer (GRS) have shown the surface concentration of sodium with a depth of a few cm in the regolith may be an inverse function of the maximum surface temperature (Evans et al., 2013). If this is the case, longitudinal

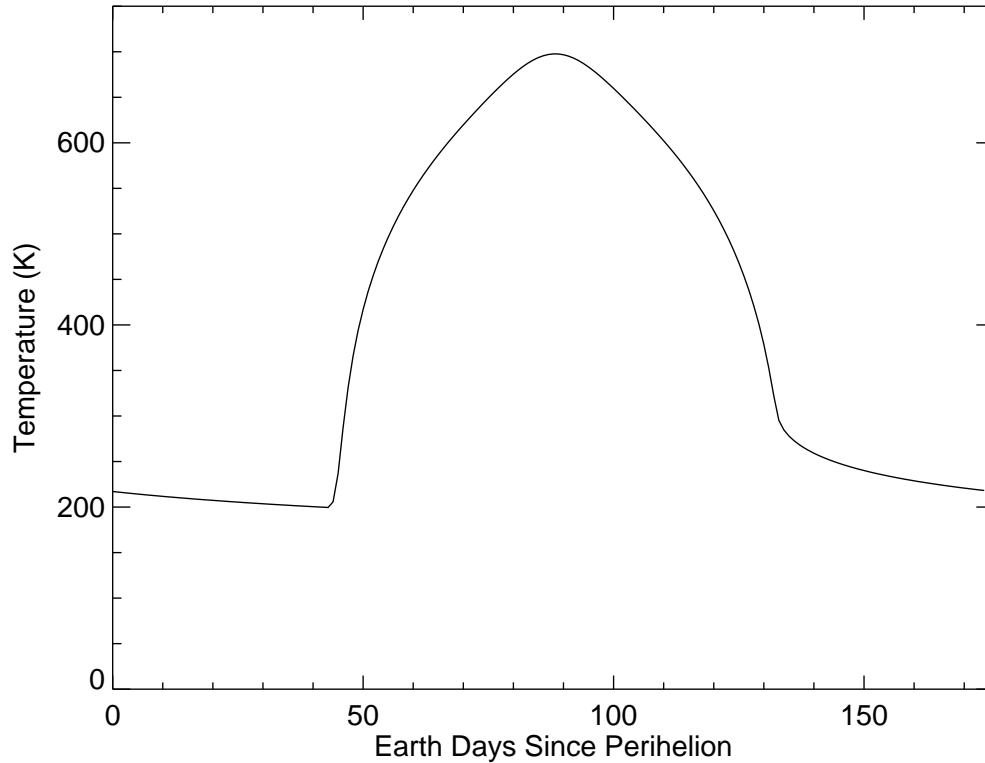


Figure 4.3 The modeled surface temperature for a point on the equator that intercepts the sub-solar point at perihelion. Due to the planet's 3:2 spin orbit resonance, a diurnal period is 175.94 days, and an opposite hemisphere faces the Sun with each orbit.

inhomogeneities in the planet-wide Na concentration may also exist and be distributed within the regolith inversely proportional to Fig. 4.4.

Photoionization and solar drivers

A high resolution solar spectrum is needed to accurately predict the feedback characteristics of radiation pressure. The 1-dimensional solution for Mercury presented in Schmidt et al. (2010) utilized the Bass2000 solar survey (available at <http://bass2000.obspm.fr>) and scaled to absolute values in the continuum measured

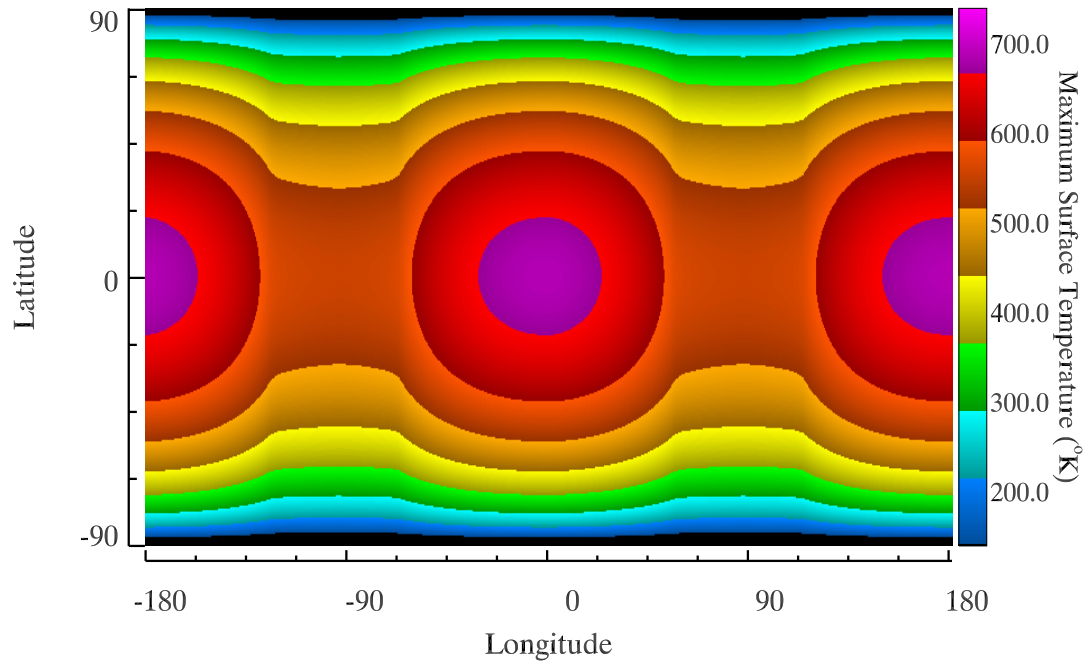


Figure 4.4 Maximum surface temperatures with planetographic location on Mercury. 0° longitude and latitude is defined at the sub-solar point at perihelion.

by the SORCE (Solar Radiation and Climate Experiment) satellite. As the Bass2000 spectrum could in principle contain trace terrestrial contamination, the solar spectrum used by Killen et al. (2009) was subsequently adopted, though deviations between the two were minimal. Doppler shifts in each particle's frame are interpolated to the data points increments of $50 \text{ m}\text{\AA}$. At these visible wavelengths, variation in the scattered flux with solar activity is negligible.

The energy required for singly ionizing a sodium atom is 5.139 eV , corresponding to photon wavelengths short-ward of 2411 \AA . Electron-impact ionization lifetimes are much longer than photoionization lifetimes at Mercury, and while electron-impact ionization dominates in the Io nebula (Carlson et al., 1975), it is negligible here. The

photoionization rate in this work is taken to be 1.69×10^5 s at 1 AU, determined by (Huebner et al., 1992) for the theoretical absorption cross section and subsequently verified in observations of the sodium tail of comet Hale-Bopp (Cremonese et al., 1997). Because sodium has a relatively low ionization potential, the product of the UV flux and the wavelength-dependent cross section for photo-ionization is dominated by solar continuum, so that ionization rates vary by less than $\sim 10\%$ with solar cycle (Huebner et al., 1992; Han et al., 2006). This small variability in UV flux is not corrected for, as the wavelength dependence in the photoionization cross-section remains uncertain. In particular, it has been found that between 500 \AA and 1200 \AA , the experimental cross-section is larger than the theoretical cross-section and shows a broad feature which has yet to be explained (Huebner et al., 1992). Thus solar activity is neglected to good approximation, and the e-folding photo-ionization lifetime for sodium simply increases with distance squared and varies from 4.4 to 10.2 hours at the surface because of Mercury’s eccentric orbit.

The lunar code was adapted so that photo-ionization removes a fraction of atoms from the simulation at each time step in the integration, taking into account each particle’s heliocentric range. Doing so also accounts for shadowing effects by Mercury’s disc; the ionization lifetime increases and radiation pressure decreases in the umbra and penumbra according to distance and the fraction of the solar disk seen.

4.3 Source Processes and Their Intrinsic and Potential Time Variabilities

Mercury’s atmosphere is well approximated as collisionally thin, so that an atom’s velocity retains the properties associated with its source mechanism at the time of surface ejection, modified only by subsequent gravitational and radiative forcing or surface interactions. Energy distributions in exospheric sodium can therefore be non-

Maxwellian. Fig. 4.5 shows a comparison of energy distributions that have been attributed to source processes at Mercury, compiled from several studies. This section summarizes these sources with particular attention to their ability to produce escaping sodium.

4.3.1 Thermal Evaporation

While thermal evaporation may be important in mobilizing atoms about the surface, even atoms that are thermal equilibrium with the hot surface temperature at the sub-solar point are not energetic enough for gravitational escape. As an efficient means of lofting atoms, thermal effects, in combination with radiation pressure, may enable transport from the day to night sides, where atoms stick to the cold surface. If space weather effects do not significantly regulate the Na supply to the topmost surface, thermal desorption rates will possess north-south symmetry and only a slight local time asymmetry (cf. Fig. 4.2). Several measurements indicate that the bulk atmosphere is super-thermal (e.g., Killen et al., 1999). Since thermal Na remains bound, the process cannot be constrained by data of the Na tail. At such low energies, observable D line emissions are confined to being near the disc; the contribution to the tail population is negligible, and thus an in-depth study of this process is not relevant to these data. The efficiency of other source mechanisms, however, has been shown to be temperature dependent, as discussed in the next section.

4.3.2 Photon Stimulated Desorption

Coincidentally, the energy required to liberate sodium from regolith surface grains is approximately equal to the photoionization energy. The solar flux below 2500 Å in wavelength (≥ 5 eV) will photo-desorb Na from Mercury's surface (Yakshinskiy & Madey, 1999). The Sun's specific intensity is higher longward of ~ 2000 Å in the blackbody continuum than at Lyman α (1216 Å), where emission varies strongly with

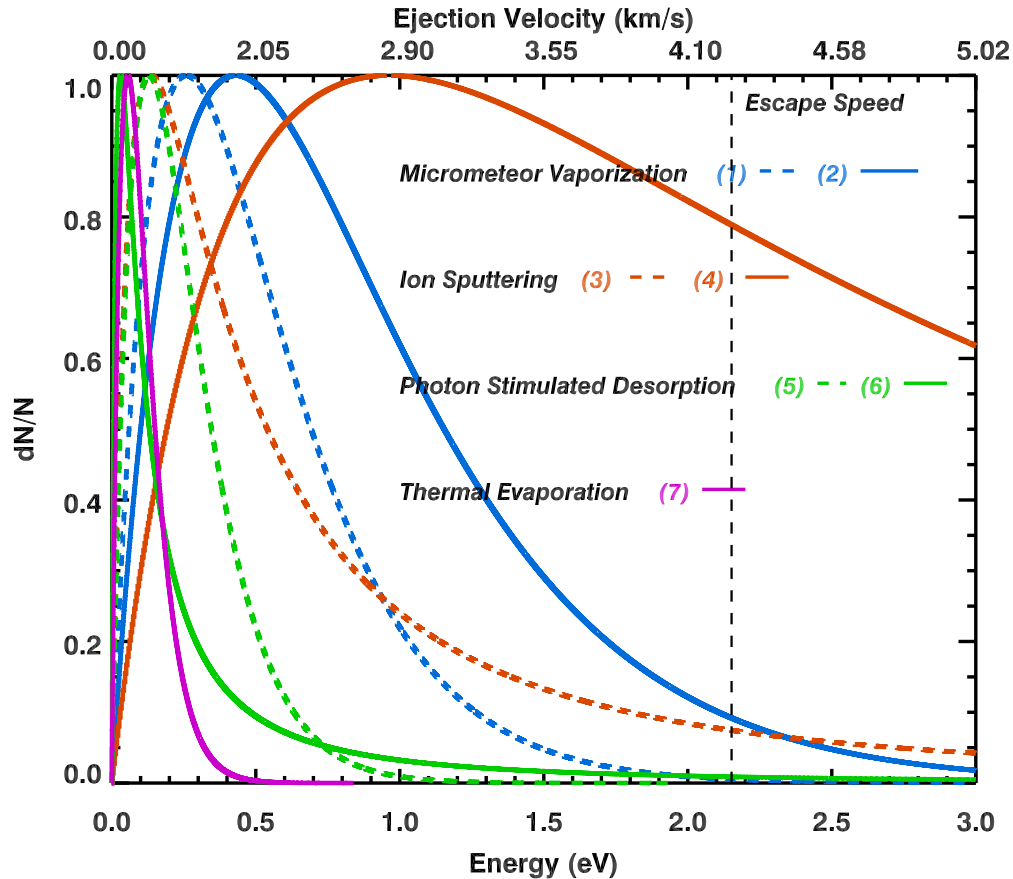


Figure 4.5 A comparison of energy distributions, normalized to the most probable value, for sodium released by various processes that have been applied at Mercury: (1) 3000 K Maxwellian used in modeling by Leblanc & Johnson (2003). (2) 5000 K Maxwellian used in modeling by Mouawad et al. (2011). (3) Distribution fit by Wiens et al. (1997) to measurements of sodium ejected from an Na_2SO_4 surface bombarded by energetic ions. (4) Sigmund-Thompson type distribution for 1 keV protons, applied in modeling by Wurz et al. (2010). (5) 1500 K Maxwellian Leblanc & Johnson (2003) fit to Yakshinskiy & Madey (1999) ESD data. (6) Distribution fit by Johnson et al. (2002) for laboratory measurements of icy surfaces bombarded by 200 eV electrons, modified with a cutoff term at high energies Wurz et al. (2010). (7) Sodium thermalized to 650 K, approximating the sub-solar point surface temperature.

solar activity. Although it has been argued that solar activity significantly affects the PSD rate in Mercury (e.g., Killen et al., 2007; Mouawad et al., 2011), variability in the Herzberg Continuum between 2000 and 2420 Å was estimated to be less than 7% over the last three solar cycles (Krivova et al., 2009). Furthermore, the first three years of the Mercury data set spans during a deep minimum in the solar activity cycle. Solar-driven variability in PSD sources are hence neglected in these simulations.

Empirical energy distributions of desorbed sodium are often derived by time-of-flight measurements under electron bombardment, rather than UV radiation, as a wide experimental energy range for electron-induced excitations is more readily available under laboratory conditions. Electron-stimulated desorption is a charge transfer process similar to PSD, with comparable cross sections and an identical excitation threshold of ~ 4 to 5 eV (Yakshinskiy & Madey, 1999). While desorption of sodium into the exosphere by electrons is negligible compared to that released by photon stimulation, the energy distributions of ejected sodium are quite similar, so that electron stimulated desorption (ESD) measurements can be substituted for the effects of UV photons.

Johnson et al. (2002) have measured the energy distribution of sodium desorbed by 200 eV electrons from an icy surface as:

$$F_{PSD}(E) = \beta(\beta + 1) \frac{EU^\beta}{(E + U)^{2+\beta}} \cos(\theta) \quad (4.6)$$

where θ is the angle of ejection relative to the normal; $\beta = 0.7$ is a parameter determining the shape of the curve; and U is a characteristic energy, equal to 0.052 eV for sodium, related to the surface binding energy. In addition, these authors fit an E^2 falloff to their high-energy data points near 1 eV. As the ejection energy must not exceed that of the impacting photon, I modify Eq. 4.6 for a lower energy tail using the term suggested by Wurz et al. (2010).

Samples that are better analogues to Hermean regolith than water ice are known to desorb Na with lower energies. Yakshinskiy & Madey (1999) found the energy distribution of ESD from SiO₂ surfaces to be similar to that of a 1200 K Maxwellian, but with a higher-energy tail. Leblanc & Johnson (2003) chose a 1500 K Maxwellian to fit these data. The energy distribution of ESD from a lunar sample was found to be shifted toward lower velocities than that of SiO₂, peaking around 0.8 km/s instead of 1 km/s (Yakshinskiy & Madey, 2004). My Schmidt et al. (2012) study simulates both a 1500 K Maxwellian and a higher-energy distribution used in the study by Wurz et al. (2010), where I have imposed a 10 eV cutoff; these are shown in Fig. 4.5 by the green solid and dashed lines, respectively.

Killen et al. (2004) proposed that the supply rate of sodium to the topmost regolith layers is diffusion limited to $10^7 \text{ cm}^2 \text{ s}^{-1}$. The diffusive supply may be enhanced by ion precipitation, impacts, or re-absorption of Na. Increased temperature can also raise the diffusion rates to the topmost layers affected by PSD. Laboratory analysis of PSD yield in lunar samples by Yakshinskiy & Madey (2004) showed efficiency increases by a factor of 10 as the temperature of the sample was increased from 100 to 470 K. This effect was reversible, and was attributed to the enhanced diffusion of Na⁺ to oxygen bonding sites. However, sodium yields via electron-stimulated desorption have been shown to decrease by a factor of 3 as the sample temperature increased from 400 to 600 K (Yakshinskiy & Madey, 2005). No temperature dependence in the PSD yield was considered in the Schmidt et al. (2012) model and the spatial dependence of desorption rates was assumed to be photon limited, varying only with the cosine of the solar zenith angle. It should be noted, however, that proper modeling of the spatial distribution of PSD sites on the surface is currently debated. Na redistribution over the surface remains model dependent (e.g., Leblanc & Johnson, 2003; Mura et al., 2009), and the localized enhancement of PSD yield by ion impacts is not yet quanti-

fied uniquely (Burger et al., 2010). For simulating the distant tail, the precise regional origins of desorbed sodium is not critical, as these inhomogeneities are largely smeared out by solar radiation pressure. Nevertheless, a spatial dependence in the escaping fraction of desorbed atoms is discussed in Section 5.3.1.

Following the very recent MESSENGER detection of inhomogeneities in the surface concentration of Na (Evans et al., 2013), the model's source function was improved to account for second order effects. For a given point on the surface, the local PSD rate is currently evaluated as:

$$\Phi_{PSD} = \frac{N \cos(Z) \int \sigma_{\lambda} \phi_{\lambda} d\lambda}{R^2} A e^{-\frac{E_a}{kT}} \quad (4.7)$$

where N is the sodium concentration per cm^2 per mean free path in the regolith, Z is the solar zenith angle, σ_{λ} is the PSD cross section in cm^2 , ϕ_{λ} is the solar spectral irradiance at Earth in photons $\text{cm}^{-2} \text{s}^{-1}$ and R is the range to the Sun in AU. N is equal to $7.4 \times 10^{14} (f_{Na})$ (Killen et al., 2001). To first order, the abundance, f_{Na} , is assumed to vary with the maximum biannual surface temperature as $0.056 \times T_{max}^{-0.345}$, which is consistent with current estimates based on MESSENGER Gamma Ray Spectrometer data (Evans et al., 2012, 2013). A Mercator projection of T_{max} in planetographic coordinates was shown in Fig. 4.4. The temperature dependence of the yield follows an activation energy, E_a , of 0.02 eV (Yakshinskiy & Madey, 2004). Finally, two constants have been combined into A : a 1/3 reduction in yield owing to porosity (Cassidy & Johnson, 2005) and a factor of 10.2 to normalize the temperature dependence to unity at 100K, where the measured PSD cross-section for a lunar sample is $\sigma = 10^{-20} \text{ cm}^2$ at $h\nu = 5 \text{ eV}$ (Yakshinskiy & Madey, 2004). The wavelength dependence of the PSD cross-section is not well known, but 10^{-20} cm^2 is commonly assumed over wavelengths short of $h\nu = 5 \text{ eV}$ and will be adopted here. The integrated solar irradiance, ϕ , is $2.2 \times 10^{14} \text{ photons cm}^{-2} \text{ s}^{-1}$ over wavelengths $h\nu \geq 5 \text{ eV}$ as measured by the SORCE

(Solar Radiation and Climate Experiment) spacecraft. At 0.4 AU, Eq. 4.7 gives a total PSD rate of 2.4×10^{25} Na atoms s^{-1} and a flux of 1.4×10^8 Na atoms $cm^{-2} s^{-1}$ at the sub-solar point. As this is nearly a decade in excess of the (Killen et al., 2004) estimate of the diffusion limited Na supply, diffusion rates therefore restrict PSD in hot regions where adsorbed Na is negligible.

Photo-desorbed Na should display north-south symmetry provided there is hemispheric symmetry in the surface concentration, N . However, MESSENGER studies have inferred latitudinal asymmetries in both the location and the flux of impacting solar wind ions (Winslow et al., 2012), and local time asymmetries in Na^+ photo-ions (Raines et al., 2013). To account for the influence of impacting ions on PSD in this simulation, the diffusive supply to the topmost surface is raised by the unity-normalized precipitation rate times an enhancement factor, κ , following Burger et al. (2010). In addition to cusp regions, PSD may be enhanced near dawn from cold-trapped and ion-implanted Na as well as ion-enhanced desorption sites accumulated during the 88 day Mercury night (e.g., Sprague, 1992).

To better estimate the energy imparted to a photo-desorbed atom, I have since fit the Yakshinskiy & Madey (1999, 2004) laboratory measurements of the energy distributions with 2 different functions as shown in Fig. 4.6. A kappa distribution ($\kappa = 1.8$, 500K) is offset by $.5 \text{ km s}^{-1}$ in order to match the solid line of the lunar samples. The dotted line shows an 800K Maxwellian, offset by $.2 \text{ km s}^{-1}$, providing a good fit to the faster desorption measured from quartz (SiO_2) surfaces.

4.3.3 Ion Sputtering

A formula proposed by Thompson (1968) is commonly applied to the energy distribution of sputtered sodium in Mercury (e.g., Lammer et al., 2003; Wurz et al., 2010). Such a distribution results in nearly all physically sputtered atoms leaving Mercury's gravitational well. The orange dotted line (4) in Fig. 4.5 shows the distribution used

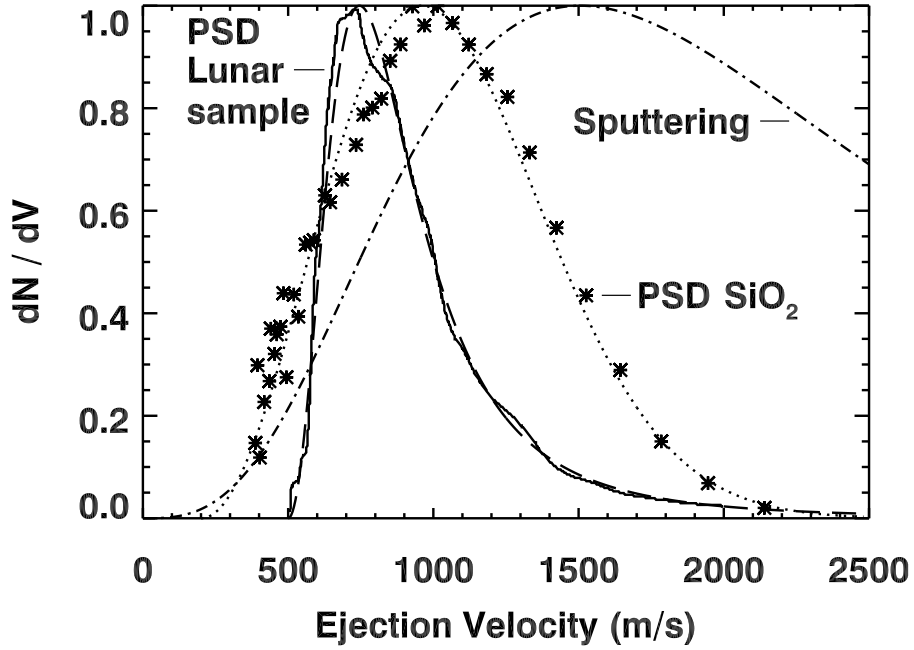


Figure 4.6 Speed distributions for photo-desorbed and sputtered Na. The thick black line and asterisks show distributions from time-of-flight measurements of desorption from a lunar sample and SiO_2 surfaces, respectively (Yakshinskiy & Madey, 1999, 2004). Input parameters in this exosphere model include the dashed and dotted line fits to these data, as well as the high velocity dash-dot profile fit by Wiens et al. (1997) to Na sputtered from sodium sulfate.

in the study by Wurz et al. (2010) for the case of 1 keV solar wind protons, which I assume here to be typical impactors in regions of open field lines.

Other empirically derived energy distributions suggest the sputtered population may be less energetic. The sputtered velocity distribution measured by Wiens et al. (1997) (Fig. 4.6 dash-dotted line) is used in my current study, although it should be noted that many models invoke a theoretical Sigmund-Thompson energy distribution that is substantially higher (e.g., Burger et al., 2010; Wurz et al., 2010). Wiens et al. (1997) fit a Thompson-Sigmund energy distribution of the form:

$$F_{IS}(E) \propto \frac{EU}{(E+U)^\alpha} \cos(\theta) \quad (4.8)$$

where θ is the angle of ejection relative to the surface normal, and obtained a profile spread over a much lower range of energies. Sodium ejected from a Na_2SO_4 pressed powder surface, bombarded by energetic Ar^+ ions, resulted in a peak ejection speed of 1.5 km/s, corresponding to $U = 0.27$ eV with $\alpha = 3.0$. Cassidy & Johnson (2005) suggested significant deviations from the energies found by Wiens et al. (1997), and a reduction in yield because of further interactions with surface grains after the initial release of the sputtered atom. However, the relative amount of high-energy sputtered sodium was independent of the effect, so that Eq. 4.8 remains valid with regard to the escaping population of prime consideration here. Fig. 4.5 shows the result of Wiens et al. (1997) as the solid red line (3), in contrast to the very high-energy distribution assumed by Wurz et al. (2010), as the dashed red line (4).

As there is clearly much disagreement regarding energy distributions and rates of sputtering at Mercury, the model was tested for both the fast and slow distributions proposed, and I now discuss the process in more detail. The total source rate for atoms sputtered from the surface is a product of the ion flux reaching the surface, the concentration of sodium in the regolith, and the effective yield of atoms per ion collision. The effective yield varies by ion species and better constraints are still needed. In addition, heavier ions can more easily reach the surface because of their larger gyro-radii. Killen et al. (2004) suggested 0.19 atoms per ion for a typical mix of solar wind particles, which I take as an upper limit. Dukes et al. (2011) showed 4 keV He^+ sputtering to have yields of 0.037 atoms/ion. While these solar alpha particles make up only 5% of the solar wind, their contribution to sputtered sodium has been estimated at 30% that of protons, with all other solar ion populations being negligible (Wurz et al., 2010). Although the yield from heavy ions is much greater than protons and alpha particles, precipitating fluxes of heavier magnetospheric ions are generally

estimated to be 3 to 4 orders of magnitude less than direct solar wind channels via the cusps (e.g., Delcourt et al., 2003; Benna et al., 2010; Mura et al., 2005).

The charged particle precipitation onto Mercury's surface is likely to vary substantially. The average solar wind density more than doubles between apoherm and periherm, from about ~ 30 to ~ 70 cm^{-3} . Furthermore, the interplanetary magnetic field (IMF) becomes less radial with distance, so that near periherm a larger surface region is likely to be directly exposed to the solar wind via open field lines (Sarantos et al., 2007). Flux transfer events sporadically increase the precipitation rate in the cusps for just a few seconds (Slavin et al., 2010a). During the most intense solar wind conditions (e.g., a dynamic pressure of 94 nPa, ~ 6 times the average), the precipitating flux integrated over the entire planet was estimated to be as high as 3.0×10^{26} protons s^{-1} (Kallio & Janhunen, 2003; Massetti et al., 2003). For purposes of modeling my Schmidt et al. (2010) wide-field data, I assume an upper limit on the typical precipitation rate of 5×10^{25} protons s^{-1} globally, which still exceeds estimates during typical solar wind conditions (e.g., Massetti et al., 2003; Kallio & Janhunen, 2003; Mura et al., 2005) and during the first two MESSENGER flybys (Burger et al., 2010). Combining this upper limit in particle precipitation, a Na soil concentration equal to 0.0134 as found in the study by (Wurz et al., 2010), and a 0.19 atoms per ion upper limit on the effective sputter yield, this forms a generous estimate of $\sim 1.3 \times 10^{23}$ atoms s^{-1} globally as the maximum contribution by a sputtered source during typical solar wind conditions.

Polar bright spots in sodium D line emission can be used to trace the location of ion precipitation channeled by magnetospheric cusps to Mercury's surface. Because of the tenuous solar wind-magnetosphere interaction, the observed intensity and location of the polar bright spots is variable (e.g., Potter & Morgan, 1990; Sprague et al., 1997; Schleicher et al., 2004; Potter et al., 2006). Using the image-slicer instruments

mounted to the AEOS (Advanced Electro Optical System) telescope, polar bright spots were resolved near $\sim 75^\circ$ latitude by Baumgardner et al. (2008). Recent modeling confirms that the bulk of the particle precipitation occurs at these latitudes during MESSENGER M1 and M2 flybys, with a dispersion of roughly 10° and 50° FWHM in latitude and longitude, respectively, centered about the noon meridian (Benna et al., 2010; Burger et al., 2010). As an input to my Schmidt et al. (2012) model, a 2-D Gaussian with these widths was therefore assumed as the typical spatial distribution of ion precipitation.

After my Schmidt et al. (2012) study, regions of ion precipitation and the surface concentration of Na were refined based on new information from the MESSENGER spacecraft. MESSENGER measurements indicate an average of $\sim 5 \times 10^{24}$ ions s^{-1} precipitate through the cusps, nearly 80% of which are contained in the south (Winslow et al., 2012). In my recent simulations, impacted surface regions are approximated using 2D Gaussians in longitude and latitude based on the Winslow et al. (2012) results. Solar wind ions are supplied to the cusps, centered at 74.7° N and 64° S latitudes. The impacting flux covers a Gaussian 1σ region of 4° latitude and 1.5 hours longitude in the north and 6° latitude and 2.3 hours longitude in the south. Thus 95% of the plasma impacts over 5.2×10^5 km^2 and 2×10^6 km^2 in the north and south, respectively, nearly 7% of the dayside surface. The assumed cusp locations and sizes are based on the Winslow et al. (2012) results, which are averaged over many MESSENGER passes. At a given point in time, such parameters are of course subject to both seasonal and space weather drivers (e.g., Sarantos et al., 2007).

Ions precipitate at lower latitudes on the nightside compared to the cusps due to solar wind compression of the magnetotail and the dayside magnetopause. Some models have shown that nightside ion precipitation peaks near $+35^\circ$ latitude (e.g., Delcourt et al., 2003; Kallio & Janhunen, 2003; Mura et al., 2009), which maps to

an L-shell of ~ 1.6 in a centered dipolar model (an L-shell is defined here as the maximum distance a field line extends outward in units of planetary radii). Yet, the Baumgardner et al. (2008) observations show enhancements at somewhat higher latitudes. Precipitation along an L-shell of 2.5 is therefore used here, which better corresponds to the boundary between open and closed field lines in the magnetotail (Slavin et al., 2012). In light of the magnetometer results of Anderson et al. (2011), the magnetic equator is located at 11.5° N planetographic latitude. An L-shell of 2.5 thus intercepts the planet at 40° S and 61° N. To first order, precipitation along these field lines is assumed to impact over Gaussian FWHMs of 30° in latitude.

4.3.4 Impact Vaporization

Enhancements in the lunar Na exosphere have been observed to correlate with intense meteor showers (Smith et al., 1999; Wilson et al., 1999). Meteorite drivers at Mercury may also comprise a measurable fraction of the total sources of the Na exosphere, however the flux of impactors is not well known. Marchi et al. (2005) predicted that the flux of large meteoroids (>13 cm diameter) may be asymmetrical in the morning and evening hemispheres by as much as a factor of 1.5. The impacting flux of smaller (1 mm to 1 cm) grains migrating from the main asteroid belt via Poynting-Robertson drag is several orders of magnitude higher, estimated to produce 75% of the vaporized sodium, with the other 25% owing to impactors 1 to 10 cm in diameter (Cremonese et al., 2005). The contribution of vapor from the impactor to the plume can be neglected to first order, as it comprises only a small fraction of the mass of the regolith vapor produced (Mangano et al., 2007). Unlike desorbed and sputtered sources, vapor is assumed to be ejected approximately isotropically from the point of impact (Killen et al., 2010a). The effect of a large impact on sodium escape rates at Mercury is discussed in Section 5.2.4.

It has been suggested that a small fraction of Na produced during meteor impacts may be in the form of oxides and hydroxides (Berezhnoy & Klumov, 2008). The photolysis lifetimes of these molecules are short on Mercury compared to the ballistic time of flight to impact the surface (Self & Plane, 2002). Atomic Na from photo-decomposed molecules may retain an energy of the order of the molecular bond strength, resulting in a trace but energetic (1 to 2 eV) population. This energetic population is ignored in models of Mercury's exosphere to date, including my own, but is mentioned for completeness. Excess photolysis energy depends on the vibrational and rotational states of the molecule and the photon wavelength; division of this energy between kinetic and potential energies in the atom is not well defined (Jhon & Dahler, 1978). As such, inclusion of the photolytic products of molecular Na is more rigorous than other source mechanisms.

Sodium vaporized by micro-meteoroid impacts on Mercury is likely to be thermalized, as the gas is locally collisional in the fireball. The average temperature of the ejecta depends on the nature of the impact. Killen et al. (2010a) suggested a temperature of only 1000 K from the Lunar Crater Observation and Sensing Satellite (LCROSS) impact plume. However, micro-meteoroids impact Mercury with more than 10 times the velocity at which LCROSS hit the Moon (Cintala, 1992). Berezhnoy & Klumov (2008) suggest 2500 K, Leblanc & Johnson (2010) assume 3000 K, Wurz et al. (2010) assume 4000 K, and Burger et al. (2010) simulate 2000 and 5000 K. Both 3000 and 5000 K thermalized sources were simulated in Schmidt et al. (2012), shown in Fig. 4.5 as the blue solid and dashed lines, respectively.

My latest work, assumes micro-meteor vaporized Na has a thermal energy of 2500 K. Killen et al. (2001) proposed a source dependence with solar range as $4.7 \times 10^{22} \times R^{-1.9}$ atoms s^{-1} , which I increased by a factor of 1.1 to 2 to reflect recent estimates of the Na surface concentration (Evans et al., 2013). Meteor flux is presumed to have

north-south symmetry over Mercury's surface, although asymmetries in the trailing and leading hemispheres have been proposed (e.g., Marchi et al., 2005).

4.3.5 Conclusion

An up to date model of the Mercury exosphere should be frequently revised in the presence of in situ measurements. For example, the inclusion of non-uniform surface concentrations based on Evans et al. (2013) improves the model's capability to simulate the bound exosphere. Modifications also stem from refinements of estimated parameters based on older literature. In my initial Schmidt et al. (2012) study, the derived source rates are not limited by the finite supply of Na atoms to the surface. Upon adopting new energy distributions in Fig. 4.6, I have since added a limit on sources based on the diffusion limited supply rate Killen et al. (2004). While many important parameters still remain poorly constrained at Mercury, modeling the most plausible cases for each can still advance the field.

Chapter 5

Model-Data Comparisons

5.1 Introduction

In the following section, 5.2, the Monte Carlo model is applied to the first two years of wide-field coronagraph data. I determine the seasonal atmospheric escape for each exospheric source applying the energies distributions shown in Fig. 4.5. I then explore the detection limits on variability in the escaping atmosphere due to space weather events and large meteor impacts. Following this study, the model's source characteristics are refined based on my own fits to the Yakshinskiy & Madey (2005) data and new information from the MESSENGER spacecraft, as discussed in Section 4.3. The refined Monte Carlo model is used to simulate the observations of north-south asymmetries in the tail by Potter & Killen (2008) in Section 5.3, using the constraint of simultaneous measurements of the Na exosphere above Mercury's disk (Baumgardner et al., 2008).

5.2 Modeling the Wide-field Coronagraph Data: New Constraints on Exospheric Processes

5.2.1 Constraints on Source Mechanisms

Using the characteristics modeled for meteoritic, photo-desorbed and sputtered source processes, each is capable of ejecting sodium that escapes the planet's gravity into the tail. In this section, the release rate of each source mechanism into the

exosphere is adjusted so that escaping sodium produces enough D line emission to match the peak brightness found in the tail. The emission falloff with distance from the planet is accurately reproduced by time-integrated ionization and acceleration effects in the model, so that once the best fit value is obtained, a peak brightness match at all distances from the planet is inherent. To gauge the variability in the data set, source rates for each surface ejection mechanism are fit to each observation. I then discuss the viability of each source rate so determined, the required variability in rates over the data set, and apply empirical and theoretical constraints. Section 5.2.2. investigates the tail width and the shape of the cross-tail profile produced by the six different energy distributions (shown in Fig. 4.5) commonly applied at Mercury.

Global source rates in the range of $\sim 10^{23}$ to $\sim 10^{25}$ atoms s^{-1} are able to match all observations seen in my Schmidt et al. (2010) study. In Figure 5.1, the first high-resolution wide-field coronagraph data of 18 May 2008 (panel A) is chosen as the test case for comparison with several simulations using a single source process as the model input. The 6 arcminute occulting mask in panel A blocks Mercury's bright disk, and the plate scale of the wide-field coronagraph has been matched in the model for convenience of comparisons. Panel B shows a 3000 K spatially isotropic Maxwellian source representing a micro-meteoroid vaporization rate of 2.7×10^{24} atoms s^{-1} . Nearly half this value, a 5000 K source rate of 1.3×10^{24} atoms s^{-1} , also matched the peak brightness but is omitted from the figure as the result looks quite similar to panel B. Total source rates for both slow and fast ion sputtering distributions (curves (3) and (4) in Fig. 4.5) are restricted to 1.3×10^{23} atoms s^{-1} totally, as shown in panels C and D, respectively, and at least a factor of 4 increase from these values is needed to match the observation. Panel E is a slow PSD source at 1500 K, limited to 1.0×10^{25} atoms s^{-1} . The best match for fast PSD requires 3.0×10^{24} atoms s^{-1} , as shown in panel F.

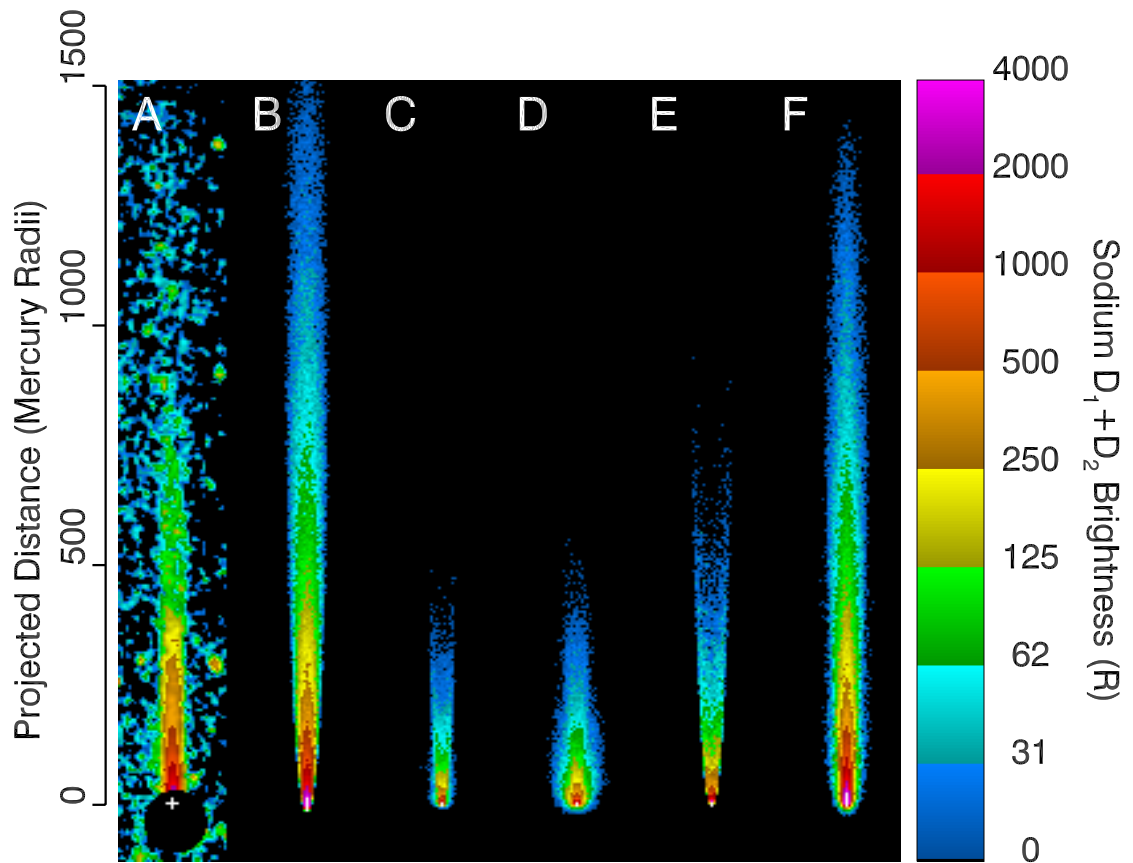


Figure 5.1 A comparison of recorded brightness on UT 18 May 2008 with simulations using a single source process (panel A). A 3000 K spatially isotropic Maxwellian source representing micrometeoroid vaporization rate of $2.7 \times 10^{24} \text{ atoms s}^{-1}$ (panel B). The sputtered distribution of Eq. 4.8 after Wiens et al. (1997), ejected from cusp regions at $\pm 70^\circ$ latitude (panel C). Source rates are limited to $1.3 \times 10^{23} \text{ atoms s}^{-1}$. Same as C but with a sputtered distribution used in the study by Wurz et al. (2010) (panel D). A PSD source at 1500 K limited to $1 \times 10^{25} \text{ atoms s}^{-1}$ (panel E). A fast PSD source distribution corresponding to the dashed green curve (6) in Fig. 4.5 (panel F).

Three of the six sources I simulate require a release rate that exceeds realistic limitations, suggesting these may be dismissed as the dominant source of high-energy sodium. On the basis of combined estimates of ion-precipitation rates, Na soil concentration, and the effective yield per ion (Killen et al., 2007; Wurz et al., 2010; Killen et al., 2004), an upper limit of 1.3×10^{24} atoms s^{-1} is placed on the global source rate sputtered by ions. Source rates required to match the tail brightness for both energy distributions of solar wind sputtering exceed this upper limit. This effectively eliminates distributions (3) and (4) in Figure 4.5 as the dominant source of Na escape, as neither is an adequate source for either sputtered energy distribution to produce the observed escape. In addition to the sputtered sources, the PSD source rate at 1500 K, needed to match the tail brightness, exceeds an observational constraint. Upon repeated measurements by Potter et al. (2007), the average dayside column abundance found (in which they applied the requisite phase angle and scattering corrections) is approximately 5×10^{10} atoms cm^2 for the orbital phase of the 18 May 2008 coronagraph data. Matching this, abundance limits slow PSD source rates to no more than $\sim 1 \times 10^{25}$ atoms/s. This source rate would account for only $\sim 35\%$ of the observed tail brightness, effectively eliminating distribution (5) in Fig. 4.5 as the dominant source of Na escape, although it should be noted that the modeled column density depends heavily on the sticking characteristics. Required upper limits are thus simulated in panels C, D, and E of Fig. 5.1.

Meteoritic and fast PSD source rates reproducing the measured brightness in panel A do not exceed observational or firm theoretical constraints. For fast PSD, a $\sim 10^{25}$ atoms s^{-1} limit is significantly higher than the rates needed to match all my wide-field observations, so that only slow PSD is constrained by the Potter et al. (2007) dayside abundance estimates. In all cases, the global supply of sodium to the surface from above (mostly reabsorbed from the exosphere) and from below (using

the diffusion limit proposed by Killen et al. (2004) is sufficient to allow the considered desorption rates without depleting the regolith. Impact vaporization and sputtered source rates are also not limited by the average dayside abundance. Simulations of these more energetic mechanisms reproduce the gravitational escape rates, while staying well below the expected dayside column abundance. The source rate of vaporized sodium caused by micro-meteoroids was not constrained, as the impacting flux at Mercury is highly model dependent (e.g., Borin et al., 2010).

Upper limits for solar wind sputtered sources are still at least a factor of four too low to account for the observed brightness in the tail. In order to meet the requisite escape flux observed, a 1500 K population ejected by PSD would exceed the disk-averaged brightness measurements by a factor of 2. PSD still may be the dominant source of escaping sodium, however, if the distribution of initial ejection velocities has a tail at high energies. Gravitational escape of a thermalized, globally distributed source attributed to impact vapor doubled from 3000 to 5000 K. The gravitational escape because of impact vaporization at 3000 K was comparable to that of PSD if a high-energy tail in the distribution of ejection velocities is extrapolated.

Table 5.1 quantifies the escape rates required for the observed brightness during the 18 May 2008 wide-field observation and compares upper limits on the globally integrated flux for several source types to the flux required to match the escape derived with my 1-dimensional model, as was shown in Fig. 3.10. The first column indicates the source type and energy distribution assigned to the atoms upon initial release in the model. The constraints on release rates applied in Fig. 5.1 are given in the second column. Notice that for both sputtered sources simulated, these imposed upper limits are at most $\sim 25\%$ of that needed to reproduce the peak brightness observed in the tail, given in the third column. The last column is the percent deviation in the source needed to match both the 18 May 2008 escape rates and the recorded maximum

Table 5.1. Global Source Rates of Sodium Required to Simulate Observed Escape

Mechanism (See Distribution in Fig. 4.5)	Upper Limit Source Rate (atoms/s)	Source Rate Matching Tail Brightness on 18 May 2008 (atoms/s)	Required Increase From 18 May 2008 to 12 Nov 2007 Measurements (%)
MIV: (1) Slow	Unconstrained	2.72×10^{24}	71
(2) Fast	Unconstrained	1.32×10^{24}	109
IS: (3) Slow	1.3×10^{23a}	9.60×10^{23}	156
(4) Fast	1.3×10^{23a}	5.14×10^{23}	170
PSD: (5) Slow	9.87×10^{24b}	2.30×10^{25}	56
(6) Fast	1.02×10^{25b}	2.96×10^{24}	146

^aExceeds total expected source flux, given upper limits on surface concentration, particle precipitation, and yield.

^bSimulation result exceeds the average dayside abundance determined by Potter et al. (2007).

escape on 12 November 2007, used as a proxy for the variability required to match the escape rates over the first two years of the wide-field data set. An inverse square law dependence would account for a 45% increase in the source between these two dates, and an uncertainty of $\sim 20\%$ is inherent in the measurements owing to calibration and terrestrial Na background noise.

5.2.2 Constraints on Energetic Processes

The cross-tail D-line brightness profile is shown in Figure 5.2 for wide-field images taken on UT 18 May 2008 at various distances from the planet. The point spread function (2.6 pixels FWHM), as determined from background stars in the coronagraph field, has been deconvolved from the tail width assuming both the cross-tail and PSF profiles are Gaussian. The resulting estimate of the physical width of the distant sodium tail is shown by the dotted black line.

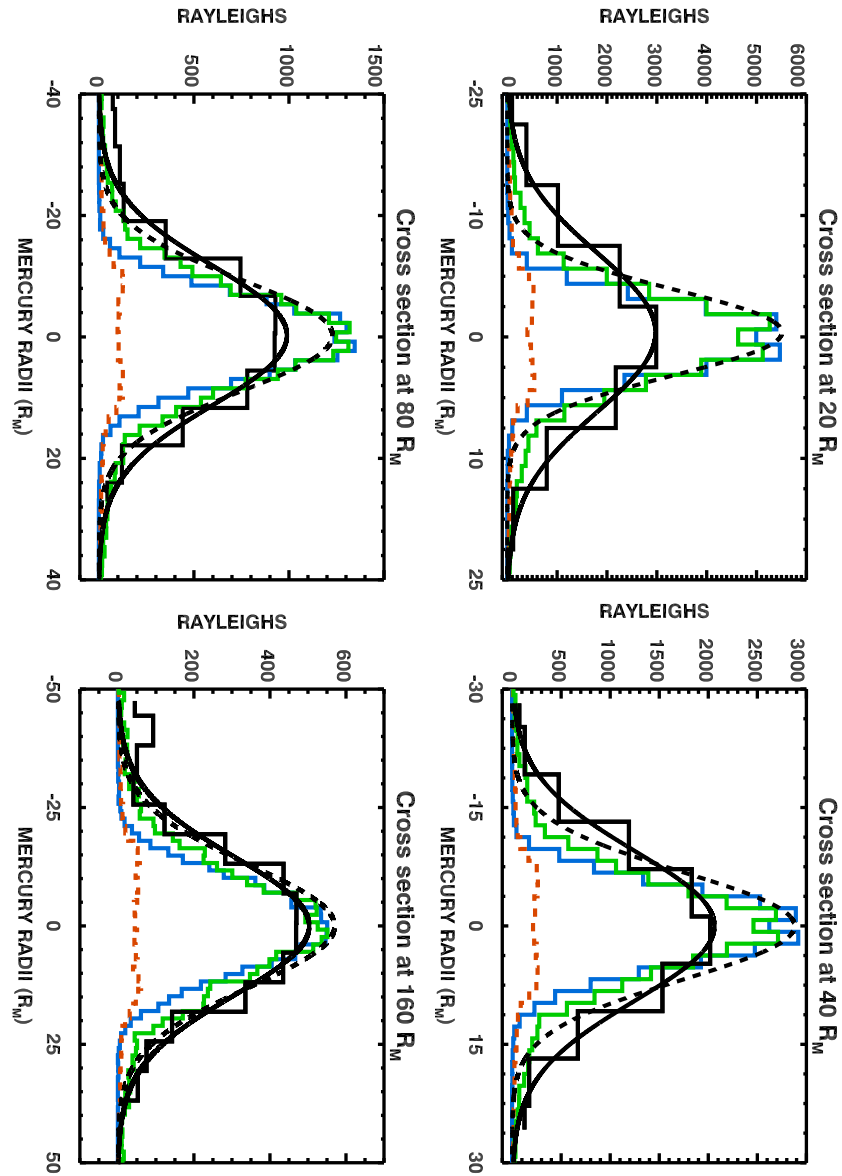


Figure 5.2 At four chosen distances, a comparison of the cross-tail brightness profiles recorded on UT 18 May 2008 (**Black Histogram**) with several simulated source distributions. Note the change in brightness scale (left axis) and width scale (bottom axis) with distance. **Black:** A Gaussian fit to the data. **Dashed Black:** A Gaussian fit to the data after removal of the 2.6 ± 0.2 pixel FWHM instrumental point spread function. **Blue:** A 5000 K globally isotropic source at 1.3×10^{24} atoms s^{-1} . **Green:** A high-energy PSD source of 2.96×10^{24} atoms s^{-1} with an energy cutoff of 10 eV as used in the studies by Johnson et al. (2002) and Wurz et al. (2010). **Dashed Orange:** A sputtered source limited to 1.3×10^{23} atoms s^{-1} .

Considerable differences in the energy distributions of Figure 4.5 result in only subtle differences in the simulated tail widths, especially for low α . If the thermal accommodation, α , is as high as 0.62 as Hunten et al. (1988) proposed, then the tail width of simulations for all Maxwellian sources is narrower than that observed. The dashed blue profile in Figure 5.2 is that of a globally isotropic source thermalized at 5000 K, characteristic of impacting micro-meteors. The contribution of high-energy sputtered sources is unable to account for the observed width, as estimates of the total yield are far too small to match observed brightness. The orange profile shows the maximum allowed contribution of a sputtered source (1.3×10^{23}), with an energy distribution of Eq. 4.8 as fit by Wiens et al. (1997). The enhanced brightness at the polar lobes from sodium ejected at $\pm 70^\circ$ latitude cusp regions is visible in the simulations, even at distances greater than 50 planetary radii. The very high-energy distribution for sputtered atoms used in the studies by Wurz et al. (2010) and Lammer et al. (2003) produces a profile that well exceeds the observed width if sputtering is the dominant source of escape. At the $\sim 3 R_M$ down-tail range observed by Potter & Killen (2008) during a similar orbital phase, desorbed and vaporized sources approximately match their widths of $\sim 10,000$ km FWHM, while the tail width from both sputtered sources is $\sim 15,000$ km. The green dashed line shows the result of an energy distribution similar to that used by Wurz et al. (2010) for PSD. I find that a ~ 10 eV upper limit to the energy of a desorbed source best matches the cross-tail width in the wide-field data, while these authors chose 20 eV. At this orbital phase, the escape flux using my modification is nearly 15% less than that of a 20 eV cutoff.

5.2.3 Seasonal Effects

Seasonal Effects on the Observable Na Tail

Mercury's Na atmosphere exhibits seasonal variability in brightness and column density (Leblanc & Johnson, 2010). Unlike the familiar seasons driven by Earth's

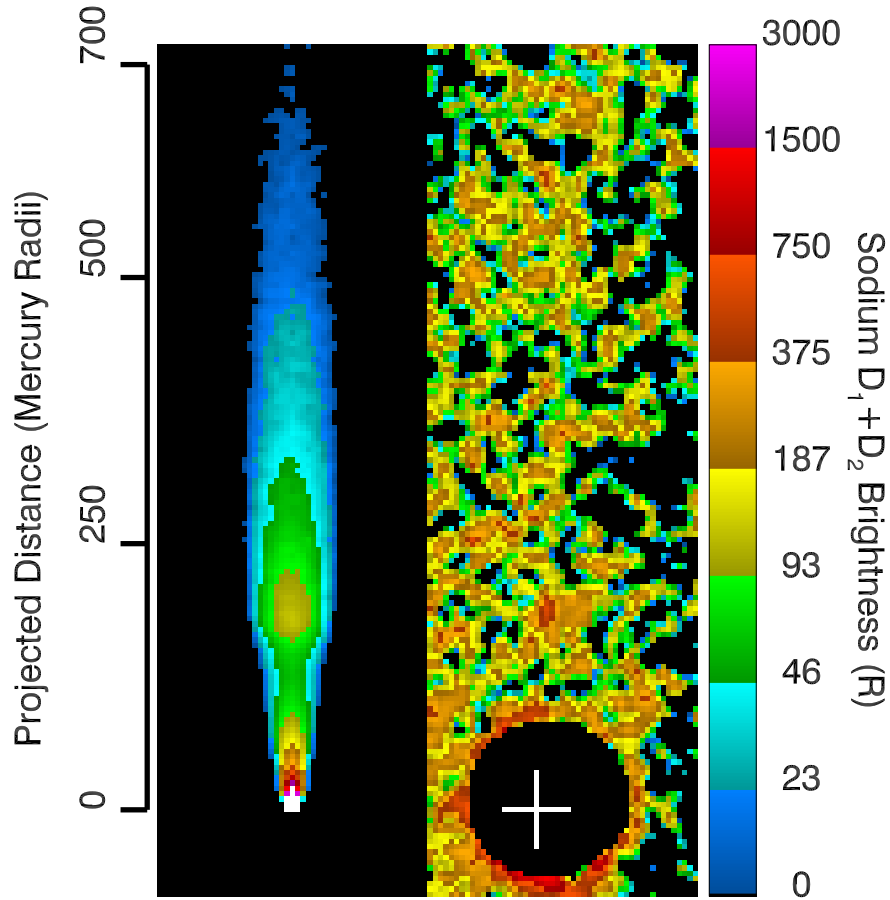


Figure 5.3 (left) Comparison of simulation and (right) data for a tail "non-detection" case. The simulation shows a steady state global release of 2.7×10^{24} atoms s^{-1} at 3000 K. Noise levels for the UT 6 July 2008 measurement are high because of D line contamination in the terrestrial mesosphere during this observation, taken at a low elevation angle.

tilted spin axis, seasons in Mercury's atmosphere result from the planet's rotational motion, and its distance and velocity relative to the Sun. The escaping portion of the atmosphere varies with orbital longitude, as solar radiation pressure is a function of the Sun's distance and relative velocity. To calculate the escaping fraction of Mercury's sodium atmosphere, the model's source is turned off and particle motions are integrated over several photo-ionization lifetimes (at least 1 day). The population remaining aloft typically moves many hundreds of planetary radii in this time, where radiative forces prevail over gravity by orders of magnitude. Such particles are labeled

as escaping if their distance from the planet then exceeds a set boundary, chosen to be $15 R_M$.

The escaping Na from each energy distribution population varies uniquely as the threshold for escape changes with orbital motion, and so wide-field observations of sodium escape during times of lesser radiation pressure can also be used to characterize high-energy tails in the source population. My observations during the M1 MESSENGER flyby (14 January 2008), as well as on 6 July 2008, showed no sodium tail at 120 and 90 R_M , respectively. Both observations were made with Mercury in the same portion of its orbit, at true anomaly angles of 287° and 275° , respectively. During this orbital phase, atoms traveling anti-sunward are Doppler shifted into the Fraunhofer D line absorption well, where scattering is only 5% of the continuum. As such, escape rates are high because of strong initial radiation pressure. However, most atoms are photo-ionized close to the planet before a bright distant tail can form. Fig. 5.3 illustrates this effect, again showing a steady state global release of 2.7×10^{24} atoms s^{-1} at 3000 K, identical to panel B of Figure 5.1, except for the case of the UT 6 July 2008 data at a true anomaly of 275° . Note the change of axis scale in comparison to Fig. 5.1. At down-tail distances of $\sim 175 R_M$, the remaining neutral sodium produces a small, isolated feature because of increased scattering as the gas emerges from the absorption well. The feature's 170 R peak simulated brightness is comparable to the $\sim 125 R$ standard deviation in the background noise during this observation. After subtraction of the bright terrestrial background, noise levels in the data are high and residual artifacts persist, especially surrounding the coronagraph mask. Subsequent observations at higher-elevation angles are expected to better quantify this feature. Yet I note that the brightness pattern observed in the anti-sunward direction has (for an observation previously considered a non-detection of the tail) a possible local

maximum at the distance range predicted by our model, and this feature should be apparent under more favorable observing conditions.

Seasonal Control Over Na Escape Rates

As the radiation pressure affecting the sodium exosphere changes with Mercury's eccentric orbital motion, the escape of the bound atmosphere varies differently for each source process, depending on its velocity distribution and source region on the surface. For a constant source, the column density averaged over the dayside disk was found to vary with radiation pressure. A 1500 K PSD source displayed a column density reduction by $\sim 1/3$ from minimum to maximum radiation pressure, and densities by meteoritic sources were reduced by as much as one half. Table 5.2 shows the fraction of particles escaping as a function of orbital phase for each source described in Figure 4.5. This escaping percentage is simply the number of particles that escape divided by total the number of particles released into the atmosphere. Those particles further than $15 R_M$ from the planet, after 24 hours of integration during which particle release is turned off, are considered to have escaped. Calculated radiation acceleration is $\sim 7\%$ smaller than given in my previous study (Schmidt et al., 2010) because of an improved solar flux model. A thermal accommodation coefficient of 0.62 was used universally for these estimates (Hunten et al., 1988). In each case, however, the smooth surface bouncing conditions described in Section 4.2.2 increased escape rates by an average of only 2%, compared with model runs where all atoms stuck to the surface upon impact, and less still if the porosity of the regolith is accounted for (Cassidy & Johnson, 2005).

There are several items to note in Table 5.2. Near apoherm, escape of Maxwellian distributions becomes negligible, and associated processes may allow sodium to replenish the upper surface layers during much of the Mercury year. High-energy sources, especially ion sputtering, naturally exhibit very little variability in escape over the Mercury year. Less energetic distributions, notably 1500 K PSD and 3000 K impact

Table 5.2. Percentage of Na Ejected into the Atmosphere that Escaped by Source¹ and Date²

UT Date	TAA (°)	a_{rad} (cm/s ²)	Slow PSD	Fast PSD	Slow IS	Fast IS	Slow MIV	Fast MIV
31 May 2007	114	126	2.2	15.8	48.5	89.1	16.5	33.7
2 Jun 2007	121	114	1.9	15.3	47.4	88.9	15.1	31.5
3 Jun 2007	124	107	1.7	15.1	46.3	88.8	14.4	30.7
12 Nov 2007 ^a	69	168	3.5	17.3	51.2	90.8	22.2	37.9
15 Jan 2008	287	170	2.2	15.3	47.7	90.5	16.1	36.8
6 Jul 2008	275	165	2.1	15.3	46.8	89.1	16.4	32.9
Apoherm ^b	180	11	0.000	7.3	25.2	76.0	0.7	4.2

¹Energy distributions attributed to each are shown in Fig. 4.5.

²For the 2007-2008 observations of Schmidt et al. (2010).

^aHighest escape rates during Mercury's orbit.

^bIncluded as a reference for minimum escape.

vaporization, exhibit the largest degree of seasonal variability in escape, and these, though still somewhat less, better approximate the variation seen in the Schmidt et al. (2010) data set, in which escape fluxes spanned 4.6 to 12.6×10^{23} atoms s^{-1} . Also note that, for constant supply, escape rates can significantly differ between orbital positions having the same radiation pressure but opposite true anomaly. This effect arises from the particle’s motion being accelerated either into or out of the Fraunhofer D line absorption well, depending on the sign of Mercury’s heliocentric velocity.

Creating Table 5.2 inherently required a specified spatial distribution of surface processes. Ejection rates were chosen to vary only with solar zenith angle for PSD (photon-limited), and sputtering occurs with north-south symmetry only in regions near $\pm 70^\circ$ latitudes. To examine localized enhancements in PSD and space weather effects on the footprint of the cusp, I also varied the ejection locations on Mercury’s surface. The escaping fraction of desorbed and ion-sputtered sodium was found to vary by ejection location on the planet’s surface, most substantially during maximum radiation pressure. Compared with the subsolar point at this time, fast PSD escape rates were 92% and 150% higher where enhancements have been proposed, near $\pm 70^\circ$ latitudes, and at the dawn terminator, respectively (e.g., Mura et al., 2009). Approximately 10% of slow PSD atoms escape from these regions, while escape at the sub-solar region is negligible. Escape of sputtered sodium is found to decrease by 37% and 10%, for slow and fast sputtering, respectively, if the cusp footprint is moved all the way to the equator during extreme loading of the magnetosphere (Slavin et al., 2010b).

5.2.4 Constraints on Potential Short-Term Source Variability

Short-term variability may be visible in the ~ 15 hour time history captured in the observed tail length using wide-field imaging techniques. Source rates of both sputtered sodium and impact vaporization are expected to vary on short timescales. Both

processes have very different morphologies because of the regions on Mercury's surface where each is likely to occur and the duration of the variability in each source. I now investigate two possible scenarios: (1) an extreme space weather event in which the magnetopause is pushed to Mercury's surface and (2) a large meteor impact centered on Mercury's leading hemisphere.

Detection of Space Weather Events

As I have determined the relative contribution of sputtered sodium to be low, transient events must be quite intense to produce any observable increase in the tail brightness. Even if a fast distribution of energies is assumed, where nearly all sputtered particles escape the planet, generous upper limits on typical supply rates are shown here to be only $\sim 25\%$ of those needed to match the observed escape. In addition, the cusp regions can shift equatorward (Slavin et al., 2010b), where radiation pressure pushes more atoms to bounce off the dayside surface, and thermal accommodation decreases the rate of sodium escape. Although induction currents will oppose compression of the magnetosphere, it is not impossible that the magnetopause may occasionally be forced down to the planet's surface (Russell et al., 1988; Fujimoto et al., 2007).

In the following example, I consider a very intense sputtering event: the extreme condition in which the whole dayside magnetosphere is exposed to the solar wind. An average source rate of $3.5 \times 10^6 \text{ atoms s}^{-1} \text{ cm}^2$ is sputtered into the exosphere, with ejection locations distributed by solar zenith angle. This represents an order of magnitude increase in the sputtering rate from my estimated upper limit, making the transient supply of sodium sputtered into the exosphere $1.3 \times 10^{24} \text{ atoms s}^{-1}$. The ejection energy distribution of Wiens et al. (1997) is applied to the sputtered atoms. A background source is chosen to be a meteoritic Na vapor at 3000 K, fixed to $1.2 \times 10^{24} \text{ atoms s}^{-1}$, and a fast PSD source at $1.1 \times 10^{24} \text{ atoms s}^{-1}$. The pulse in sputtering

is input as a step function 1 hour in width, and Figure 5.4 shows how the tail might look 6 hours after the event onset. While such an event might be unlikely, such a pulse would approximately double the sodium brightness at $100 R_M$, making it observable via wide-field imaging techniques.

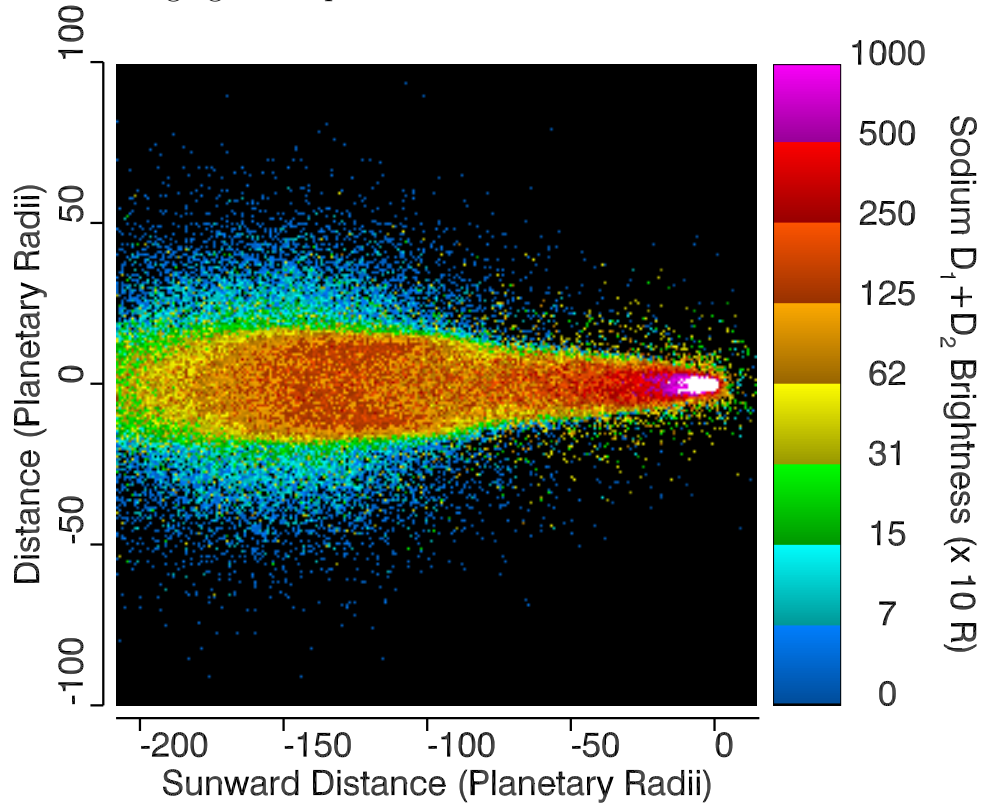


Figure 5.4 The result of an extreme sputtering event 1 hour in duration, after 5 hours of acceleration down the tail. An order of magnitude increase from the upper limit for typical solar wind conditions results in double the brightness of the background escape because of PSD and meteoroid impact vaporization.

Detection of Large Meteor Impacts

Mangano et al. (2007) showed that sodium produced by large impactors would be difficult to detect above the dayside background emission by the PHEBUS and SERENA instruments onboard the BepiColombo orbiter. If the exosphere is predominantly desorbed, the ejecta from a large impact are more energetic than background

sources. The plume of sodium D-line emission may be more easily visible further down-tail as more of it escapes relative to the lesser energetic background sources. To investigate this possibility, I determine the ejection rate from a point source needed to vaporize a plume with peak brightness at least double that of the background at $100 R_M$ down-tail, where signal to noise is optimum with wide-field coronagraph techniques. The nature and frequency of impacts vaporizing enough sodium to meet the detection limit is discussed in this section.

Again, choosing the 18 May 2008 observation as a test case, the detection of a large meteor impact in the tail becomes possible when approximately 1.6×10^{27} Na atoms (60 kg) or more are vaporized in the fireball. Figure 5.5 shows a 5×10^{27} atom plume, which is comparable to estimates of the total content of the exosphere at this orbital phase (Leblanc & Johnson, 2003). The simulation assumes that a 5000 K velocity distribution is ejected from a point centered in the leading hemisphere near the dawn terminator. Models of the LCROSS lunar impact have shown the Na plume probably expanded isotropically (Killen et al., 2010a), as I will assume here. A simple dependence on the cosine of the surface normal, as used for desorption and sputtering (Leblanc & Johnson, 2003), would increase the escape by 10 to 15 percent. To portray such a dynamical scenario, note that each panel in Figure 5.5 has a different spatial and brightness scale. A background source to the exosphere again consists of a micrometeoritic source of Na vapor at 3000 K, fixed at 1.2×10^{24} atoms s^{-1} , a fast PSD source at 1.1×10^{24} atoms s^{-1} , now with a fast sputtered source fixed at 5.0×10^{22} atoms s^{-1} . The panels in Figure 5.5 show model results of the plume 5 min, 1 hour, 2 hours, and 6 hours after impact.

Models suggest that large meteor impacts may occur with slightly greater frequency on Mercury's morning hemisphere, i.e., the hemisphere facing the upwind direction (Marchi et al., 2005). For impact sites centered near dawn as in Figure 5.5,

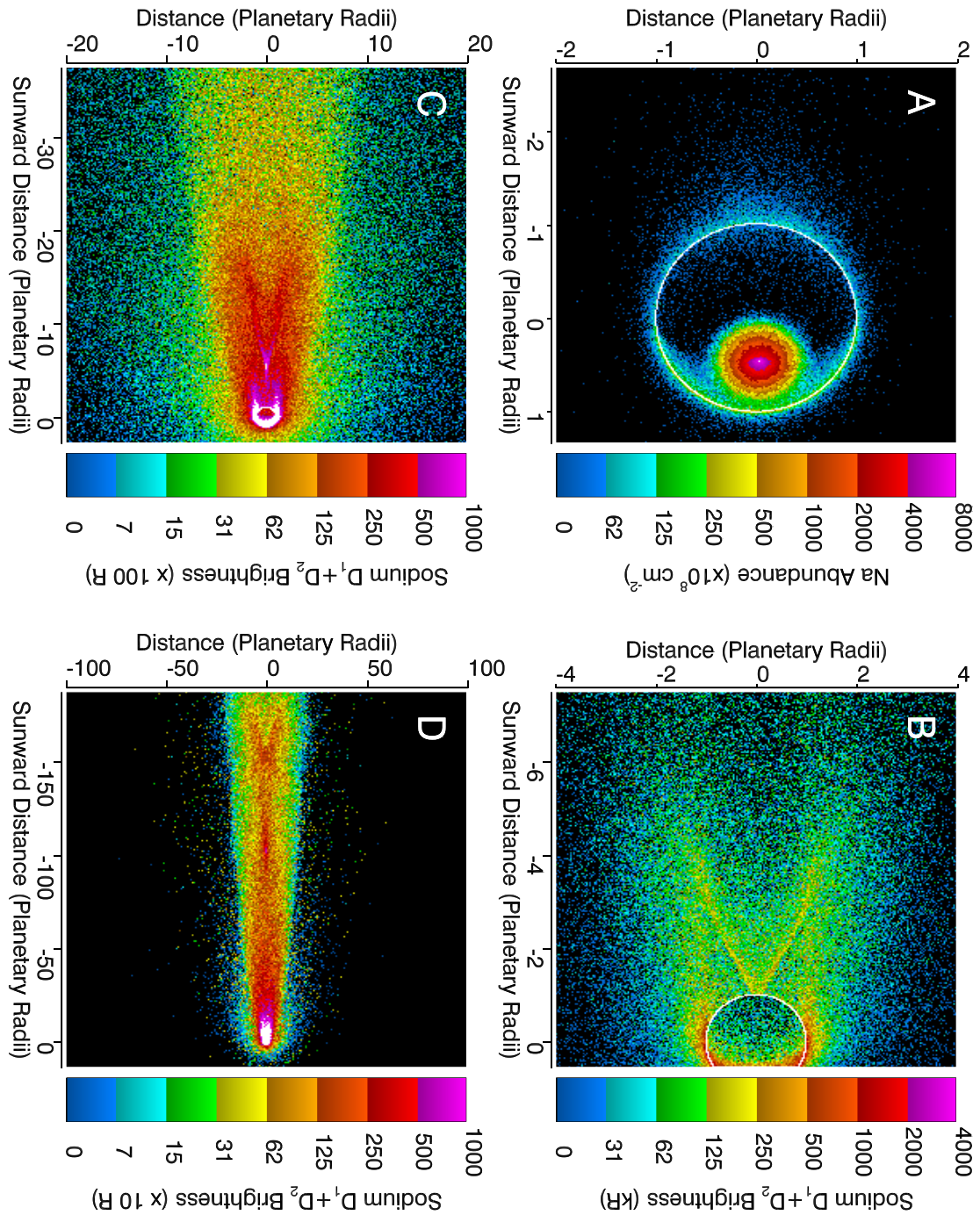


Figure 5.5 Propagation of a 200 kg sodium plume lofted from the regolith by a very large impact: (A) 5 min after impact, note the result is given as column abundance, as the D2 line is optically thick; (B) 1 hour after impact; (C) 2 hours after impact; and (D) 6 hours after impact.

much of the plume is guided across the nightside by gravity before re-emerging from the planet's shadow and making its way down-tail. During the transit to the nightside, energetic portions of the plume experience a longer time of flight and hence more radiation pressure while sunlit, effectively dispersing the vapor cloud over a large volume. This is the cause of the extended vapor cloud with a bifurcation seen in Figure 5.5 panel B, which grows to span more than $100 R_M$ in length 6 hours after the impact. The plume from an impact occurring near the sub-solar point, while still diffuse, remains more cohesive in structure down-tail. However, radiation pressure forces more of the ejecta to reimpact the dayside surface. For $\alpha = 0.62$ (Hunten et al., 1988), only $\sim 14\%$ of the plume escapes the sub-solar point, compared with $\sim 32\%$ near the terminator. In addition, a plume from a dayside-centered impact point makes a longer anti-sunward trip, allowing greater photoionization and thus canceling any gains toward potential visibility to wide-field observing methods.

My simulations suggest that only very large meteoroids (>30 cm radius) would be detectable in observations of the distant sodium tail, depending on the location of the impact on the surface. At 35 km s^{-1} , such impacts can vaporize nearly 60 kg of sodium from the surface regolith, if I extrapolate the equations of Cintala (1992) for a diabase type impactor, a surface temperature of 400 K, and a surface concentration of 0.0134 (Wurz et al., 2010). Transient processes injecting atoms into the Na tail must occur on very short timescales in order to produce distinct heterogeneity in the brightness profile. For this reason, short-term, hourly timescale pulses in ion-precipitation rates may be less likely to produce an observable brightness variation down-tail than the instantaneously released plumes that are created by occasional large meteoroids. Only for the extreme precipitation ($\sim 10^{27}$ ions/s) during solar energetic particle events does the escape rate of sputtered sodium become comparable to the rate of escape that I derive (Leblanc et al., 2003). Short-term increases in particle precipitation can cause

subsequent increases in Na desorption, as chemical alteration of the regolith may act as a catalyst for desorption processes, which are limited by diffusion in the soil (Potter, 1995; Killen et al., 2004). I am therefore not able to rule out short-term variations in the escaping exosphere driven by ion precipitation.

Observations showing localized hot spots of sodium D line emission, such as the near-disk flanks in the tail observation by Potter et al. (2002) and the polar lobes in the high-resolution adaptive optics image used in the study by Baumgardner et al. (2008), could not be replicated with the upper limit source rates for particle sputtering. Localized enhancements in desorption from surface alteration caused by particle precipitation may therefore be responsible (e.g., Potter, 1995). Also, the dawn-side sodium enhancements observed by Sprague (1992) and Schleicher et al. (2004) are difficult to explain without a more advanced surface composition model in which sodium preferentially condenses on the cold nightside. Accurately simulating such features involves a more in-depth simulation of the systematic redistribution of sodium over the planet and chemical alteration of the surface by charged particle bombardment, in which both chemically and physically absorbed Na is considered (Hunten et al., 1988). While such an effort is not pertinent to characterizing the sodium escape in this study, a surface composition and chemical alteration model is considered for future studies.

5.3 Modeling of Simultaneous Ground-Based Data

Ground-based observations and MESSENGER's first flyby show persistent asymmetries in Mercury's neutral sodium tail, with the brightest emission often seen in the northern lobe (Potter & Killen, 2008; Baumgardner et al., 2008; McClintock et al., 2008). This feature may be associated with the recent finding that the magnetic dipole moment is offset from the planet's center by $0.2 R_M$ to the north, while approximately

aligned with the spin axis (Anderson et al., 2011). Such a configuration produces an asymmetry in the magnetospheric cusp whereby more plasma has direct access to the planet's southern hemisphere than the north (Winslow et al., 2012). In this section, I examine the effects of asymmetric precipitation on the sodium tail by simulating the near simultaneous observations of Potter & Killen (2008) and (Baumgardner et al., 2008) taken on 8 June 2006 and 11 June 2006.

Observationally, a clear distinction can be made between asymmetric source types by examining the neutral sodium tail escaping Mercury. Desorbed atoms leave the surface at low energies so that gravity directs their trajectories back to the surface, and very few escape. Ballistic trajectories of sputtered atoms experience far less gravitational influence and largely escape into the tail during maximum radiation pressure. Smyth & Marconi (1995) demonstrated very different migration effects in the tail depending on the energy imparted to Na atoms. In particular, these authors showed that atoms accelerated by radiation pressure to just above the gravitational escape threshold will migrate to the opposite hemisphere before escaping down-tail (see their Figure 7). The practical implications of these unique trajectories have only recently become pertinent, as sodium sources are now expected to be asymmetric given the magnetic field offset. Measurements of Mercury's sodium escape hence provide valuable constraints for characterizing the sources and physical processes sustaining the exosphere and their energies.

Studies concerning the spatial distribution of sodium sources at Mercury have a long history (e.g., Sprague, 1992; Potter et al., 2006). In this section, regional sources of sodium are examined, as prompted by the recently observed asymmetries in the escaping tail (Potter & Killen, 2008; Baumgardner et al., 2008; McClintock et al., 2008) and offset in the magnetic field (Anderson et al., 2011). Modeled emissions are compared with the tail measurements of Potter & Killen (2008), using exospheric

sources coupled to estimates of particle precipitation in the magnetosphere. Observations one and three nights prior by Baumgardner et al. (2008) confirm the persistence of the northern tail enhancement in the Potter & Killen (2008) dataset, and depict the exospheric structure above Mercury’s disk at this time.

This section uses the Monte Carlo sodium exosphere model to investigate if ion sputtering and PSD could produce north-south asymmetries in the Na tail by applying the latest information from the MESSENGER spacecraft. Precipitation rates to the surface and the location of the magnetic cusp footprints are input based on an average of the magnetic pressure deficit measured with the on-board magnetometer (Winslow et al., 2012). The abundance, f_{Na} , is assumed to vary with the maximum surface temperature as $0.056 \times T_{max}^{-0.345}$, based on MESSENGER GRS data (Evans et al., 2012, 2013). The ejection rates of all exosphere sources are weighted by this concentration. Surface temperatures are calculated as described in Section 4.2.2 resulting in a small dawn-dusk asymmetry in the surface interactions due to the thermal inertia of the lithosphere.). At any given latitude, the variation in f_{Na} is less than $\sim 10\%$. Exospheric Na re-impacting the surface has a sticking probability that is temperature dependent, approaching unity at 100K and 0.1 at the sub-solar point based on a fit to the Yakshinskiy & Madey (2005) measurements. The thermal accommodation of atoms bouncing off the surface is treated as a free parameter.

5.3.1 Constraints on North-South Asymmetries

All sources show north-south migration for the majority of the particles escaping. Figure 5.6 gives results for several scenarios that relate to the asymmetries Potter & Killen (2008) observed in the sodium tail. Panel A contains their observations made on UT 12 June 2006. Panels B-D display results of the exosphere model in which source rates are scaled to match the peak observed brightness of 130 kR at 10 arcsec down-tail. Each was convolved with a 2D Gaussian kernel of 1.9 arcseconds FWHM

to compensate for the atmospheric seeing estimated by Potter & Killen (2008). An escape rate of $\sim 6 \times 10^{23}$ Na atoms s^{-1} is determined for this measurement, in fair agreement with both the $4.9 \pm 1.1 \times 10^{23}$ atoms s^{-1} quoted by Potter & Killen (2008) and the wide-field observations at this true anomaly angle by Schmidt et al. (2010).

Simulated cross-tail profiles in panel B-D include PSD, micro-meteor impact vaporization and sputtering as source types, each with a different mixture. The dashed line in panel B shows results of sputtered sources at the average locations of the cusp footprints that are scaled to 4.1×10^{24} atoms s^{-1} . In addition, nominal rates for photon-limited PSD and meteor impacts, 2.4×10^{25} atoms s^{-1} and 1.2×10^{23} atoms s^{-1} , respectively, are applied as described in the previous section. However, an influx of 5×10^{24} Na ions s^{-1} (Winslow et al., 2012) precipitating onto a .8% Na surface concentration (Evans et al., 2012) with a 0.19 atom per ion yield (Killen et al., 2004), predict a nominal sputtered Na source of only 7.6×10^{21} Na atoms s^{-1} . Precipitation rates of 3×10^{26} Na ions s^{-1} have been proposed as an upper limit (Kallio & Janhunen, 2003) and could compensate for some of this deficit. If the cusp footprints were to shift 30° equator-ward from the average, which can occur during substorm-like events (Slavin et al., 2010a), the solid curve of Panel B would result, given a 1:3 north-south precipitation ratio. Even in this extreme case, the ion impact rate matching the peak of Panel A remains nearly an order of magnitude higher than the upper limit. Moreover, both profiles in Panel B are distinctly wider than the observations, a consequence of high ejection energies. These considerations suggest that the sputtered contribution to the Na escape flux is relatively small, and an alternative mechanism is likely to be responsible.

Narrower tail widths appear if ion-enhanced PSD is considered, shown in Panel C. Nominal backgrounds are assumed for sputtering and micro-meteor vaporization sources, while diffusion-limited PSD is scaled to the peak brightness. Cusp positions

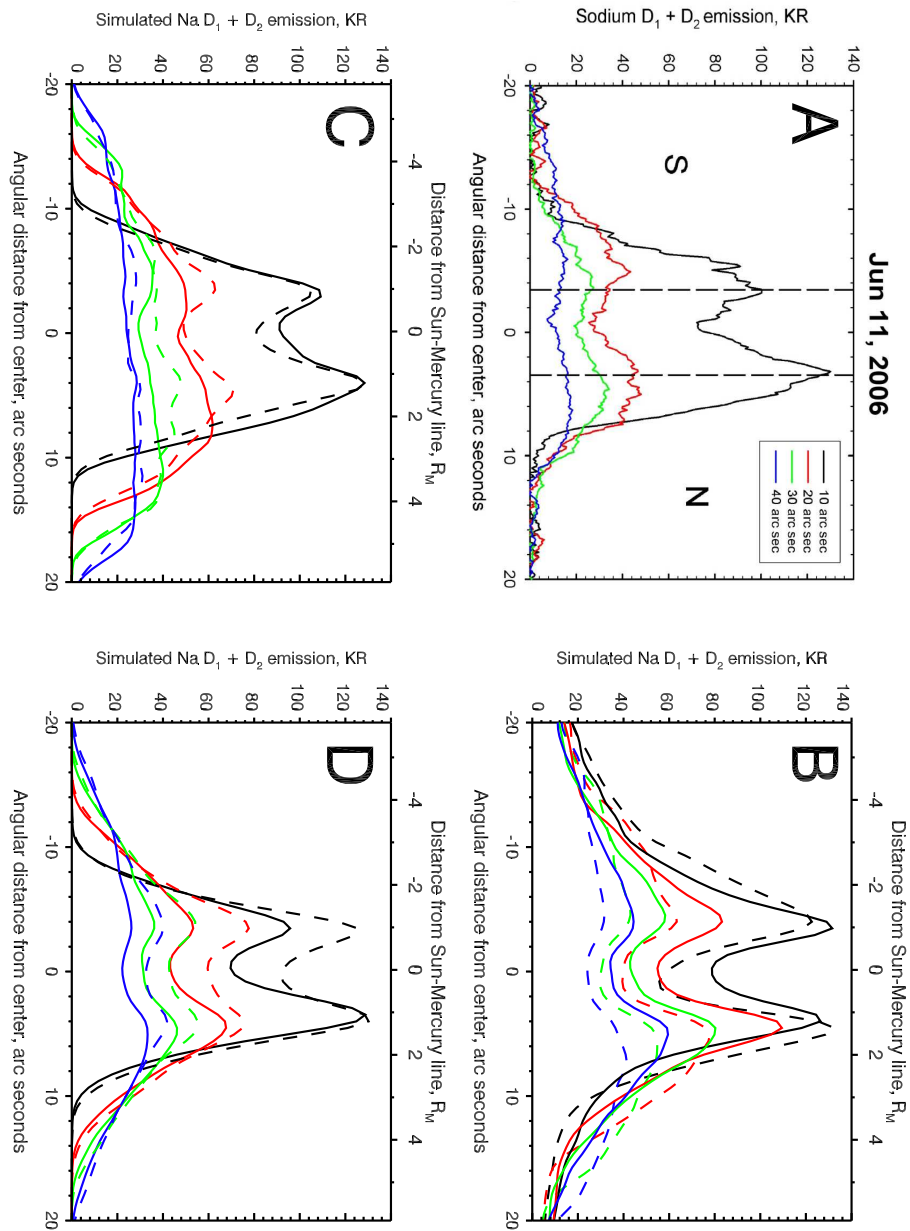


Figure 5.6 North-south cross-sections in Mercury's tail. (A) Observed brightness at 4 down-tail distances by Potter & Killen (2008), note the date represents local time. (B) Results from asymmetrically sputtered sources at the cusps. Dashed lines result from high latitude ejection, while solid lines result from ejection at mid latitudes. (C) Results of photo-desorption enhanced at the average cusp positions. Dashed lines result from lunar-type desorption, while solid lines result from SiO_2 (cf. Figure 4.6). Required rates exceed the diffusion-limited PSD rate. (D) Results in which meteorite vaporization rates are scaled. The dashed line results from $\sim 10^7$ atoms $\text{cm}^{-2} \text{s}^{-1}$. The solid line results from 4×10^7 atoms $\text{cm}^{-2} \text{s}^{-1}$ in combination with PSD enhancements at the cusps and near dawn.

based on (Winslow et al., 2012) are invoked and a κ of 9 enhancement due to increased diffusion is shown. The dashed line results from a lunar-type energy distribution and the solid line from a SiO_2 energy distribution, which better agrees with the brightness down-tail. Lower latitude cusps yield a more tapered cross-tail profile, nearly 3 arc-seconds decrease in FWHM for the black contour if the cusp footprints were to shift 30° equator-ward from the average. Though escape rates are lower, isotropic ejection angles better reproduce the tail width compared to ejection in which the direction is weighted by the cosine of the angle from the surface normal (e.g., Leblanc & Johnson, 2003). Escape rates are a steep function of the thermal accommodation that occurs when atoms bounce off the surface, parameterized as 0.2 in Panel C. For a thermal accommodation ≥ 0.2 , the emission falloff with distance approaches that in Panel A, but less than 1% of Na atoms escape given either PSD energy distribution in Figure 4.6. If elastic rebounds are simulated (thermal accommodation = 0), escape follows many bounces and reaches $\sim 6 - 8\%$ of the total source. In this case, sub-solar desorption is $\sim 10^7$ atoms $\text{cm}^{-2} \text{s}^{-1}$, consistent with the diffusion limited supply proposed by Killen et al. (2004). The emission falloff as a function of distance down-tail is poorly reproduced, however, by a thermal accommodation ≤ 0.2 . A thermal accommodation of ~ 0.2 and source rates that exceed the diffusion-limited PSD flux at the sub-solar point are required to fit these tail measurements. To reconcile the measurements with the diffusion-limited flux, one must assume higher impact vaporization rates.

The dashed line in Figure 5.6 Panel D shows the result of a 15x increase in micro-meteor vapor. Such intense meteoritic flux is consistent with recent estimates (e.g., Borin et al., 2010), and the width of the tail at distance is better reproduced compared to localized PSD enhancements at the cusp footprints. Yet, such high impact production rates are not consistent with this dataset, since adding them to nominal

values for mid-latitude sputtering and PSD yield a negligible north-south asymmetry, even with a κ of 9.

The solid line in Panel D results from a combination of micro-meteor and ion-enhanced PSD sources, with sputtered contributions included though insignificant. In this case, micro-meteors vaporize an average of 4×10^6 atoms $\text{cm}^{-2} \text{s}^{-1}$ into the exosphere, which is consistent with the meteoritic escape rate found by Mouawad et al. (2011), taking into account the energies assumed. Ion-enhancement of PSD is parameterized using a κ of 9, and a sub-solar point rate of $\sim 10^7$ atoms $\text{cm}^{-2} \text{s}^{-1}$. PSD in excess of these values results in excess emission in the wings of the cross-tail profile, as seen in Panel C. Additionally, simulated photo-desorption is enhanced just after dawn, an effect which will now be discussed in detail.

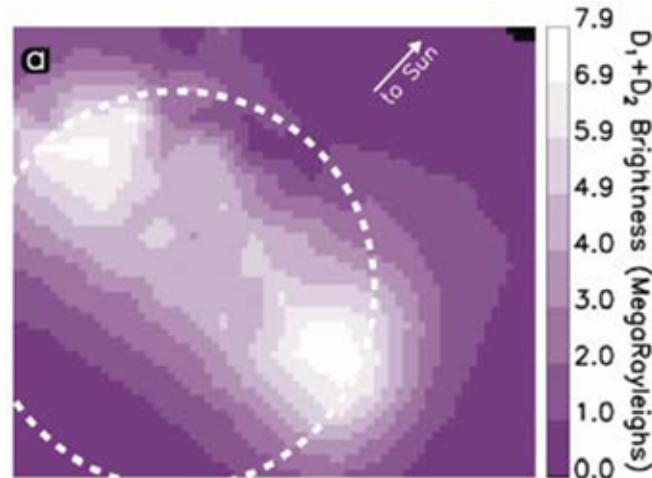


Figure 5.7 Adapted from Baumgardner et al. (2008). A resolved image of the Na exosphere over Mercury's disk taken with the image slicing spectrograph and the AEOS (Advanced Electro Optical System) telescope on 8 June 2008. This image was taken just 3 nights prior to the spectrograph slices in the tail by Potter & Killen (2008), which are modeled in Fig. 5.6.

Near simultaneous measurements of structure in both the bound and escaping atmosphere provide important constraints on model parameters. Baumgardner et al.

(2008) made high resolution measurements of sodium above Mercury’s disk three nights prior to the tail observations of Potter & Killen (2008), shown here in Panel A. Utilizing adaptive optics, these disk-resolved observations show emission concentrated at mid to high latitudes, consistent with the average cusp footprints (Winslow et al., 2012), and large ion enhancements in PSD ($\kappa \approx 9$). For reference, Baumgardner et al. (2008) Figure 1 (Panel A) is reproduced here in Fig. 5.7. The D-line brightness over dawn thru mid-morning regions was $\sim 4\text{-}5$ MR, and ≤ 1 MR at the sub-solar point, indicating a substantial increase in the morning exosphere given the $\sim 80^\circ$ phase angle. The Baumgardner et al. (2008) measurement is well reproduced by photo-desorption rates that exponentially decay from dawn by $1/e$ in one Earth week, or approximately one hour local time at the equator. Exospheric sodium adsorbed to the cold nightside surface is likely to bond ionically with binding energies similar to native Na (Madey et al., 1998). The depletion of this population is a plausible cause for the observed dawn-side enhancement.

MESSENGER’s Fast Imaging Plasma Spectrometer (FIPS) has detected a substantial presence of Na^+ during nightside equatorial crossings (Zurbuchen et al., 2011) which are expected to precipitate at mid-latitudes (Delcourt et al., 2003). To simulate the effect of nightside precipitation on subsequent dawn-side PSD, 2.3×10^{25} Na atoms s^{-1} are released at mid-latitudes near dawn, 61°N and 40°S , corresponding to footprints of a dipolar L shell of 2.5. For an isotropic pitch angle distribution, ion precipitation is ~ 2.8 times greater in the southern hemisphere, where the loss cone is significantly larger at the surface intersect than in the north. Given that the gyro-radii of nightside ion impactors is several hundred km (Zurbuchen et al., 2011), the affected regions are assumed to spread over a wide range of latitudes; $\sim 30^\circ$ to first order is consistent with Baumgardner et al. (2008). Walsh et al. (2013) demonstrated that magnetospheric ions can impact over lower latitudes with 2.4 times greater precipita-

tion in the south than the north. While high latitudes produced excess brightness in the wings of the tail, adopting their locations as an input yielded profiles across the Na tail that did not deviate significantly. At the distances considered, the effect does not depend critically on the position of night-side ion impacts.

In the solid line of Figure 5.6 panel D, an approximate agreement to the Potter & Killen (2008) data is found for a total desorption rate of 4.3×10^{25} Na atoms s^{-1} , half of which originates before 10 am local time. The total deposition of Na^+ to the nightside has been estimated on the order of 10^{23} per second (Delcourt et al., 2003). This ion recycling rate alone is insufficient to provide such high Na desorption at morning. Rather, north-south asymmetries in a morning source enhancement are attributed to anisotropies in adsorption of exospheric Na, and to nightside ion impacts. Nightside impactors may aid the subsequent diffusion of Na more than solar wind protons, given their impact energies (Delcourt et al., 2003; Sarantos et al., 2010). If source energies based on desorption from a lunar sample are used (see Figure 4.6), the requisite source is 15% greater than Na desorption from quartz, as the high-energy tail to this distribution allows less escape.

Figure 5.8 gives simulation results that show how this neutral sodium tail would appear under perfect seeing from Earth. White lines identify locations where cross-sectional slices were taken to produce the solid line in Figure 5.6 Panel D, corresponding to slit positions of the spectrograph used by Potter & Killen (2008). As the migration from the southern source enhancement takes place very close to the surface, the asymmetry is seen quite close to the planet. The northern enhancement becomes more difficult to detect with distance, especially beyond $\sim 10 R_M$. The panel at right displays the associated column density to show where sources are prominent above the surface. At mid and high latitudes, ion precipitation and high surface concentrations enhance the Na exosphere. The exosphere is also enhanced at morning where

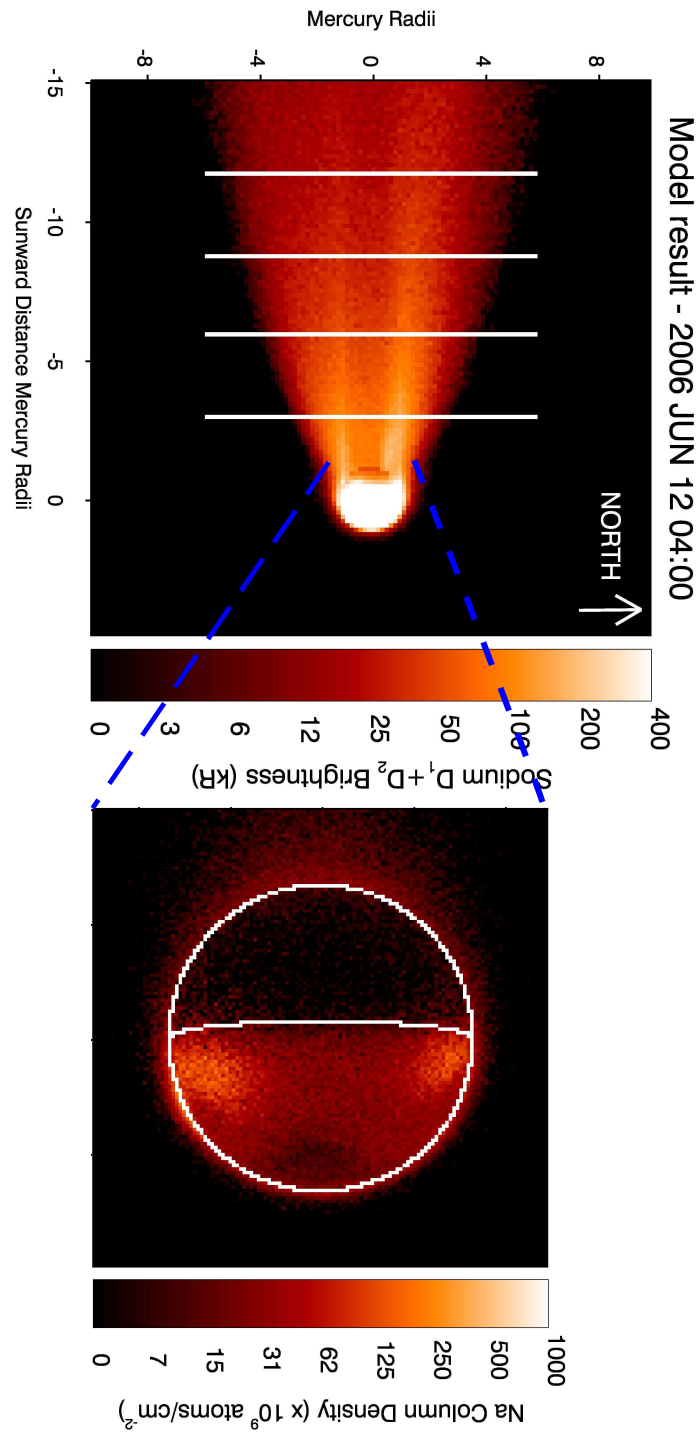


Figure 5.8 Simulated Na tail for meteoritic and photo-desorbed sources. The 4 white lines trace slices taken for the profiles of Figure 5.6 Panel D.

incident sunlight first becomes significant in intensity, however, this is also where the observer's path length through the atmosphere is shortest, at the center of the planet's disk. The confluence of these effects results in a low-latitude column density that is relatively flat across the visible dayside, except near the hot sub-solar point where the PSD source is depleted.

Figure 5.9 offers a summary of the scenarios used in simulating these asymmetries. Orange surface regions delineate regolith impacted by ions. Escaping Na trajectories indicate migration effects using modeled paths for vertically desorbed Na at 2 km s^{-1} during the Potter & Killen (2008) measurement on 12 June 2006. Dotted lines indicate trajectories from a southern source (green) and a northern source (orange). Desorption mainly re-distributes Na atoms that eventually accommodate to cooler surfaces; the light blue trajectory shows 1 km s^{-1} bound atoms. Ions attached to field lines shown close to the night-side can impact the surface during frequent dipolarization events in the magnetotail, and night-side ions precipitate to mid-latitudes via plasma convection during intense magnetic reconnection (Sundberg et al., 2012).

The escaping fraction of desorbed sodium depends on the depletion of available desorption sites throughout the morning, though the depletion timescale had only a small effect on the shape of the simulated tail profile. A two order of magnitude increase in the topmost surface concentration due to adsorption with a one week e-fold depletion is used here based on the Baumgardner et al. (2008) observations. Mura et al. (2009) found an even higher dawn enhancement in PSD, but with decay of more than an order of magnitude over this time. Column content estimated by Sprague et al. (1997) showed a much longer e-fold falloff over more than 6 hours local time, and similar decay rates are seen in the Leblanc et al. (2013) data. The one Earth week e-fold decay rate in Na surface concentration assumed here is nearly ten times longer than that predicted by Mura et al. (2009) or Sprague (1992), but shorter than

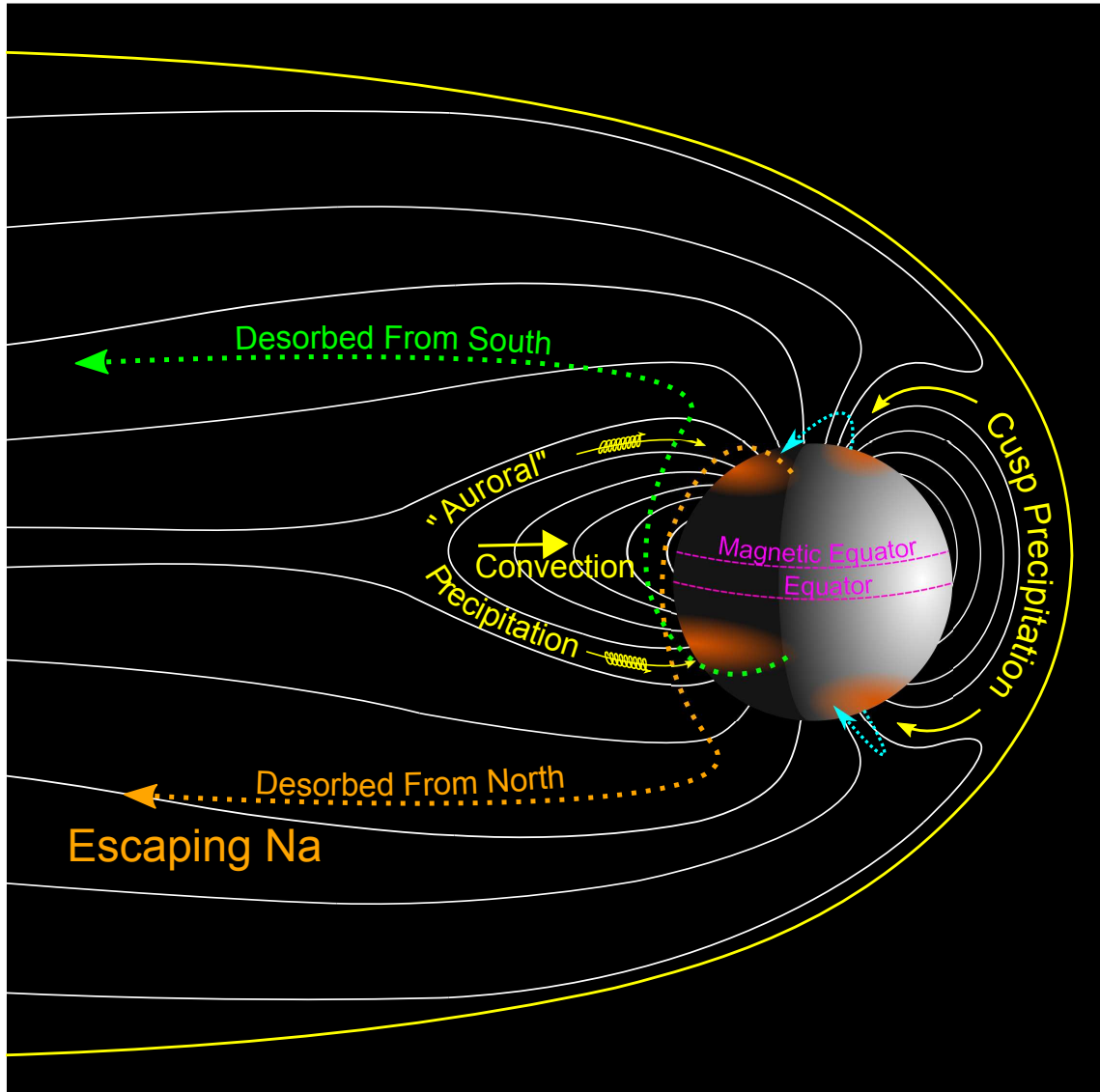


Figure 5.9 A diagram showing characteristic regions of ion precipitation and sodium trajectories at Mercury. Precipitation is separated into cusp components on the day-side, and “auroral” components on the nightside. Orange shows surface regions subject to ion bombardment, where fresh sodium diffuses to the surface and desorbs into the exosphere upon heating and exposure to sunlight. Trajectories for sodium vertically ejected at 1 km s^{-1} from the cusps are shown in blue. Escape trajectories are shown for particles desorbed near dawn.

the Sprague et al. (1997) and Leblanc et al. (2013) observations. Simulations using a one Earth day time constant better approximate the removal of ion implanted Na proposed by Killen & Morgan (1993), and result in 50% greater escape. The PSD rate determined in these simulations may be lower depending on Na depletion rates, but still exceeds those previously derived (Schmidt et al., 2012) as a consequence of lower ejection energies.

These results represent the time-averaged conditions in the Mercury system, while solar wind and interplanetary magnetic field (IMF) conditions should still affect the exosphere. Sarantos et al. (2001, 2007) have modeled the solar wind ion precipitation locations on Mercury’s surface for different IMF configurations. Like the Earth’s magnetosphere, solar wind plasma has access to the system primarily during southward IMF conditions ($B_z < 0$). When the IMF is southward, Sarantos et al. (2001) showed that the radial (B_x) IMF component can induce a north-south asymmetry in particle precipitation. For a $B_x > 0$ (sunward pointing), solar wind ions have a momentum component which is parallel to Mercury’s open field in the southern hemisphere, and hence more precipitation in the southern hemisphere is expected, further offsetting the north-south asymmetry. The opposite effect occurs for $B_x < 0$, acting to cancel out the inherent asymmetry in precipitation imposed by Mercury’s offset dipole. The sign of the B_x component shares equal likelihood between these cases (Sarantos et al., 2007), but an IMF driven asymmetry occurs primarily during southward IMF conditions when magnetic reconnection is strongest.

MESSENGER has recorded the IMF conditions while the spacecraft is outside of Mercury’s bow shock and magnetosphere, at least 1 hour prior to first flyby (M1), and 1.5 hours prior to the second flyby (M2). For several hours prior to the M1, B_z was variable and $B_x < 0$. As such, slightly more ions may have precipitated toward the northern hemisphere. For several hours prior the initial crossing of the bow shock dur-

ing the M2 flyby, B_z was oriented north-ward, resulting in a magnetosphere that was more closed to solar wind plasma. This may explain why a north-enhanced asymmetry was more pronounced in the Na tail during M1 than during M2 (McClintock et al., 2008; Vervack et al., 2010). Relatively little precipitation would have occurred prior to M2 measurements under north-ward IMF conditions. More particles were able to reach the surface during M1, though the B_x induced asymmetry may have somewhat mitigated the 1:4 north-south asymmetry inherent to the offset dipole (Winslow et al., 2012).

Many datasets confirm sodium sources concentrated at dawn (e.g., Sprague et al., 1997; Schleicher et al., 2004) with brightness peaks in the southern hemisphere (e.g., Mangano et al., 2009) as indicated by these results. On average, brighter emission in the southern hemisphere relative to the north has been reported when the dawn terminator was in view, an effect not seen at dusk (Potter et al., 2006). Measurements at 96° TAA by Leblanc et al. (2013) show D2 line brightness narrowly confined to regions near dawn, with mid-latitude enhancements. During the flybys, MESSENGER fantail observations showed excess in the northern and dusk portions of the tail (Vervack et al., 2010), and now in orbit, the FIPS instrument reveals equatorial Na+ concentrated near dawn just above the surface and tail-ward of dusk at 2-3 R_M (Raines et al., 2013 in press). Both are consistent with trajectories of escaping particles that have drifted to the opposite hemisphere before traveling down-tail, given enhanced sources near dawn and in the southern hemisphere.

Chapter 6

Summary

6.1 Conclusions

“What is/are the source/sources of Mercury’s atmosphere?” The exosphere is sustained primarily by photon-stimulated desorption with an added contribution from micro-meteorite impacts. This is indicated by my model comparisons with both the seasonal variability in sodium escape in Section 5.2.3, and the shape of the cross-tail profile in Section 5.3.1.

“How much of Mercury’s atmosphere is escaping?” As much as 20% of the sodium atoms displaced from the surface into the atmosphere will escape the planet. This is based on the my modeling of the escape of Na ejected from the surface by photon-stimulated desorption and micro-meteorite vaporization of Na in Table 5.2.

“How does this escape vary with time?” Escape varies with solar radiation pressure. This based on analysis of the coronagraph data at different orbital phases in Section 3.5.4. However, second order short-term variations due to meteor impacts and space weather cannot be ruled out. Further data analysis is needed to determine if escape is also a function of variable source rates at the surface.

“Do sources keep up with losses?” Seasonally, no. There are portions of Mercury’s orbit in which the bound exosphere becomes depleted due to losses by escape. This is evident in the Leblanc & Johnson (2010) data, in which seasonal depletions in the dayside content match the seasons where I observe the maximum atmospheric escape (see, for instance, Figure 2.13). The influx of meteoritic Na balances the average loss, however, and on geological time scales the sodium abundance should be approximately constant.

“Is the atmosphere coupled to the magnetosphere?” Yes. The effects of ions precipitating to the surface are observed in both the bound and escaping atmosphere. The asymmetry in north-south precipitation (due to the offset magnetic dipole) imprints a signature on the spatial distribution of exospheric sodium. This is based on Section 5.3.1, in which my modeled effects of ion precipitation are compared to the near simultaneous observations of Baumgardner et al. (2008) and Potter & Killen (2008) showing exospheric north-south asymmetries.

6.1.1 Summary of Observational Results: Schmidt et al. (2010)

The brightness of scattered sunlight suggests a strong correlation between the characteristics of the tail and the effects of radiation acceleration. My observations imply an increased escape rate during times of high radiation acceleration. Escape rates are determined to increase from 4.6 to 12.6×10^{23} atoms s^{-1} , as radiation acceleration increases from ~ 115 to ~ 184 cm s^{-2} , half of the 3.7 m s^{-1} gravitational acceleration. This is considered to be a steady state baseline escape which is a function of Mercury’s orbital position, rather than a transient ion sputtering effect, as no disturbances in solar environment were found to occur at these observation dates. Rates of exospheric atoms lost to the tail are consistent with those found by Potter

et al. (2002) and Potter & Killen (2008) at a similar orbital phase. However, during an orbital phase of maximum radiation pressure I find that sodium escape from Mercury exceeds 10^{24} atoms s^{-1} , nearly twice the highest previously published rate (McClintock et al., 2008). At this time, escape becomes a substantial fraction of the total planetary production. This is repeatedly observed in long-term surveys; a $\sim 40\%$ decrease in the disk averaged emission is found at this true anomaly angle (Leblanc & Johnson, 2010). My most recent observations in Fig. 2.18 demonstrate significant escape at orbital phases where prior studies predict the tail should disappear beyond the detection limit (Potter & Killen, 2008).

An escaping tail of neutral sodium atoms persists over a significant portion of the planet's orbit with an extent of several hundred Mercury radii. Using the wide-field imaging method, a single image can capture a ~ 10 h time history in which the tail is bright enough to observe possible changes in escape rates. No observations, to date, give evidence of emission changes on an hourly timescale that can be attributed with confidence to variations in sodium production rates associated with solar activity or meteor flux. However, continued observations and modeling will show if characteristics of the escaping atmosphere indeed depend on orbital conditions alone. The expansion rate of the tail's width remained nearly constant over five measurements, implying that the energy of the escaping population does not vary with time.

6.1.2 Model Results based on the Wide-Field Data: Schmidt et al. (2012)

Given our current understanding of precipitating ions and sputtered energies, I have eliminated ion sputtering as an effective means of atmospheric escape on Mercury. Even with a generous upper limit of 1.3×10^{23} atoms s^{-1} , the total flux of sputtered sodium, previously considered the primary supplier of the tail (e.g., Potter & Killen, 2008), is shown to constitute only a small fraction of the escaping population. Total sputtered source rates reported for the first two MESSENGER flybys

were much smaller still than my upper limit: 3.5×10^{21} atoms s^{-1} and 2.3×10^{21} atoms s^{-1} , respectively, (Burger et al., 2010). Although the fraction of this population escaping the planet is substantial, my simulations conclude that the sputtered source rate is likely to be more than an order of magnitude smaller than the $\sim 10^{24}$ atoms s^{-1} needed to sustain the recorded brightness in the distant tail.

I have shown that micro-meteorite impact vaporization, while more significant than sputtering, is also not the dominant escape mechanism. Currently, our knowledge of the impactor flux at Mercury is quite poorly constrained. Burger et al. (2010) estimated an impact vaporization source rate of 3.5×10^5 atoms $\text{cm}^2 \text{s}^{-1}$, about half that assumed by Leblanc & Johnson (2003). The recent study by Borin et al. (2010) suggests it may be substantially higher still due to migration of dust particles by the Poynting-Robertson effect. My derived Na production rates that match the observed tail brightness are 3.6×10^6 and 1.8×10^6 atoms $\text{cm}^2 \text{s}^{-1}$ for a 3000 and 5000 K vaporized population, respectively, if this were the only source of escaping sodium. This is approximately the minimum meteoritic source rate determined by Borin et al. (2010) accounting for asteroid dust migration into the inner solar system. Even at 5000 K, however, the width of the tail is significantly narrower than our observations. Judging from lunar effects, analysis of the LCROSS impact suggests a temperature of only 1000 K in the Na plume (Killen et al., 2010a). Although impact velocities at Mercury are expected to be 7 to 9 times faster than LCROSS, a plume temperature < 3000 K may be more realistic (Borin et al., 2009). It has been suggested that a small fraction of Na produced during meteor impacts may be in the form of oxides and hydroxides (Berezhnoy & Klumov, 2008). The photolysis lifetimes of these molecules are short on Mercury compared to the ballistic time of flight to collide with the surface (Self & Plane, 2002). Neutral Na resulting from this photo-decomposition retains an energy of the order of the molecular bond strength, resulting in a trace

but energetic (1-2 eV) Na population. Although the production of these high-energy atoms is poorly constrained, it is possible this process may widen the cross-tail profiles of impact-vaporized sources significantly, allowing a better match to the Schmidt et al. (2010) data.

Sources with a high-energy tail feature in the velocity distribution best fit the observed sodium tail width, in particular, a fast PSD source with a 10 eV maximum energy cutoff. Mura et al. (2009) determined fast PSD to be the primary source in simulations of the exosphere during the 2003 transit of Mercury across the solar disc. A large set of observations by Potter et al. (2007) showed a 30% reduction in dayside Na column density between minimum and maximum radiation pressures. This reduction is found to be 33% and 38% for slow and fast PSD, respectively, and a globally averaged supply rate of 4.8×10^7 and 9.7×10^6 atoms $\text{cm}^{-2} \text{s}^{-1}$ is required to match my wide-field observations if PSD alone was the source of all escaping sodium at Mercury. However, the observed polar brightness suggests twice the supply of sodium in cusp regions compared to other day-side areas (Baumgardner et al., 2008), and PSD in these regions is found to yield much higher escape rates than a photon-limited case, which peaks at the subsolar point. As shown for sputtering, localized polar sources of energetic sodium would be evident in bright flanks in the northern- and southern-most regions of the tail in a smaller field of view. While observations suggest this may be the case, such features are difficult to distinguish from the effects of shadowing (Potter & Killen, 2008).

Atoms liberated from Mercury's surface by both PSD and micro-meteoroid impact vaporization contribute significantly to the escape of atmospheric sodium from Mercury. Maxwellian velocity distributions at 1500 and 3000 K, corresponding to PSD and to impact vaporization, respectively, best matched the escape flux as a function of orbital phase found in my wide-field data set. However, both of these thermal dis-

tributions lacked the high-energy atoms needed to match the observed width of the comet-like neutral tail. The energy distribution of atoms released into the exosphere must have two key features: (1) a low peak energy (~ 1000 K), so that the escape rate varies substantially with orbital phase, and (2) a high-energy tail sufficient to match the observed width far from the planet. Measured energy distributions of sodium released by desorption off a lunar sample induced by electrons (representative of UV photons) best match these criteria (Yakshinskiy & Madey, 2004). High-energy sources require a large degree of driven variability to match the escape observed in the Schmidt et al. (2010) data set. Of the six characteristic sources modeled, a 1500 K PSD source and a 3000 K impact vaporization source showed the least deviation from steady state in order to match the brightness at multiple orbital phases. A PSD source with a high-energy tail best matched the observed width of the escaping sodium population at Mercury.

Sufficiently large meteoroids (>30 cm in radius) impacting the surface could be identified using ground-based wide-field imaging techniques by the resulting plume of sodium in the vaporized regolith several hours after impact, depending on the impact location. Variable source processes on longer timescales, rather than a single instantaneous impact, such as ion precipitation and meteors showers from Sun-grazing comets, resulted in an overall brightening of the sodium tail as a whole instead of distinct hot spots.

The model predicts that an isolated sodium feature should appear at more than 100 planetary radii from Mercury during the “in” leg of the orbit. As seen in Figure 5.3, the terrestrial background noise at the time of my observation is considerable. Although the signal to noise level of 1.36 is insufficient to accurately quantify this feature’s brightness, a local maximum exists in the coronagraph data at the $\sim 175 R_M$

anti-sunward distance forecast by the model. Follow up observations will certainly be able to confirm or refute my prediction.

6.1.3 Summary of North-South Asymmetry Study: Schmidt (2013)

Using 3-D numerical modeling, I have demonstrated that ion precipitation, enhanced in the south, can result in the observed Na emission profiles across the tail that are brighter in the north (Baumgardner et al., 2008; McClintock et al., 2008; Potter & Killen, 2008). However, sources located at high latitude cusp footprints on the dayside are unable to match the observed width of the brightness profiles across the tail. Instead, my simulations provide evidence for lower latitude sources, which may result from magnetospheric ion precipitation. Such source regions would be enhanced on the dawn-side given the accumulation of sodium and ion impact sites during the long Mercury night, especially at orbital longitudes following maximum precipitation at perihelion. Photo-desorption, rather than ion sputtering, is determined to be the responsible mechanism for this population's release and escape from the planet's surface. I find that a thermal accommodation, $\alpha \sim 0.2$, best reproduces the simultaneous measurements of Potter & Killen (2008) and Baumgardner et al. (2008), consistent with the range of 0.1 to 0.3 determined by Mouawad et al. (2011). If α is as large as 0.62, as Hunten et al. (1988) proposed, sources with a Maxwellian energy distribution are not consistent with the observed width of the Na tail in Schmidt et al. (2010).

The results of simulated asymmetries in the sodium tail can be summarized in three key points. First, sodium escaping Mercury's gravity via high radiation pressure drifts to the opposite hemisphere of the tail. This is especially true for low energy sources such as PSD, where migration occurs very close to the disk. Northern enhancements in the portion of the tail near dusk seen in the MESSENGER spacecraft roll during M2 (Vervack et al., 2010) are therefore consistent with enhanced sources at dawn in the southern hemisphere. Secondly, low energy sources provide a better

match to both the width and brightness of each tail lobe than simulations using a sputtering source. PSD rates enhanced at latitudes of ion bombardment yield similar structure in comparison with both the Potter & Killen (2008) and Baumgardner et al. (2008) data, observations made just a few days apart. Third, sources at the magnetospheric cusps supply relatively little Na directly to the tail. Both sputtered and desorbed sources at the cusp footprints yield a Na tail of width far in excess of what is measured (Potter & Killen, 2008). Furthermore, the requisite ejection rates from these regions to reproduce the peak D line brightness would well exceed reasonable estimates. Alternatively, magnetospheric ion precipitation to Mercury’s night-side is shown to be a viable mechanism for producing the exosphere asymmetries observed and best matches the wings of the tail profiles.

6.2 Discussion

As the strong effects of radiation pressure at vary uniquely for each species in Mercury’s atmosphere, it should be noted that sodium is not an ideal tracer for the spatial distribution of other atmospheric constituents. Potassium is the species present with the most similar characteristics in terms of photoionization lifetime, ejection mechanisms and radiation pressure (Smyth & Marconi, 1995; Yakshinskiy & Madey, 2005). Though potassium tail structures analogous to Na should exist in principle, their detection is hindered by the low abundances — observed Na to K ratios span a range from 36 to 260 (Killen et al., 2010b; Leblanc & Doressoundiram, 2011). Additional atmospheric constituents may share the same source mechanisms as Na and K. The best measurements of such species come from MESSENGER, and only the refractory elements Ca and Mg are well characterized currently. Ca and Mg temperatures are much hotter (20,000 - 50,000 K) suggesting the bulk populations are the products of molecular dissociation (Killen et al., 2010b; Burger et al., 2012). At such high ener-

gies, substantial escape of these species is observed in the tail region, despite the lesser effects of radiation pressure compared to Na (Vervack et al., 2010).

Near true anomaly angles of $\sim 65^\circ$, I show that roughly 20% of Na atoms displaced from the surface into the atmosphere will escape. Long term (daytime) observing campaigns utilizing solar telescopes have repeatedly observed a depletion by nearly 40% in the disk-averaged exosphere at this orbital phase (Leblanc & Johnson, 2010). Reconciling these figures suggests that the average residence time for a Na atom in the exosphere is, perhaps not surprisingly, a function of radiation pressure. At maximum radiation pressure, residence times 75% of the average would account for gains in the tail balancing losses in the bound exosphere. While the escaping fraction I have determined is higher than previous estimates (Potter & Killen, 2008), it is much less than the $\sim 50\%$ hypothesized to escape the lunar gravity (Wilson et al., 2003).

The five measurements of Mercury's sodium tail I reported in Schmidt et al. (2010) span distances 0.023 to 0.042 AU from the ecliptic plane. Of these, the brightest observation and highest column density occurred at the farthest distance from the ecliptic plane. Furthermore, the recorded brightness as a function of distance from the ecliptic plane is anti-correlated with the disc-averaged trend used in the study of Kameda et al. (2009), in which higher source rates near the symmetry plane were proposed because of interplanetary dust. I have shown that radiation acceleration can strip a significant portion of Mercury's sodium exosphere from the planet, and pointed out that Mercury's orbit is such that radiation pressure is strongest near the greatest distance from the ecliptic plane. The effect reported in the study by Kameda et al. (2009) is therefore interpreted as losses in the gravitationally bound sodium via radiation pressure, observed as gains in the tail.

The results of my Schmidt (2013) asymmetry study connect spatial patterns observed in the escaping Na tail with those of the gravitationally bound exosphere, al-

though not without raising further questions. Given the desorption energies in Figure 4.6, optimum parameters used in this model fit both the dayside brightness (Baumgardner et al., 2008) and the tail brightness (Potter & Killen, 2008) simultaneously within a factor of two. That is, accurately modeling the tail gives a bound exosphere twice in excess of the Baumgardner et al. (2008) dayside emission, or matching the dayside emission yields only half the escape measured by Potter & Killen (2008). Resolution and residual seeing effects may account for some of this discrepancy, and disk-averaged emission lies within the range measured by Leblanc & Johnson (2010). Surface reflectance has not been included in this model. The associated radiation pressure, while only a few percent of the solar value, may allow significantly more atoms in the high energy tail to escape. Another possibility is that hermean PSD energies are higher than the laboratory results in Figure 4.6. For the slow and fast energies investigated by Mouawad et al. (2011), 2.3 and 89 times more Na atoms escape, respectively, when compared with the dotted line in Figure 4.6 (particular to this orbital phase, neglecting surface bouncing or ion enhancements). Thus, increasing the photo-desorption energies would also better reproduce brightness in the bound and escaping exosphere simultaneously.

Dawn-dusk asymmetries are likely to be seasonal, correlated with the approximate tidal locking effect near perihelion and the rate of advance of the morning terminator. While space weather also imposes seasonal modulation, precipitation driving north-south asymmetries is irregular. Such variability may explain why, though the orbital phase was similar, the Na tail during the second MESSENGER flyby appeared more symmetric than the first (McClintock et al., 2008; Vervack et al., 2010). I demonstrate that time averaged space weather conditions given by (Winslow et al., 2012) should, however, produce a substantial asymmetry in the tail, as is most commonly observed (Baumgardner et al., 2008; McClintock et al., 2008; Potter & Killen, 2008).

The surface concentration of Na can be thought of as a reservoir that feeds the exosphere. Atoms re-adsorbed from the exosphere, meteoric Na, and precipitating Na^+ through the magnetosphere all add to the surface concentration, while the escaping Na tail and Na^+ escaping the magnetosphere deplete the surface reservoir. It is important to note that sources and sinks of the Na surface reservoir are not balanced self-consistently in my model. That is, I assume the spatial distribution of Na in the surface rather than simulating it in numerical steady state equilibrium. The architecture of my model permits Na adsorbed by the exosphere to influence the spatial distributions of Na available to each exospheric source process. However, meteoritic and magnetospheric contributions to the reservoir must also be considered for a conserved self-consistent balance between sources and sinks. Leblanc & Johnson (2010) have presented a model in which the balance of Na between the surface reservoir and the exosphere is conserved. This approach is more computationally expensive than the model I present here, as it tracks nearly 1000 surface particles for every exospheric particle. Their work suggests Mercury's surface reservoir contains $\sim 10^{31}$ Na atoms and between 1.6 and 4.5×10^{28} Na atoms in the exosphere.

The physical parameters governing a detailed model of the balance between surface reservoir and the exosphere remain uncertain. In particular, the rate at which Na is supplied to the topmost surface of regolith grains is poorly known. The Arrhenius diffusion rates, (rate constant $k = Ae^{-E_a/(k_B T)}$, where A is a constant, k_B is Boltzmann's constant, T is temperature, and E_a is the activation energy) of Na through the grain are highly dependent on how vitrified the surface is. Diffusion coefficients for Na through glassy grains are several orders of magnitude higher than for mineral grains (Čapek & Borovička, 2009). The temperature dependence of diffusion from depth must therefore consider the ensemble of grains types and sizes. Plasma precipitation creates defects in the grain, which increase the diffusive supply to exospheric source

processes, an effect that is dependent on the plasma energy (Sarantos et al., 2010). Furthermore, diffusion will also depend on gradients in the surface potential (Madey et al., 1998). Kilovolt negative potentials have been measured at the Moon and gradients are expected to be strongest at boundaries between shadowed and illuminated surfaces (Halekas et al., 2008). Each exospheric process depletes the surface reservoir at a different depth; desorption affects the topmost monolayers (Madey et al., 1998), typical ion impacts penetrate a few hundred angstroms (Sprague, 1992), and meteorites excavate at depth. Considering all of these effects and the dynamic conditions in the magnetosphere, a complete treatment of the surface reservoir of Na is therefore complex.

6.3 Future Work

Wide-field coronagraph and image-slicer measurements that I present are generally made within 5 to 10° of the horizon. Given the extreme effects of atmospheric extinction in these data, much time and care will be required for calibration to the desired degree of confidence. As such, only the first two years of wide-field data in this study have been published to date (Schmidt et al., 2010). For these few nights, extinction profiles were compiled from many stars in the field to gain confidence in the extinction with altitude, a laborious procedure when applied to the more than fifty nights of data shown in Table 2.1. In contrast, Figures 2.17 and 2.18 result from the calibration method outlined in Chapter 2 in which only one or two standard stars were used to calculate the atmospheric extinction at the time of exposure. In the time since Schmidt et al. (2010), a data reduction pipeline for the image slicing spectrograph has been developed. Utilizing the occasional short exposure off the coronagraph occulting mask, cross-calibration now can be performed by utilizing simultaneous measurements with both instruments. Data analysis using instrumental cross-calibration and/or ad-

ditional stellar extinction profiles is considered necessary to better constrain potential variability in atmospheric escape independent from orbital effects.

A model of the planet’s surface reflectance can be used to calibrate the image-slicing spectrograph data independently from the method using standard stars which I described in Sections 2.4.3 and 2.4.4. Several other studies use a Hapke model of surface reflection (Hapke, 1986) with the parameters of Mallama et al. (2002) as a photometric standard to calibrate observations of the Na exosphere (e.g., Potter et al., 2006; Leblanc & Johnson, 2010; Mouawad et al., 2011). Forward modeling the reflectance of Mercury’s surface can also give an independent estimate of the atmospheric seeing (e.g., Potter et al., 1999), a useful comparison with my current estimates based on stellar PSF fitting. To increase confidence in the calibration of the image slicing spectrograph data, and by association the coronagraph data, this alternative method should be explored. Following a more rigorous analysis of my nightly extinction conditions as just described, data comparison with simultaneous measurements from other ground-based observatories is planned (cf., Table 2.1).

A model of surface reflectance is also applicable to simulations of the exosphere. Surface reflectance of Mercury may significantly aid in the resonant scattering of the sodium D-lines at Mercury. The contribution of surface reflection to both D-line brightness in the day-side exosphere and escape via radiation acceleration may be non-negligible. Including the effects of surface reflection in the model is computationally intensive, even if the surface is idealized as a smooth sphere which singly scatters sunlight. The vector addition of the Sun-Mercury and the Mercury-particle Doppler shift is needed to compute the spectral flux in the particle’s frame. To then compute the effect on particle trajectories, the phase angle of the planet and the Doppler corrected spectral flux must be calculated at each integration time step for each particle. The Hapke function (Hapke, 1986) must be integrated over the visible region of the

planet in this procedure. A complete treatment of exospheric emission that includes reflectance of the planet's disk should also consider the scattering phase function of the D2 line.

Another prospective project involves serendipitous space-based observations of Mercury's exosphere that were unforeseen. Heliospheric Imagers HI-1 aboard both the STEREO-A (Ahead) and -B (Behind) spacecraft occasionally record emissions extending anti-sunward in a tail from Mercury. These wide-field cameras use "white light" broadband filters designed to image transient in the solar wind via Thomson scattering. Thomson scattering of sunlight from nearby solar coronal electrons is seen simultaneously throughout the HI-1 field with short-term brightness variations near the planet. However, the overall instrument transmission (filter \times detector quantum efficiency) of is only between 1 and 2 percent at sodium D line wavelengths. If calibration is carried out assuming the emission is completely due to sodium D-line emission, HI-1A measurements on 28 January 2009 show a sustained brightness of nearly 30 kilo-Rayleighs over more than 24 hours at a distance of 12 arcminutes from the planet. At this time, the line of sight from STEREO-A and the Sun-Mercury directions differs by only 7° , with the tail pointed toward the Ahead spacecraft. Correcting for path length and projection, this corresponds to a cross-tail brightness of 7 kiloRayleighs at a physical distance of nearly 430 planetary radii. Based on my coronagraph observations of the tail, a sodium D line brightness between 100 and 200 Rayleighs is expected for this orbital phase. It is unlikely that the HI-1A recorded emissions in the kR range would be due to sodium at such distances.

Two possibilities exist to explain this large discrepancy in brightness between STEREO and ground-based imaging. First, an additional source of emission besides that of the sodium D-lines may be present. It is unlikely that bright line emissions from ion, atomic or molecular transitions would have gone undetected by ground-

based Echelle spectrographs (e.g., Bida et al., 2000), hence a broad-band emission source is more probable. Thomson scattering off electrons somehow related to the Mercury system is very inefficient for forward scattering geometries (Howard & Tappin, 2009), which thus far seem inherent to the feature's appearance. The potential for scattering off dust particles remains to be determined. The second possibility is simply uncertainty in the STEREO HI-1 calibration for sodium D emission. The feature is best imaged when the tail is aligned along the line of sight at the edge of the HI field of view. Pre-launch performance calibrations of these instruments are only available for on-axis imaging. Deviations in the calibrated spectral throughput will be highest for objects imaged at the extremes of the field of view, as is the case here. Another source of calibration uncertainty is the stability of the optics coatings with yttrium it is possible that the filter responses have changed since pre-flight testing. Despite these considerations, the STEREO space-based observing capability provides new insights into long and short-term temporal variability in the hermean system and its potential sources.

At the time of writing, the only published data of hermean sodium from MESSENGER were taken during the flybys. That is, no published data were recorded during the spacecraft's orbit. After several Mercury years of in situ observations, this dataset is rich with clues about the seasonal distribution of sodium in the exosphere. Preliminary studies with MESSENGER have already yielded many important developments in our understanding of Mercury's environment. After several hermean years of accumulated data, the MASCS instrument is beginning to reveal seasonal patterns in the exosphere in which both dawn and dusk enhancements are correlated with orbital phase (Cassidy, personal communication 2013). This new information will add important constraints for our understanding of the exosphere, and it is reasonable to expect subsequent revisions to my model in light of new developments.

Major element abundances from the MESSENGER GRS instruments have recently placed firm constraints on the surface mineralogy (e.g., Evans et al., 2012). In light of this information, it is now possible for laboratory experiments to pin down physical quantities that are often treated as free parameters in current exosphere models. Laboratory studies of ion-enhanced diffusion and the associated timescales would much improve our understanding of localized exospheric enhancements and the inferred effects of space weather on the exosphere. In particular, diffusion coefficients for the temperature dependent supply rates of fresh sodium from depth can now be determined. As I've shown in fig 4.5, there is currently little consensus in the community about the energies associated with exospheric source mechanisms, although the yields and energy distributions can be determined empirically. Such experiments are vital to the progress of the field, and, in conjunction with an understanding of the seasonal patterns as revealed by MESSENGER, should provide closure to the outstanding questions regarding Mercury's tenuous atmosphere.

List of Journal Abbreviations

Adv. Space Res.	Advances in Space Research
Ann. Geophys.	Annales Geophysicae
Appl. Opt.	Applied Optics
Astron. Astrophys.	Astronomy and Astrophysics
Astrophys. J.	Astrophysical Journal
Astrophys. J. Lett.	Astrophysical Journal Letters
Geophys. Res. Lett.	Geophysical Research Letters
J. Atmos. Solar Terr. Phys.	Journal of Atmospheric and Solar-Terrestrial Physics
J. Geophys. Res.	Journal of Geophysical Research
Planet. Space Sci.	Planetary and Space Science
Phys. Rev.	Physical Review
PASP	Publications of the Astronomical Society of the Pacific
Space Sci. Rev.	Space Science Reviews
Space Wea. J.	Space Weather Journal

References

- Acton, C. H. 1996, *Planet. Space Sci.*, 44, 65
- Anderson, B. J., Johnson, C. L., Korth, H., et al. 2011, *Science*, 333, 1859
- Baumgardner, J., & Mendillo, M. 2009, *Earth, Moon and Planets*, 105, 107
- Baumgardner, J., Mendillo, M., & Wilson, J. K. 2000, *AJ*, 119, 2458
- Baumgardner, J., Wilson, J., & Mendillo, M. 2008, *Geophys. Res. Lett.*, 35, 3201
- Benna, M., Slavin, J. A., Sarantos, M., et al. 2010, *AGU Fall Meeting Abstracts*, B6
- Berezhnoy, A. A., & Klumov, B. A. 2008, *Icarus*, 195, 511
- Bida, T. A., Killen, R. M., & Morgan, T. H. 2000, *Nature*, 404, 159
- Borin, P., Bruno, M., Cremonese, G., & Marzari, F. 2010, *Astron. Astrophys.*, 517, A89
- Borin, P., Cremonese, G., Marzari, F., Bruno, M., & Marchi, S. 2009, *Astron. Astrophys.*, 503, 259
- Brown, R. A., & Yung, Y. L. 1976, 1102
- Burger, M. H., Killen, R. M., McClintock, W. E., et al. 2012, *Journal of Geophysical Research (Planets)*, 117, 0
- Burger, M. H., Killen, R. M., Vervack, R. J., et al. 2010, *Icarus*, 209, 63
- Burnashev, V. I. 1985, *Abastumanskaia Astrofizicheskaia Observatoriia Byulleten*, 59, 83
- Carlson, R. W., Matson, D. L., & Johnson, T. V. 1975, *Geophys. Res. Lett.*, 2, 469
- Cassidy, T. A., & Johnson, R. E. 2005, *Icarus*, 176, 499
- Chamberlain, J. W. 1961, *Physics of the aurora and airglow*
- Cintala, M. J. 1992, *J. Geophys. Res.*, 97, 947

- Combi, M. R., Disanti, M. A., & Fink, U. 1997, *Icarus*, 130, 336
- Cox, A. 2000, *Allen's astrophysical quantities* (Springer)
- Cremonese, G., Bruno, M., Mangano, V., Marchi, S., & Milillo, A. 2005, *Icarus*, 177, 122
- Cremonese, G., Boehnhardt, H., Crovisier, J., et al. 1997, *ApJ*, 490, L199
- Delcourt, D. C., Grimald, S., Leblanc, F., et al. 2003, *Annales Geophysicae*, 21, 1723
- Delcourt, D. C., Moore, T. E., Orsini, S., Millilo, A., & Sauvaud, J.-A. 2002, *Geophys. Res. Lett.*, 29, 1591
- Dukes, C. A., Chang, W.-Y., Famá, M., & Baragiola, R. A. 2011, *Icarus*, 212, 463
- Evans, L. G., Peplowski, P. N., Killen, R. M., Potter, A. E., & Sprague, A. L. 2013, *LPI Contributions*, 1719, 2033
- Evans, L. G., Peplowski, P. N., Rhodes, E. A., et al. 2012, *Journal of Geophysical Research (Planets)*, 117, 0
- Fujimoto, M., Baumjohann, W., Kabin, K., et al. 2007, *Space Sci. Rev.*, 132, 529
- Hale, A. S., & Hapke, B. 2002, *Icarus*, 156, 318
- Halekas, J. S., Delory, G. T., Lin, R. P., Stubbs, T. J., & Farrell, W. M. 2008, *Journal of Geophysical Research (Space Physics)*, 113, 9102
- Han, X.-Y., Gao, X., Li, J.-M., Vokv, L., & Feautrier, N. 2006, *Phys. Rev. A*, 74, 062710
- Hapke, B. 1986, *Icarus*, 67, 264
- Howard, T. A., & Tappin, S. J. 2009, *Space Science Review*, 147, 31
- Howell, S. B. 2006, *Handbook of CCD Astronomy*, ed. R. Ellis, J. Huchra, S. Kahn, G. Rieke, & P. B. Stetson
- Huebner, W. F., Keady, J. J., & Lyon, S. P. 1992, *Ap&SS*, 195, 1
- Hunten, D., Roach, F., & Chamberlain, J. 1956, *Journal of Atmospheric and Terrestrial Physics*, 8, 345
- Hunten, D. M., Shemansky, D. E., & Morgan, T. H. 1988, 562
- Hunten, D. M., & Sprague, A. L. 2002, *Meteoritics and Planetary Science*, 37, 1191

- Ip, W.-H. 1986, *Geophys. Res. Lett.*, 13, 423
- . 1990, *ApJ*, 356, 675
- Jhon, M. S., & Dahler, J. S. 1978, *Journal of Chemical Physics*, 69, 819
- Johnson, R. E., Leblanc, F., Yakshinskiy, B. V., & Madey, T. E. 2002, *Icarus*, 156, 136
- Kallio, E., & Janhunen, P. 2003, *Geophys. Res. Lett.*, 30, 1877
- Kameda, S., Kagitani, M., Okano, S., Yoshikawa, I., & Ono, J. 2008, *Advances in Space Research*, 41, 1381
- Kameda, S., Yoshikawa, I., Kagitani, M., & Okano, S. 2009, *Geophys. Res. Lett.*, 36, 15201
- Killen, R., Shemansky, D., & Mouawad, N. 2009, *ApJS*, 181, 351
- Killen, R., Cremonese, G., Lammer, H., et al. 2007, *Space Sci. Rev.*, 132, 433
- Killen, R. M. 2006, *PASP*, 118, 1344
- Killen, R. M., Hurley, D. M., & Farrell, W. M. 2012, *Journal of Geophysical Research (Planets)*, 117, 0
- Killen, R. M., & Morgan, T. H. 1993, *J. Geophys. Res.*, 98, 23589
- Killen, R. M., Potter, A., Fitzsimmons, A., & Morgan, T. H. 1999, *Planet. Space Sci.*, 47, 1449
- Killen, R. M., Potter, A. E., Hurley, D. M., Plymate, C., & Naidu, S. 2010a, *Geophys. Res. Lett.*, 37, 23201
- Killen, R. M., Potter, A. E., Reiff, P., et al. 2001, *J. Geophys. Res.*, 106, 20509
- Killen, R. M., Potter, A. E., Vervack, R. J., et al. 2010b, *Icarus*, 209, 75
- Killen, R. M., Sarantos, M., Potter, A. E., & Reiff, P. 2004, *Icarus*, 171, 1
- Krivova, N. A., Solanki, S. K., Wenzler, T., & Podlipnik, B. 2009, *Journal of Geophysical Research (Atmospheres)*, 114, 0
- Lammer, H., Wurz, P., Patel, M. R., et al. 2003, *Icarus*, 166, 238
- Leblanc, F., Chaufray, J.-Y., Doressoundiram, A., et al. 2013, *Icarus*, 223, 963
- Leblanc, F., & Doressoundiram, A. 2011, *Icarus*, 211, 10

- Leblanc, F., & Johnson, R. E. 2003, *Icarus*, 164, 261
- . 2010, *Icarus*, 209, 280
- Leblanc, F., Luhmann, J. G., Johnson, R. E., & Liu, M. 2003, *Planet. Space Sci.*, 51, 339
- Leblanc, F., Chassefiere, E., Johnson, R. E., et al. 2007, *Planet. Space Sci.*, 55, 1069
- Leblanc, F., Doressoundiram, A., Schneider, N., et al. 2009, *Geophys. Res. Lett.*, 36, 7201
- Maday, T. E., Yakshinskiy, B. V., Ageev, V. N., & Johnson, R. E. 1998, *J. Geophys. Res.*, 103, 5873
- Mallama, A., Wang, D., & Howard, R. A. 2002, *Icarus*, 155, 253
- Mangano, V., Leblanc, F., Barbieri, C., et al. 2009, *Icarus*, 201, 424
- Mangano, V., Milillo, A., Mura, A., et al. 2007, *Planet. Space Sci.*, 55, 1541
- Marchi, S., Morbidelli, A., & Cremonese, G. 2005, *Astron. Astrophys.*, 431, 1123
- Massetti, S., Orsini, S., Milillo, A., et al. 2003, *Icarus*, 166, 229
- McClintock, W. E., Bradley, E. T., Vervack, R. J., et al. 2008, *Science*, 321, 92
- McGrath, M. A., Johnson, R. E., & Lanzerotti, L. J. 1986, *Nature*, 323, 694
- Meeus, J. 1998, *Astronomical algorithms*
- Mendillo, M., & Baumgardner, J. 1995, *Nature*, 377, 404
- Mendillo, M., Baumgardner, J., & Flynn, B. 1991, *Geophys. Res. Lett.*, 18, 2097
- Mierkiewicz, E. J., Line, M., Roesler, F. L., & Oliverson, R. J. 2006, *Geophys. Res. Lett.*, 33, 20106
- Mitchell, A. C., & Zemansky, M. W. 1934, *Resonance Radiation and Excited Atoms*
- Morton, D. C. 2003, *Astrophysical Journal Supplement*, 149, 205
- Mouawad, N., Burger, M. H., Killen, R. M., et al. 2011, *Icarus*, 211, 21
- Mura, A., Orsini, S., Milillo, A., et al. 2005, *Icarus*, 175, 305
- Mura, A., Wurz, P., Lichtenegger, H. I. M., et al. 2009, *Icarus*, 200, 1

- Neumann, G. A., Cavanaugh, J. F., Sun, X., et al. 2013, *Science*, 339, 296
- Potter, A., & Morgan, T. 1985, *Science*, 229, 651
- Potter, A. E. 1995, *Geophys. Res. Lett.*, 22, 3289
- Potter, A. E., & Killen, R. M. 2008, *Icarus*, 194, 1
- Potter, A. E., Killen, R. M., & Morgan, T. H. 1999, *Planet. Space Sci.*, 47, 1441
- . 2002, *Meteoritics and Planetary Science*, 37, 1165
- . 2007, *Icarus*, 186, 571
- Potter, A. E., Killen, R. M., & Sarantos, M. 2006, *Icarus*, 181, 1
- Potter, A. E., & Morgan, T. H. 1987, *Icarus*, 71, 472
- . 1990, *Science*, 248, 835
- . 1997, *Advances in Space Research*, 19, 1571
- Press, W. H., Teukolsky, S. A., Vetterling, W. T., & Flannery, B. P. 2007, *Numerical Recipes: The Art of Scientific Computing*. Third Edition
- Russell, C. T., Baker, D. N., & Slavin, J. A. 1988, 514
- Sandin, C., Becker, T., Roth, M. M., et al. 2010, *A&A*, 515, A35
- Sansonetti, J. E. 2008, *J. Phys. Chem. Ref. Data*, 37, 1659
- Sarantos, M., Killen, R. M., & Kim, D. 2007, *Planet. Space Sci.*, 55, 1584
- Sarantos, M., Killen, R. M., Surjalal Sharma, A., & Slavin, J. A. 2010, *Icarus*, 205, 364
- Sarantos, M., Reiff, P. H., Hill, T. W., Killen, R. M., & Urquhart, A. L. 2001, *Planet. Space Sci.*, 49, 1629
- Schleicher, H., Wiedemann, G., Wöhl, H., Berkefeld, T., & Soltau, D. 2004, *Astron. Astrophys.*, 425, 1119
- Schmidt, C. A. 2013, *Journal of Geophysical Research (Space Physics)*
- Schmidt, C. A., Baumgardner, J., Mendillo, M., & Wilson, J. K. 2012, *Journal of Geophysical Research (Space Physics)*, 117, 3301
- Schmidt, C. A., Wilson, J. K., Baumgardner, J., & Mendillo, M. 2010, *Icarus*, 207, 9

- Schroeder, D. J. 1987, *Astronomical optics*
- Self, D. E., & Plane, J. M. C. 2002, *Physical Chemistry Chemical Physics (Incorporating Faraday Transactions)*, 4, 16
- Slavin, J. A., Anderson, B. J., Baker, D. N., et al. 2010a, *Science*, 329, 665
- Slavin, J. A., Lepping, R. P., Wu, C.-C., et al. 2010b, *Geophys. Res. Lett.*, 37, 2105
- Slavin, J. A., Anderson, B. J., Baker, D. N., et al. 2012, *Journal of Geophysical Research (Space Physics)*, 117, 0
- Smith, S. M., Wilson, J. K., Baumgardner, J., & Mendillo, M. 1999, *Geophys. Res. Lett.*, 26, 1649
- Smyth, W. H. 1986, *Nature*, 323, 696
- Smyth, W. H., & Marconi, M. L. 1995, *ApJ*, 441, 839
- Spencer, J. R., Lebofsky, L. A., & Sykes, M. V. 1989, *Icarus*, 78, 337
- Sprague, A. L. 1992, *J. Geophys. Res.*, 97, 18257
- Sprague, A. L., Kozlowski, R. W. H., Hunten, D. M., et al. 1997, *Icarus*, 129, 506
- Sundberg, T., Slavin, J. A., Boardsen, S. A., et al. 2012, *Journal of Geophysical Research (Space Physics)*, 117, 0
- Thompson, M. W. 1968, *Philosophical Magazine*, 18, 377
- Čapek, D., & Borovička, J. 2009, *Icarus*, 202, 361
- van Dokkum, P. G. 2001, *Publications of the Astronomical Society of the Pacific*, 113, 1420
- Vasavada, A. R., Paige, D. A., & Wood, S. E. 1999, *Icarus*, 141, 179
- Vervack, R. J., McClintock, W. E., Bradley, E. T., et al. 2009, 40, 2220
- Vervack, R. J., McClintock, W. E., Killen, R. M., et al. 2010, *Science*, 329, 672
- Wang, Y.-C., & Ip, W.-H. 2008, *Advances in Space Research*, 42, 34
- Wiens, R. C., Burnett, D. S., Calaway, W. F., et al. 1997, *Icarus*, 128, 386
- Wilson, J. K., Baumgardner, J., & Mendillo, M. 1998, *Geophys. Res. Lett.*, 25, 225

- . 2003, *Geophys. Res. Lett.*, 30, 1649
- Wilson, J. K., Mendillo, M., Baumgardner, J., et al. 2002, *Icarus*, 157, 476
- Wilson, J. K., Mendillo, M., & Spence, H. E. 2006, *Journal of Geophysical Research (Space Physics)*, 111, 7207
- Wilson, J. K., & Schneider, N. M. 1994, *Icarus*, 111, 31
- Wilson, J. K., Smith, S. M., Baumgardner, J., & Mendillo, M. 1999, *Geophys. Res. Lett.*, 26, 1645
- Winslow, R. M., Johnson, C. L., Anderson, B. J., et al. 2012, *Geophys. Res. Lett.*, 39, 8112
- Wurz, P., & Lammer, H. 2003, *Icarus*, 164, 1
- Wurz, P., Whitby, J. A., Rohner, U., et al. 2010, *Planet. Space Sci.*, 58, 1599
- Yakshinskiy, B. V., & Madey, T. E. 1999, *Nature*, 400, 642
- . 2000, *Surface Science*, 451, 160
- . 2004, *Icarus*, 168, 53
- . 2005, *Surface Science*, 593, 202
- Yoshioka, K., Hikosaka, K., Kameda, S., et al. 2008, *Advances in Space Research*, 41, 1386
- Young, A. T. 1994, *Appl. Opt.*, 33, 1108
- Zurbuchen, T. H., Raines, J. M., Slavin, J. A., et al. 2011, *Science*, 333, 1862

Curriculum Vitae

Carl A. Schmidt

Boston University - Center for Space Physics
725 Commonwealth Ave
Boston, MA 02215

Tel: (315) 267 6438
Email: schmidtc@bu.edu
Citizenship: US

Education

M.A., Astronomy, Boston University Dissertation defense: 4 June 2013	2008
---	------

B.A., Physics, University of Colorado	2005
---------------------------------------	------

Experience

Graduate Research Assistant, Boston University	2006 - Present
--	----------------

- Observation, data reduction and modeling of Mercury's atmospheric escape.
- Assisted in design and testing of the imaging spectrograph at Poker Flat Observatory, AK, and two standard spectrographs in use at Boston University's calibration facility

Graduate Teaching Assistant, Boston University	2007
--	------

- Lab instructor for AS101 undergraduate introductory astronomy.

Graduate Teaching Assistant, Boston University	2007
--	------

- Assisted in design, construction, and testing of the Near-Infrared Camera and Fabry-Perot Spectrometer at Apache Point Observatory, NM.

Publications

-
- C. Schmidt (2013) Monte-Carlo Modeling of North-South Asymmetries in Mercury's Sodium Exosphere, *Journal of Geophysical Research*, In Press - 15 June 2013, A50396.

- C. Schmidt, J. Baumgardner, M. Mendillo, J. Wilson (2012) Escape rates and variability constraints for high-energy sodium sources at Mercury, *Journal of Geophysical Research*, Vol 117, A03301.
- C. Schmidt, J. Wilson, J. Baumgardner, M. Mendillo (2010) Orbital Effects on Mercury's Escaping Sodium Exosphere, *Icarus*, Vol 207, Issue 1, p. 9-16.
- F. Hearty and 11 co-authors including C. Schmidt (2005) Colorados Near-Infrared Camera (AKA NIC-FPS) Commissioning on the ARC 3.5M Telescope, *Proc. SPIE*, Vol 5904, p. 199-211.

Grants Awarded

NASA Earth and Space Sciences Fellowship (NESSF)	2010 - 2013
--	-------------

Selected Conference and Meeting Presentations

-
- Schmidt, Baumgardner, Mendillo (2012), Hemispheric asymmetries in Mercury's exosphere DPS Meeting, Abstract DPS2012-410.05.
 - Clarke and 9 co-authors including Schmidt (2012), HST observations and modeling of the Martian hydrogen corona, DPS Meeting, DPS2012-214.01.
 - Schmidt, Baumgardner, Mendillo, Wilson (2011), Escape rates and variability constraints for high-energy sodium sources at Mercury, Joint EPSC/DPS Meeting, Abstract EPSC-DPS2011-100.
 - Mangano and 19 co-authors including Schmidt (2010), The sodium emission from Mercury's exosphere as detected by the IMW coordinated campaign in June 2006, COSPAR Meeting, Abstract B07-0022-10.
 - Schmidt, Baumgardner, Mendillo, Davis, Musgrave (2010), Observations of tail structures at Mercury with the STEREO spacecraft, Joint MESSENGER / Bepi-Colombo Workshop, Abstract 2.2.1.

Invited Presentations

Mercury's Sodium Atmosphere, AOSS, Univ. of Michigan, Ann Arbor, MI	2012
Mercury's Tenuous Atmosphere, Heliophysics, NASA GSFC, Greenbelt, MD	2012

Public Outreach

Workshop Coordinator, Sprout, www.thesprouts.org	2010 - present
Lab Instructor, Upward Bound program, Boston University	2010
Science Fair Judge, O'Bryant Middle School for Math and Sci., Boston, MA	2009